COUPLED MAGNETO-ELASTOSTATIC ANALYSIS USING IMPLICIT BOUNDARY FINITE ELEMENT METHOD

By

SUNG-UK ZHANG

A DISSERTATION PRESENTED TO THE GRADUATE SCHOOL
OF THE UNIVERSITY OF FLORIDA IN PARTIAL FULFILLMENT
OF THE REQUIREMENTS FOR THE DEGREE OF
DOCTOR OF PHILOSOPHY

UNIVERSITY OF FLORIDA

2010

To God and my family

ACKNOWLEDGMENTS

I would like to express my sincere gratitude to my advisor, Dr. Ashok V. Kumar for his guidance, enthusiasm, and constant support throughout my doctoral research. His recommendations and suggestions have been invaluable for the research. I would also like to thank the members of my advisory committee, Dr. Bhavani V. Sankar, Dr. John K. Schueller, Dr. Peter G. Ifju, and Dr. Toshi Nishida. I am grateful for their willingness to serve on my committee, for valuable suggestions in my oral qualifying examination and for reviewing this dissertation.

I also wish to thank my colleagues at Design and Rapid Prototyping Laboratory at the University of Florida for their help and their dissertations. The dissertations of Ravi K. Burla and Sanjeev Padmanabhan were valuable. The help of Prem Dheepak and Nitin Chandola improved my research. I would like to thank my family. Without their constant love and support, this would not have been possible.

TABLE OF CONTENTS

CHAPTER

LIST OF TABLES

Table page

LIST OF FIGURES

Abstract of Dissertation Presented to the Graduate School
of the University of Florida in Partial Fulfillment of the
Requirements for the Degree of Doctor of Philosophy

COUPLED MAGNETO-ELESTOSTATIC ANALYSIS USING IMPLICIT BOUNDARY FINITE ELEMENT METHOD

By

SUNG-UK ZHANG

May 2010

Chair: Ashok V. Kumar
Major: Mechanical Engineering

Implicit boundary finite element method (IBFEM) uses solution structures constructed using step functions to enforce boundary and interface conditions so that a structured grid can be used to perform the analysis. A structured grid, which consists of regular shaped elements, is much easier to generate than conforming mesh thus eliminating the difficulties associated with mesh generation for complex assembles.

In this study, IBFEM is extended to solve 2D and 3D magnetostatics, compute magnetic forces and to solve coupled magneto-elastostatic problems that typically involve an assembly of parts made of several different materials. The geometry is accurately modeled using equations from CAD models and a separate structured mesh is used for each part in an assembly. Specially constructed solution structures are used to represent test and trial functions such that boundary and interface conditions are enforced.

Several magnetostatic problems with known solutions are modeled to validate the method. The magnetostatic problems are classified as unbound problems so that sometimes a very large analysis domain should be modeled to get more accurate results. In order to reduce the analysis domain, two open boundary techniques are

developed for IBFEM: asymptotic boundary conditions and decay function infinite element. In addition, a magnetostatic problem with permanent magnets is solved using IBFEM.

CHAPTER 1
INTRODUCTION

Overview

Implicit boundary finite element method (IBFEM) is a modified finite element method that avoids the need for a conforming mesh. IBFEM has been applied to solid mechanics and heat transfer problems in past work [13]-[16], [65]. In this study, IBFEM is extended to perform magnetostatic analysis as well as coupled magneto-elastostatic analysis.

Magnetostatic analysis and force computation for magnetic actuators involves modeling an assembly of components with different material properties. The traditional finite element method has been used for such analysis but it requires a conforming mesh that approximates the geometry of the assembly. The mesh must contain nodes along the external boundaries and the interfaces between parts. The edges / faces of the elements must approximate these interfaces. Figure 1-1 shows a typical mesh where both the boundary and the interfaces between materials are approximated poorly if the mesh is not very dense. Furthermore, the mesh generator has to ensure sufficient node density along the boundary / interface and proper connectivity so that element edges are not connected across the interface.

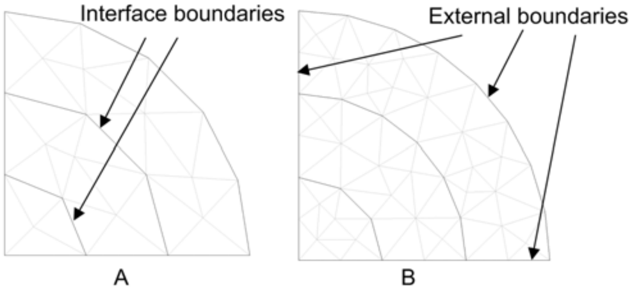

Figure 1-1. Conformal mesh. A) 33 elements, and B) 82 element

Generating such a mesh is difficult and, despite decades of research, 3D mesh generation (especially using hexahedral elements) is still not a fully automated process and in fact requires significant user input. To address mesh generation difficulties, several meshless methods [1] have been proposed that still need a well-placed distribution of nodes but does not requires these nodes to be connected into elements. Some of these methods have been successfully used for magnetostatic analysis [2]-[7]. These methods use interpolation and approximation schemes that do not need connectivity between nodes. However, computationally these methods are more expensive and they still approximate boundaries and interfaces using nodes along them.

An alternate approach to avoid mesh generation difficulties is to use a structured background mesh to represent the solution while using accurate equations of curves and surfaces to present the boundaries. A structured mesh consists of uniform regular shaped elements and is therefore easy to generate. Extended finite element method (X-FEM) [8-10] is one such method which uses a structured mesh and implicit equations for the boundaries and interfaces. In the X-FEM approach, the solution is enriched near singularities and discontinuities such as cracks. An important application of this method has been fracture mechanics, where crack propagation [11]-[12] is simulated by modifying the equations of the crack rather than regenerating the mesh. Boundary and interface conditions have been imposed using Lagrange multiplier and Penalty methods for X-FEM.

The Implicit Boundary FEM (IBFEM), described in this study, uses solution structures constructed utilizing implicit equations of the boundaries to enforce boundary and interface conditions. This method has been applied to 2D and 3D elastostatics and steady state heat transfer problems [13]-[16]. Structured mesh, which has uniform and undistorted elements, can be used for the analysis because the implicit boundary method does not require nodes on the boundary to impose boundary conditions. Compared to the conformal mesh shown in Figure 1-2 B, the structured mesh, such as the examples shown in Figure 1-2 C, is easy to generate since all elements are regular shaped and the grid does not have to conform to the geometry.

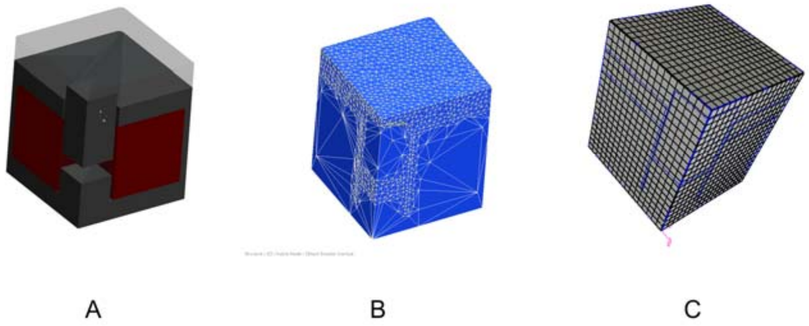

Figure 1-2. Conformal mesh versus Structured mesh. A) Solid model, B) Conformal mesh, and C) Structured mesh

For modeling multiple materials and assemblies, a separate grid is generated for each material or part as shown in Figure 1-3. Within overlapping elements at the interface, the piece-wise interpolation within each grid in combined into a single solution structure as explained in the later chapter.

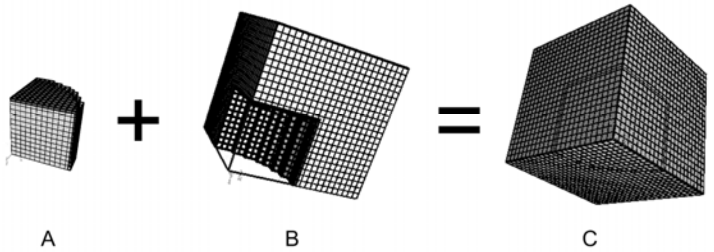

Figure 1-3. 3D structured girds on multi-material. A) Material 1, B) Material 2 and C) Multi-material

IBFEM is extended to solve magneto-static problems. Some magneto-static problems can be characterized as 2D problems the geometry has constant thickness or depth. If the magnetic field can be assumed to be in a plane then the problem can be modeled as 2D planar magneto-static problems. Cylindrical shaped models and models symmetric about an axis are classified as the 2D axisymmetric problem. Such simple structures can be analyzed under the 2D assumption. Magnetic vector potential becomes a scalar in 2D problems whose governing equation is a Poisson's equation. The Poisson's equation is also the governing equation in steady state heat transfer problems [14]. Under the 2D assumption, several applications with multiple components can be analyzed such as magnetic actuators, coaxial cables and switched reluctance motors. Using the IBFEM, it is possible to use B-spline shape functions instead of the traditional finite element shape functions if needed. The advantage of using B-splines is that the computed magnetic flux density and field (or stresses and strains) are continuous between elements.

Under the 2D assumption, magneto-static analysis is computationally inexpensive; however, 3D magneto-static analysis is necessary when the shape of the structures is not simple. In the case of 3D problems, the number of equations drastically increases because the magnetic vector potential is a 3D vector and the number of nodes per element increases due to the usage of 3D elements. Although the current density is a scalar value in 2D magneto-static analysis, in 3D, the current density becomes a vector field. Therefore, the current density distribution must be computed by electrostatic analysis prior to magneto-static analysis. Under the above considerations, several 3D magneto-static problems are solved in this study.

Since magnetostatic problems are often infinite domain problems, an open boundary technique is needed to obtain more accurate results in order to use small finite domain. Among several open boundary techniques, asymptotic boundary condition and infinite element with decay functions are implemented for IBFEM. Several structures including permanent magnet are studied and the results are compared to ones from commercial software or analytical solutions.

After validating IBFEM for magneto-static analysis, the method is extended to solve coupled magneto-elastostatic problems. One of the applications for the coupled analysis is for micro air vehicles. Micro air vehicles (MAV) have recently been developed for military or scientific purposes. MAV are useful for scouting in dangerous or hazardous area where ground vehicles cannot go. Airplane-like fixed wings and helicopter-like rotary wings are widely used because of higher efficiency in the fixed wings and hovering capability in the rotary wings. One way to miniaturize MAVs further is to use flapping wings. In order to design the flapping wings actuated using magnetic forces, a coupled magneto-elastostatic analysis is needed because the magnetic force produced by the actuator deforms the flapping wings. In traditional magnetic actuators, the magnetic force is used to create a rigid body motion of a rotor and any attached mechanism. Coupled magneto-elastic analysis is needed when the magnetic forces produce structural deformation.

In this research, using coupled analysis, magnetic actuators for flapping wings are designed as shown in Figure 1-4. Figure 1-4 A shows the downward wing stroke when the magnetic actuator turns off. Figure 1-4 B shows the upward wing stroke when it turns on. Several magnetic actuators are characterized in terms of magnetic force and iron weight to design a proper actuator for flapping wings.

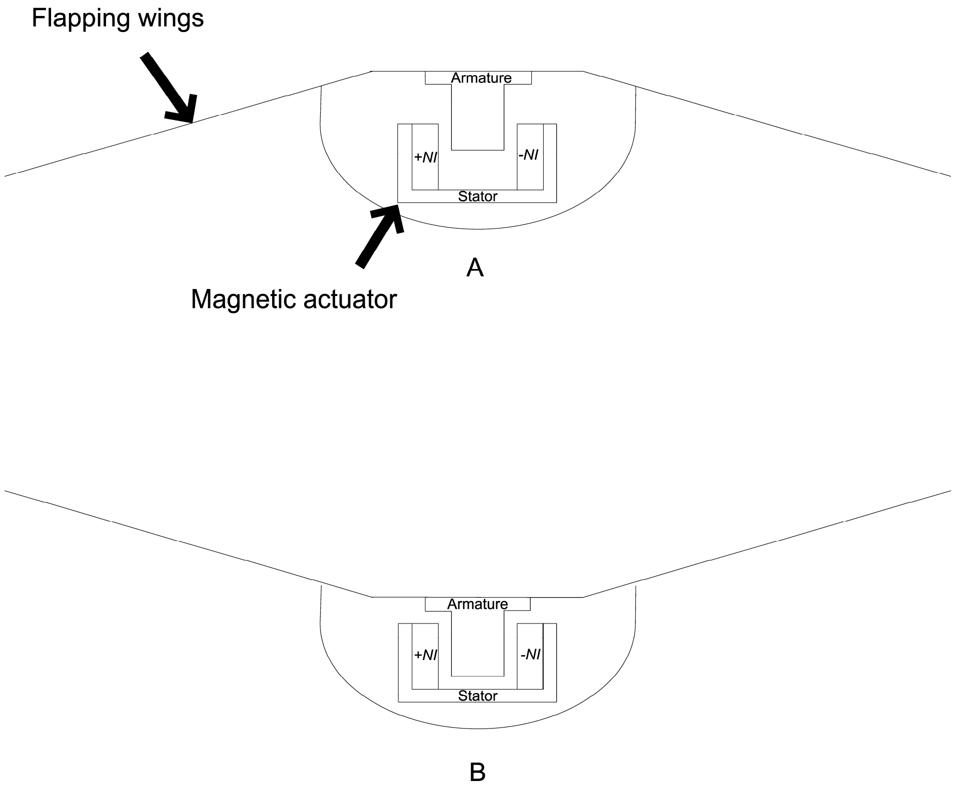

Figure 1-4. Flapping wings operated by magnetic actuator. A) Downward wing stroke, and B) Upward wing stroke

Goals and Objectives

The goal of this research is to extend the Implicit Boundary Finite Element Method (IBFEM) to develop capability for multi-material system analysis and to perform magnetostatic analysis as well as coupled magneto-elastostatic analysis.

The main objectives of this dissertation are to extend IBFEM to

- Perform 2D magneto-static analysis
- Perform 3D magneto-static analysis
- Model permanent magnets

- Perform multi-material analysis
- Compute magnetic forces, and
- Solve coupled magneto-elastostatic analysis

In addition, IBFEM are tested and validated using several examples: coaxial cable, solenoid actuator, U-shaped permanent magnet and so on. Based on the analysis capability of IBFEM, it is used as magnetic actuator design tool in order to design magnetically actuated structures.

Outline

The rest of the dissertation is organized as follows:

Chapter 2 briefly discusses computational electromagnetics, Maxwell’s equations, overview of magnetic actuators and overview of reluctance method. Among the Maxwell’s equations, Gauss’s law and Ampere’s law are used as the governing equations for elastostatics and magnetostatics. In addition, the chapter describes how to analyze magnetic actuators using the reluctance method.

Chapter 3 discusses previous works for Implicit Boundary Finite Element Method. The chapter briefly describes the motivation for IBFEM, applications for solid mechanics, and B-spline element.

Chapter 4 discusses 2D magneto-static analysis with IBFEM. A modified solution structure is introduced for the multi-material analysis. Application of permanent magnet is described.

In Chapter 5, 3D magneto-static analysis with IBFEM is described. The chapter introduces the difficulties for 3D magneto-static analysis, and 3D coupled magneto-elastostatic analysis is introduced.

Chapter 6 discusses open boundary techniques. Infinite element with decay function and asymptotic boundary condition are introduced for IBFEM.

Chapter 7 provides several results and discussions for 2D and 3D magnetostatics, coupled analysis and permanent magnet problems.

Chapter 8 explains several small actuators for flapping wings under the specific specifications. IBFEM is introduced as a design tool.

Finally, chapter 9 provides the summary of the results and conclusions. The further work is suggested in the end of the dissertation.

CHAPTER 2
MAGNETOSTATIC ANALSIS

Computational Electromagnetics

Researchers have studied electromagnetic devices using Maxwell's equations. By the Maxwell's equations, electromagnetic fields are computed to characterize the behaviors of electromagnetic devices such as transistors, electrical machines, waveguides, and so on. Before the advent of computers, the only way to solve the Maxwell's equations was using elaborate mathematics such as series expansions, Legendre polynomials, Bessel's functions, and so on. Using these methods, the solving process took days or they needed to make drastic simplifying assumption on device geometry, current and charge distribution. For example, the geometry is assumed to be circular or rectangular and the current distribution is suggested to be uniform in the analysis domain. Under those assumptions, they can obtain a closed form solution.

After the advent of the computer, several numerical schemes could make solutions without the severe assumptions. With a realistic design, researchers can solve Maxwell's equations so that they can predict the behavior of the electromagnetic devices. Although those schemes are approximation methods, solutions by those schemes are accurate enough. Sometimes using the simple geometry such as circular or rectangular, the analytic solution by classical methods is more accurate than the numerical solution. However, the numerical schemes are not comparable to the classical methods in term of area of applications. For computational electromagnetics, several numerical schemes have been introduced such as finite difference method, variational methods, differential variational schemes, finite element method and so on

[17]. Among those numerical schemes, the finite element method is known as a general method to solve differential equations.

Maxwell's Equations

Maxwell's equations are a set of four partial differential equations that relate the electric and magnetic fields to their sources, charge density and current density. The individual equations are known as Gauss's law, Gauss's law for magnetism, Faraday's law of induction and Ampere's law. Figure 2-1 shows conceptual drawings for Maxwell's equations

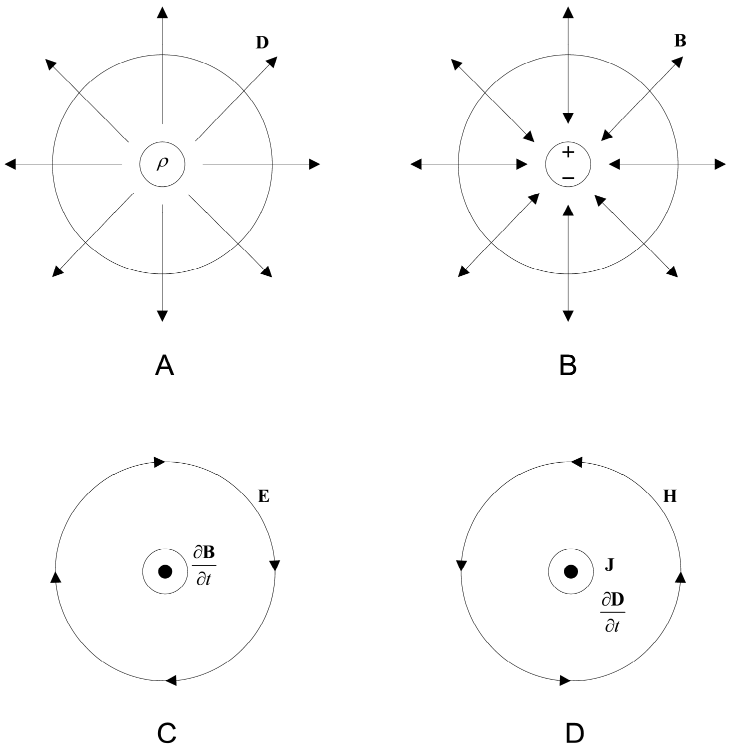

Figure 2-1. Maxwell's equations. A) Gauss's law, B) Gauss's law for magnetism, C) Faraday's law of induction, and D) Ampere's circuital law.

Figure 2-1 A shows Gauss's law that relates electrical charge within a close surface to the surrounding electric field. The differential form of the Gauss's law is expressed as

$$\nabla \cdot \mathbf{D} = \rho \tag{2-1}$$

where, $\mathbf{D}$ is the electric flux density and ρ is the electrical charge density. The constitutive equation is written as

$$\mathbf{D} = \varepsilon \mathbf{E} \tag{2-2}$$

where, $\mathbf{E}$ is the electric field, and ε is the permittivity for dielectric material. Figure 2-1 B shows Gauss's law for magnetism which means the total magnetic flux through a closed surface is zero. As the dipole magnetic change only exists in real world, the divergence of magnetic fields cancels each other out. The differential form for Gauss's law for magnetism is stated as

$$\nabla \cdot \mathbf{B} = 0 \tag{2-3}$$

where, $\mathbf{B}$ is the magnetic flux density. Figure 2-1 C shows Faraday's law of induction. The law states that a changing magnetic field produces an induced electric field, which is the operating principle for many electric generators. The differential form for Faraday's law of induction is stated as

$$\nabla \times \mathbf{E} = -\frac{\partial \mathbf{B}}{\partial t} \tag{2-4}$$

Ampere's law with Maxwell's correction is shown in Figure 2-1 D. The law indicates that two factors can generate magnetic field; electrical current and changing electric flux density. The differential form for Ampere's law with Maxwell's correction is written as

$$\nabla \times \mathbf{H} = \mathbf{J} + \frac{\partial \mathbf{D}}{\partial t} \tag{2-5}$$

where, $\mathbf{H}$ is the magnetic field. The constitutive equation between $\mathbf{H}$ and $\mathbf{B}$ can be stated as

$$\mathbf{B} = \mu \mathbf{H} \tag{2-6}$$

where, μ is the permeability.

For electric field problems, dielectric materials are characterized by the permittivity ε. However, conductive materials are characterized by the conductivity σ so that a different constitutive equation is used which is stated as

$$\mathbf{J} = \sigma \mathbf{E} \tag{2-7}$$

After taking the divergence of Ampere's law, the equation can be written as

$$\nabla \cdot \left(\nabla \times \mathbf{H} \right) = \nabla \cdot \mathbf{J} + \nabla \cdot \frac{\partial \mathbf{D}}{\partial t} = \nabla \cdot \mathbf{J} + \frac{\partial \left(\nabla \cdot \mathbf{D} \right)}{\partial t} = 0 \tag{2-8}$$

Equation 2-8 can be restated as

$$\nabla \cdot \mathbf{J} = -\frac{\partial \rho}{\partial t} \tag{2-9}$$

The equation is called the electrical continuity equation. Practically all electromagnetic devices guarantee that the input current is equal to the output current for the devices. Otherwise, electrical charge accumulates in the device or is produced by the device. Therefore, the electrical continuity equation is normally written as

$$\nabla \cdot \mathbf{J} = 0 \tag{2-10}$$

Overview of Magnetic Actuator

Among many electromagnetic devices, magnetic actuators are the focus of this study. Magnetic actuators have widely been used as components of electro-hydraulic valves, fuel injectors in engines of automobiles, biomedical prosthesis devices for artificial organs, head positioners for computer disk drives, loudspeakers and relays [18]. The magnetic actuator is an energy conversion device or a transducer. This transducer transforms magnetic energy to mechanical energy. In order to use these actuators as precise components, inputs and outputs need to be controllable. For the input, magnetic circuit is used for electrical signal to be able to control the intensity or direction of the magnetic field. The electrical signal is characterized as directed current (DC) and alternating current (AC). For the output, mechanical system is used to render magnetic force to be used as controlled mechanical output. Figure 2-2 shows the block diagram of a magnetic actuator. The electrical input can be direct current or alternating current. The mechanical output can be rotary motion or linear motion. The flexibility of the input and the output enables broad application of magnetic actuators. In order to design a proper magnetic actuator for a specific application, sometimes the analysis of the magnetic actuator is difficult because of complexities within three blocks: magnetic circuit, force factor, and mechanical system shown in Figure 2-2. As these blocks often involve the complex geometry, the analysis of magnetic actuator becomes complicated so that numerical schemes such as finite element method are required.

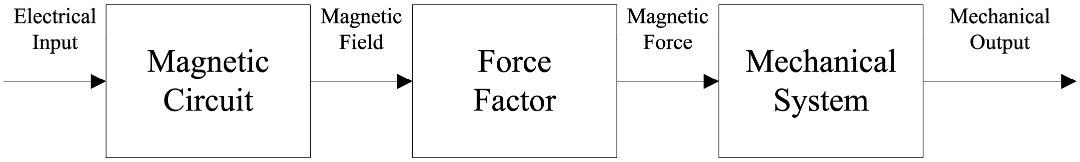

Figure 2-2. Block diagram of a magnetic actuator

In this study, only direct current (DC) is used as the input. The common types of magnetic actuators using DC are solenoid actuators, coil actuators, proportional actuators and rotary actuators.

Solenoid actuators have an armature (moving part) and a stator (stationary part). The armature is made of steel laminates so that eddy current effect is reduced. Eddy currents create heat in a device that leads to energy loss. The stator has a solenoid coil which is wound into shapes like cylinder, cubic, or parallelepiped. Solenoid actuators can produce linear motion of the armature which can be designed in a variety of shapes.

Rotary actuators generate rotary motion as the mechanical output instead of the linear motion of solenoid actuators. Rotary actuators have a rotor (moving part) and a stator (stationary part). The most common rotary magnetic actuator is a step motor. The step motor is used to work with a microprocessor or a digital signal processor which produces digital pulses for controlling the motion. The processors send digital signals to the step motor in order to generate incremental step motion. One example of the step motors is a switched reluctance motor with the rotor composed of only steel laminations. The advantages of the switched reluctance motor are high speed operation and the lowest construction cost because of the simple structure and the absence of permanent magnets [19]. In addition, minimum switching devices are required because only unidirectional current is needed. Because of above merits, the switched reluctance motor has several applications including electric propulsion, fan and pump.

Coil actuators are linear motion actuators that can produce reversible force. Although forces on ferromagnetic material are used for the solenoid actuators, Lorentz force on current-carrying coil is used for coil actuators. The Lorentz force is expressed as

$$F = NIBl \tag{2-11}$$

where, N is the number of turns for the coil, I is the amount of current per one turn coil, l is the average turn length and B is the magnetic flux density which is perpendicular to the coil direction. As the force is proportional to the current, the direction of the force can be controlled by the direction of the current. Usually, the magnetic field is provided by permanent magnets so that high flux density can be obtained without any power loss and temperature increments on the device. Coil actuators are widely used in loudspeakers, where they are called voice coil actuators. Another popular application is a computer disk drive head actuation.

Reluctance Method

In order to analyze a magnetic actuator, reluctance method can be used. The reluctance method is also called magnetic circuit method, which is a simplified method to solve for magnetic fluxes and magnetic fields. For a magnetic actuator model with simple geometry, the reluctance method is an analytical method to estimate actuator's characteristics such as approximate magnetic fluxes, magnetic fields and magnetic force. In this study, magnetic fluxes and magnetic force by the reluctance method is used to compare with IBFEM's results.

The reluctance method is based on the Ampere's law. Ampere's law in integral form can be expressed as a summation form as follows

$$\oint \mathbf{H} \cdot \mathbf{dl} = NI \quad \rightarrow \quad \sum_k H_k l_k = \sum_k \left(\frac{B_k}{\mu_k} \right) l_k = NI \tag{2-12}$$

where, NI is the ampere-turns, l_k is the line segment along the field intensity H_k and μ_k is the permeability of path segment k. The magnetic flux in the surface integral form can be redefined in discrete form as follows

$$\phi = \int \mathbf{B} \cdot \mathbf{dS} \quad \rightarrow \quad \phi_k = B_k S_k \tag{2-13}$$

where, ϕ and ϕ_k is the magnetic flux and the magnetic flux on the *k*th path and B_k is the magnetic flux density normal to the cross-section surface area S_k. Substituting into the Ampere's law in the summation form, Equation 2-12 is stated as

$$\sum_k \left(\frac{\phi_k l_k}{S_k \mu_k} \right) = NI \tag{2-14}$$

As the divergence of flux density is zero, the fluxes through all segments have a same quantity ϕ. So Equation 2-14 is rewritten as

$$\phi\sum_k\left(\overline{R}_k\right)=NI \tag{2-15}$$

where, $\overline{R}_k=\dfrac{l_k}{\mu_k S_k}$ called the reluctance. When the total reluctance $\overline{R}$ and the ampere-turns, which is called magnetomotive force (MMF), are known, the flux can be expressed as

$$\phi=\frac{NI}{\overline{R}} \tag{2-16}$$

The equation is similar to the familiar Ohm's law of electric circuits: $I=\dfrac{V}{R}$ where I is the electric current, V is the voltage potential, and R is the resistance. The reluctance method, which is also known as the magnetic circuit method, is graphically shown in Figure 2-3.

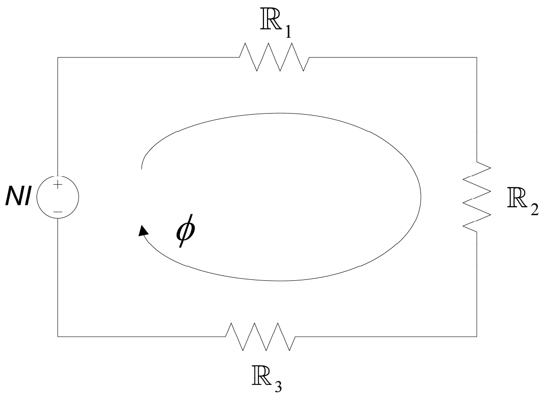

Figure 2-3. Reluctance method (Magnetic circuit method)

Even though the reluctance method is an easy way to estimate magnetic fluxes, the method has a limitation. The reluctance method ignores the fringing flux which means the expansion of flux in air as shown in Figure 2-4.

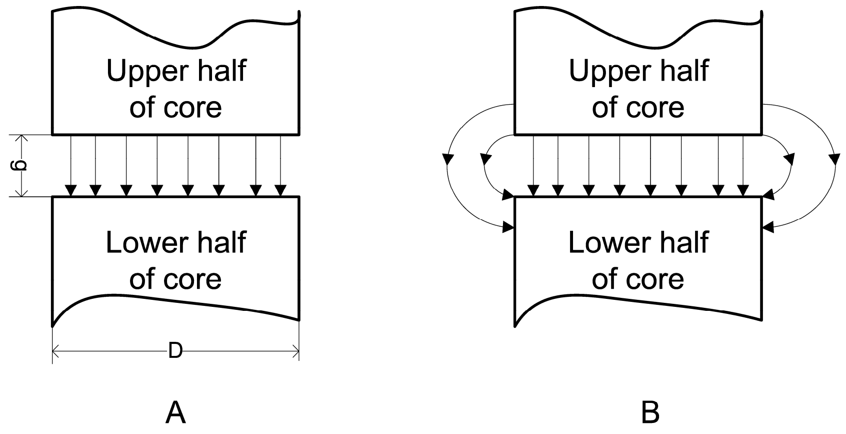

Figure 2-4. Fringing flux. A) Fluxes without fringing flux, and B) Fluxes with fringing flux

When magnetic fluxes flow from the steel to air, the magnetic flux tends to increase because of a large difference in permeability. The fringing flux makes air-gap reluctance decrease so that the total flux increases. The upper and the lower steel cores are cylindrical with the diameter *D* and the air gap length is *g* as shown in Figure 2-4. The fringing flux can be ignored when the ratio g/D is less than about 0.04, which means the reluctance method can be accurate. However, the fringing flux should be considered for larger g/D ratios [18]. Moreover, most devices including complicated geometries or non-linear materials such as permanent magnet are difficult to be analyzed using this method.

CHAPTER 3
IMPLICIT BOUNDARY FINITE ELEMENT METHOD

Overview of Finite Element Method

Partial differential equations are used to express physical phenomenon such as heat transfer, electrostatics, magnetostatics, solid mechanics, and so on. Exact or analytical solutions of those equations can be obtained under restricted conditions of simple geometry and loading conditions. Otherwise it is difficult to obtain analytical solutions. Since complex geometry and loading conditions are common for real physical or engineering situations, alternative methods are necessary to solve those problems. A popular method is the finite element method (FEM), which is a numerical method for solving partial differential equations. FEM has been widely used for solving engineering and mathematical problems both in academia and industry. FEM is a well established numerical method, but it is highly depended on the quality of the domain discretization using a conforming mesh. Often mesh generators are not reliable for 3D domain and if the mesh contains a few highly distorted elements it can lead to inaccurate results.

In order to avoid the need for generating conforming mesh, several meshless techniques has been developed [1], where nodes scattered within the domain are used without connecting them to form elements. Several approximation schemes have been developed that do not need elements or connection between nodes. Researchers have developed different types of meshless techniques such as moving least square approximation method by Nayroles et al. and Belytschko et al., reproducing kernel particle method (RKPM) by Liu et al., Hp clouds method by Duarte et al. and so on. The meshless approximation schemes do not have Kronecker’s delta property that is the value of the approximation at a node is not equal to the nodal value. Therefore, it is difficult to impose essential boundary conditions. Lagrange multiplier approaches, modified variational principles, penalty methods and so on are used as remedies. The Lagrange multiplier method is the more accurate method; however, this method increases the number of variables, causes the element matrix to be non positive definite and non-banded which increases the computational time for solving the equations.

Another approach to avoid traditional mesh generation is to use structured grid methods. Structured grids have regular, undistorted elements and are therefore easy to generate automatically. A structured grid does not approximate the geometry of the analysis domain adequately therefore the geometry has to be independently represented using equations. It is possible to use a variety of interpolation or approximation methods with structured grid methods. Belytschko et al. developed extended finite element method (X-FEM) [8], which uses implicit equations to define the geometry of the domain. And they used Lagrange multipliers to apply essential boundary conditions. Kantorovich and Krylov proposed a solution structure constructed using implicit equations of the boundaries, a solution structure that ensures that essential boundary conditions are satisfied at these boundaries. Rvachev et al used R-functions to construct implicit equations for the solution structure, and analyzed numerous partial differential equations [20]. The R-function method is a way to define implicit equations for domains using Boolean operations between simple primitives. Shapiro and Tsukanov extended the R-function method to solve non-stationary physical problems with time-varying geometries, and used transfinite Lagrangian interpolation to apply essential boundary conditions [21]. Hollig et al. proposed the Web-method which uses weighted extended B-spline basis to guarantee higher order continuous solutions

[22]. Their method has been used with R-functions or distance functions as implicit equations in order to construct the solution structures. In addition, Apaydin et al have extended the Web-method to solve one-dimensional electromagnetic problems and two-dimensional electromagnetic wave equations [23]-[24].

In this study, the implicit boundary finite element method (IBFEM) is used, which has been developed by Kumar et.al [13]-[16], [65]. It has been used in the past to analyze 2D and 3D elastostatics and steady state heat transfer. IBFEM uses solution structures constructed using approximate step functions of the boundaries. Approximate step functions have a unit value inside the domain of analysis and transition sharply to zero at the boundary. An advantage of using step functions to construct the solution structure is that all the internal elements have identical element matrix. IBFEM has been used with traditional FEM interpolations also known as Lagrange interpolation as well as with uniform B-spline approximations [15].

IBFEM for Elastostatics

Kantorovich and Krylov first proposed using solution structures constructed using implicit equations of boundaries to impose essential boundary conditions when using nonconforming mesh / structured grids. Since the nodes of the structured grid may not lie on boundary, traditional methods for applying boundary conditions cannot be used. For elastostatics, a solution structure is expressed as

$$\mathbf{u} = \mathbf{D} \cdot \mathbf{u}^g + \mathbf{u}^a = \mathbf{u}^s + \mathbf{u}^a \tag{3-1}$$

where $\mathbf{u}$ is the displacement vector , $\mathbf{u}^g$ is the *grid variable* represented by a piece-wise interpolation, $\mathbf{u}^a$ is the boundary value function with prescribed values, $\mathbf{u}^s$ is defined as the homogenous part of the solution, and $\mathbf{D} = diag(D_i, .., D_{n_d})$ is the diagonal matrix where

D_i is an approximate step function that has been referred to as Dirichlet function [13] . At any given point $\mathbf{x} \in R^3$, a Dirichlet function (or D-function) is defined as

$$D(\mathbf{x}) = \begin{cases} 0 & \phi(\mathbf{x}) \le 0 \\ 1 - \left(1 - \dfrac{\phi(\mathbf{x})}{\delta}\right)^k & 0 \le \phi(\mathbf{x}) \le \delta \\ 1 & \phi(\mathbf{x}) \ge \delta \end{cases} \tag{3-2}$$

where, k is an integer. The D-function has C^{k-1} continuity at $\phi(\mathbf{x}) = \delta$ where $\phi(\mathbf{x}) = 0$ is the implicit equation of the boundary at which the essential boundary conditions are applied. The D-function transitions between 0 and 1 in a narrow band $0 \le \phi(\mathbf{x}) \le \delta$. For IBFEM, very small values of δ is used (10^{-5} or smaller value) so that this band is very narrow and the D-function is a good approximation of a step function. Hollig et al. have used a weighting function that is similar to the D-function. However, they use relatively larger value of δ so that the weighting function is not a step function. The advantage of using an approximate step function for constructing solution structure is that all internal elements have identical element matrix. However, special techniques are needed to handle the large gradient of the step function within the band.

There are several ways to construct the boundary value function. In this study, the boundary value function is defined as

$$\mathbf{u}^a = \sum_i N_i u_i^a \tag{3-3}$$

where, N_i is the shape functions which are identical to the basis functions used for the grid variable and u_i^a is the nodal values of the boundary elements in which the essential boundary conditions are applied. For example, if the prescribed value at a boundary is constant equal to 3, then the value, of all the support nodes of the boundary element, is set equal to 3. The other nodes are set to zero. Figure 3-1 graphically depicts the solution structure. The element e1 is a boundary element and the others are internal elements.

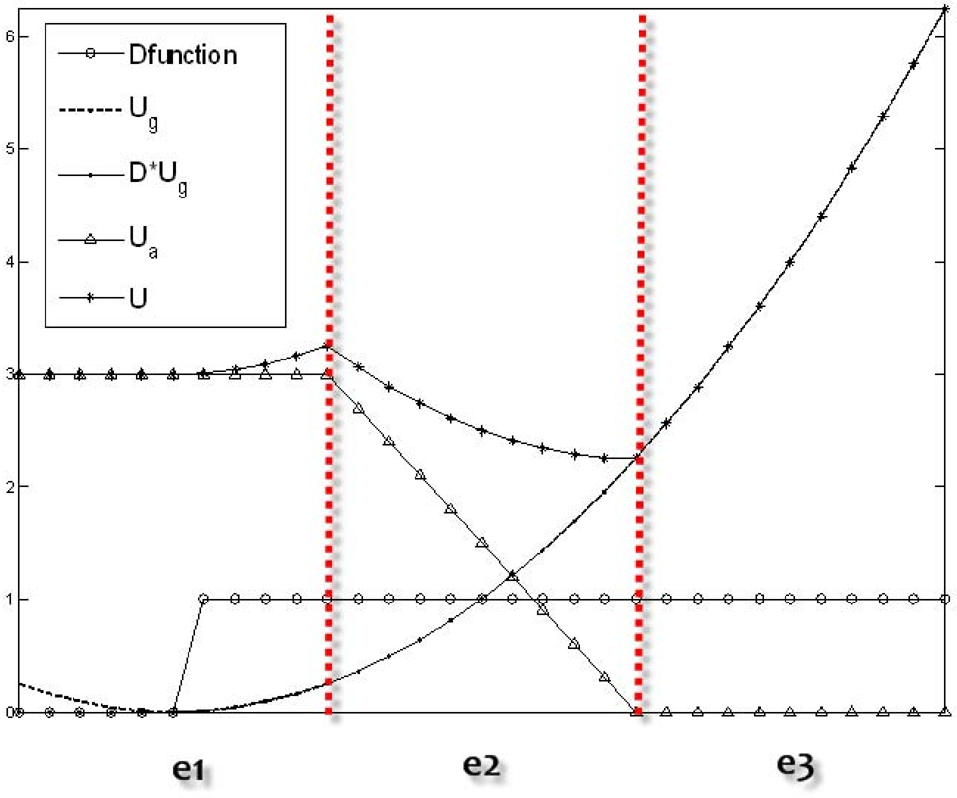

Figure 3-1. The solution structure with the essential boundary condition

If the homogenous part of the solution and the boundary value function for the displacement vector are defined as $\mathbf{u}^s = \{u^s, v^s\}$ and $\mathbf{u}^a = \{u^a, v^a\}$. The strain can be stated as

$$\boldsymbol{\varepsilon} = \boldsymbol{\varepsilon}^s + \boldsymbol{\varepsilon}^a \tag{3-4}$$

For 2D problems in Voigt notation these strains can be defined as

$$\boldsymbol{\varepsilon}^s = \left\{ \frac{\partial u^s}{\partial x} \quad \frac{\partial v^s}{\partial y} \quad \frac{\partial u^s}{\partial y} + \frac{\partial v^s}{\partial x} \right\}^T, \quad \boldsymbol{\varepsilon}^a = \left\{ \frac{\partial u^a}{\partial x} \quad \frac{\partial v^a}{\partial y} \quad \frac{\partial u^a}{\partial y} + \frac{\partial v^a}{\partial x} \right\}^T \tag{3-5}$$

Using the constitutive equation, the stress is

$$\boldsymbol{\sigma} = \boldsymbol{\sigma}^{\mathbf{s}} + \boldsymbol{\sigma}^{\mathbf{a}} = \mathbf{C} \cdot \boldsymbol{\varepsilon}^s + \mathbf{C} \cdot \boldsymbol{\varepsilon}^a \tag{3-6}$$

where, $\mathbf{C}$ is the elasticity matrix. The governing equation for linear elasticity is stated as

$$\nabla \cdot \boldsymbol{\sigma} + \mathbf{b} = 0 \quad \text{in} \quad \Omega \tag{3-7}$$

where, $\mathbf{b}$ is the boundary force, Ω is the analysis domain. The essential boundary and natural boundary conditions are defined as

$$\mathbf{u} = \mathbf{u_0} \quad \text{on} \quad \Gamma_u, \quad \boldsymbol{\sigma} \cdot \mathbf{n} = \mathbf{T_0} \quad \text{on} \quad \Gamma_t \tag{3-8}$$

where, $\mathbf{T_0}$ is the traction vector, and Γ_u and Γ_t are the prescribed boundaries for the essential boundary and the natural boundary conditions. Using the solution structure in the principle of virtual work for elastostatics we obtain

$$\int_{\Omega} \boldsymbol{\delta\varepsilon}^{\mathbf{T}} \cdot \boldsymbol{\sigma}^{\mathbf{s}} d\Omega = \int_{\Gamma_t} \boldsymbol{\delta}\mathbf{u}^{\mathbf{T}} \cdot \mathbf{T_0} d\Gamma + \int_{\Omega} \boldsymbol{\delta}\mathbf{u}^{\mathbf{T}} \cdot \mathbf{b} d\Omega - \int_{\Omega} \boldsymbol{\delta\varepsilon}^{\mathbf{T}} \cdot \boldsymbol{\sigma}^{\mathbf{a}} d\Omega \tag{3-9}$$

where, $\boldsymbol{\delta\varepsilon}$ and $\boldsymbol{\delta}\mathbf{u}$ are small perturbation of the strain and the displacement.

Finite Element Formulation for Elastostatics

Considering 2D elastostatic problems, the boundary value function and the homogeneous part of the solution for the displacement field is stated as

$$\begin{aligned} \mathbf{u}^a &= \begin{Bmatrix} u^a \\ v^a \end{Bmatrix} = \begin{bmatrix} N_1 & 0 & \cdots & N_N & 0 \\ 0 & N_1 & \cdots & 0 & N_N \end{bmatrix} \left\{ \mathbf{X}^a \right\} = [\mathbf{N}] \left\{ \mathbf{X}^a \right\}, \\ \mathbf{u}^s &= \begin{Bmatrix} u^s \\ v^s \end{Bmatrix} = D \cdot \begin{bmatrix} N_1 & 0 & \cdots & N_N & 0 \\ 0 & N_1 & \cdots & 0 & N_N \end{bmatrix} \left\{ \mathbf{X}^s \right\} = D \cdot [\mathbf{N}] \left\{ \mathbf{X}^g \right\} \end{aligned} \tag{3-10}$$

where, N_i is the shape function, and $\{\mathbf{X}^a\}$ and $\{\mathbf{X}^g\}$ are the predefined boundary value vector and the unknown nodal grid value vector respectively. Using these definitions, the strain can be expressed as

$$\boldsymbol{\varepsilon}^{a} = \begin{Bmatrix} \dfrac{\partial u^{a}}{\partial x} \\ \dfrac{\partial v^{a}}{\partial y} \\ \dfrac{\partial u^{a}}{\partial y} + \dfrac{\partial v^{a}}{\partial x} \end{Bmatrix} = \begin{bmatrix} \dfrac{\partial N_1}{\partial x} & 0 & \cdots & \dfrac{\partial N_N}{\partial x} & 0 \\ 0 & \dfrac{\partial N_1}{\partial y} & \cdots & 0 & \dfrac{\partial N_N}{\partial y} \\ \dfrac{\partial N_1}{\partial y} & \dfrac{\partial N_1}{\partial x} & \cdots & \dfrac{\partial N_N}{\partial y} & \dfrac{\partial N_N}{\partial x} \end{bmatrix} \left\{ \mathbf{X}^{a} \right\} = \left[\mathbf{B} \right] \left\{ \mathbf{X}^{a} \right\},$$

$$\boldsymbol{\varepsilon}^{s} = \begin{bmatrix} D\dfrac{\partial N_1}{\partial x} & 0 & \cdots & D\dfrac{\partial N_N}{\partial x} & 0 \\ 0 & D\dfrac{\partial N_1}{\partial y} & \cdots & 0 & D\dfrac{\partial N_N}{\partial y} \\ D\dfrac{\partial N_1}{\partial y} & D\dfrac{\partial N_1}{\partial x} & \cdots & D\dfrac{\partial N_N}{\partial y} & D\dfrac{\partial N_N}{\partial x} \end{bmatrix} \left\{ \mathbf{X}^{g} \right\} + \begin{bmatrix} N_1\dfrac{\partial D}{\partial x} & 0 & \cdots & N_N\dfrac{\partial D}{\partial x} & 0 \\ 0 & N_1\dfrac{\partial D}{\partial y} & \cdots & 0 & N_N\dfrac{\partial D}{\partial y} \\ N_1\dfrac{\partial D}{\partial y} & N_1\dfrac{\partial D}{\partial x} & \cdots & N_N\dfrac{\partial D}{\partial y} & N_N\dfrac{\partial D}{\partial x} \end{bmatrix} \left\{ \mathbf{X}^{g} \right\}$$

$$= \left[\overline{\mathbf{B}}_1 \right] \left\{ \mathbf{X}^{g} \right\} + \left[\overline{\mathbf{B}}_2 \right] \left\{ \mathbf{X}^{g} \right\} = \left[\overline{\mathbf{B}} \right] \left\{ \mathbf{X}^{g} \right\} \tag{3-11}$$

The virtual strain and stress are stated as

$$\left\{ \delta\boldsymbol{\varepsilon} \right\} = \left[\mathbf{B} \right] \left\{ \delta\mathbf{X}^{e} \right\}, \quad \left\{ \boldsymbol{\sigma}^{\mathbf{s}} \right\} = \left[\mathbf{C} \right] \left[\mathbf{B} \right] \left\{ \mathbf{X}^{e} \right\} \tag{3-12}$$

where, $\left\{ \delta\mathbf{X}^{e} \right\}$ and $\left\{ \mathbf{X}^{e} \right\}$ are the nodal grid values for the element e. Then, the weak form can be expressed in the following discrete form:

$$\begin{aligned} &\sum_{i=1}^{NE} \left\{ \delta\mathbf{X}^{e} \right\}^{T} \int_{\Omega_e} \left[\mathbf{B} \right] \left[\mathbf{C} \right] \left[\mathbf{B} \right] \left\{ \mathbf{X}^{e} \right\} d\Omega_e \\ &= \sum_{i=1}^{NE} \left\{ \delta\mathbf{X}^{e} \right\}^{T} \int_{\Omega_e} \left\{ \mathbf{N} \right\}^{T} \left\{ \mathbf{b} \right\} d\Omega_e - \sum_{i=1}^{NE} \left\{ \delta\mathbf{X}^{e} \right\}^{T} \int_{\Omega_e} \left[\mathbf{B} \right] \left\{ \boldsymbol{\sigma}^{\mathbf{a}} \right\} d\Omega_e + \sum_{i=1}^{NBE} \left\{ \delta\mathbf{X}^{e} \right\}^{T} \int_{\Gamma_t} \left[\mathbf{N} \right]^{T} \left\{ \mathbf{T_0} \right\} d\Gamma_e \end{aligned} \tag{3-13}$$

where, NE is the total number of elements in the domain, NBE is the number of elements on the boundaries that have natural boundary conditions specified. $\left[\mathbf{N} \right]$ contains the shape functions.

B-spline element

Using Lagrange elements, the traditional FEM only warrants C^0 continuity of a solution between elements. When B-spline approximation is used, higher order continuity of the solution can be guaranteed. Figure 3-2 shows one dimensional solution using Lagrange interpolation and one using B-spline approximation scheme. Both solutions can provide higher order continuity of the solution within elements. However, only C^0 continuity of a solution between the element e1 and the element e2 can be guaranteed using Lagrange interpolation as graphically shown in Figure 3-2 A.

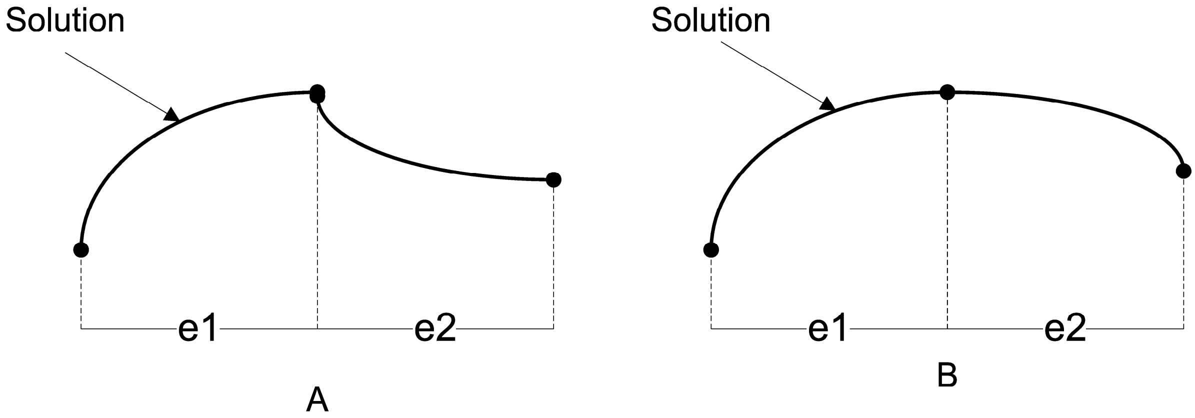

Figure 3-2. One dimensional field solution using two elements. A) Lagrange interpolation, and B) B-spline approximation scheme.

B-spline presentation has been used in computer aided geometric design in order to represent curves and surfaces with higher order of continuity. As it is a parametric representation, the basis functions of B-spline could be adapted to finite elements. Burla and Kumar [15] have solved elastostatic problems using B-spline element with IBFEM. They reported that solutions of IBFEM have faster convergence rate using B-spline element.

In IBFEM, uniform B-splines can be used, which means nodes have been equally spaced in the parametric space. The B-spline shape functions for each element are constructed to have independent parameter space such that the parametric range is from -1 to 1. Namely, one dimensional B-spline element with C^1 continuity has three support nodes and three basis functions. The basis functions are quadratic functions expressed as follows

$$\begin{Bmatrix} N_0 \\ N_1 \\ N_2 \end{Bmatrix} = \begin{bmatrix} a_{00} & a_{01} & a_{02} \\ a_{10} & a_{11} & a_{12} \\ a_{20} & a_{21} & a_{22} \end{bmatrix} \begin{Bmatrix} 1 \\ r \\ r^2 \end{Bmatrix} \tag{3-14}$$

where, N_i are the basis functions, r is the parametric value varying within $[-1,1]$, and a_{ij} are coefficients to be solved. Using these basis functions, the approximated functions of two adjacent elements can be stated as follows

$$f^i(r) = \{N_0 \quad N_1 \quad N_2\}^T \begin{Bmatrix} u_i \\ u_{i+1} \\ u_{i+2} \end{Bmatrix}, \; f^{i+1}(r) = \{N_0 \quad N_1 \quad N_2\}^T \begin{Bmatrix} u_{i+1} \\ u_{i+2} \\ u_{i+3} \end{Bmatrix} \tag{3-15}$$

where, f^i and f^{i+1} are the approximated functions and u_i are the support nodal values. As given B-spline elements warrants C^0 and C^1 continuity, two continuity requirements provides the following restricted conditions :

$$f^i(1) = f^{i+1}(-1) \text{, and } \frac{\partial f^i(1)}{\partial r} = \frac{\partial f^{i+1}(-1)}{\partial r} \tag{3-16}$$

where, $f^i(1)$ is the approximated value at the end point in the *i* th element , $f^{i+1}(-1)$ is the approximated value at the start point in the *i+1* th element, $\frac{\partial f^i(1)}{\partial r}$ is the tangential value at the end point the *i* th element, and $\frac{\partial f^{i+1}(-1)}{\partial r}$ is the tangential value at the start point in the *i*+1 th element. The two conditions lead to following eight independent equations.

$$\begin{Bmatrix} N_0(1) \\ N_1(1) - N_0(-1) \\ N_2(1) - N_1(-1) \\ N_2(-1) \end{Bmatrix} = 0 \text{ and } \begin{Bmatrix} \dfrac{\partial N_0(1)}{\partial r} \\ \dfrac{\partial N_1(1)}{\partial r} - \dfrac{\partial N_0(-1)}{\partial r} \\ \dfrac{\partial N_2(1)}{\partial r} - \dfrac{\partial N_1(-1)}{\partial r} \\ -\dfrac{\partial N_2(-1)}{\partial r} \end{Bmatrix} = 0 \tag{3-17}$$

Additionally, the basis functions should form a partition of unity, $\sum_{i=0}^{2} N_i = 1$. This provides another independent equation. Using the nine independent equations, the nine coefficients can be solved. The basis function can be stated as follows

$$\begin{Bmatrix} N_0 \\ N_1 \\ N_2 \end{Bmatrix} = \begin{bmatrix} \frac{1}{8} & -\frac{1}{4} & \frac{1}{8} \\ \frac{3}{4} & 0 & -\frac{1}{4} \\ \frac{1}{8} & \frac{1}{4} & \frac{1}{8} \end{bmatrix} \begin{Bmatrix} 1 \\ r \\ r^2 \end{Bmatrix} \tag{3-18}$$

The B-spline element using these basis functions is called Quadratic B-spline element (QBS). Using the same approach, the B-spline basis functions with C^2 continuity can also be obtained. The B-spline element with the basis functions is defined as Cubic B-spline element (CBS).

Two and three dimensional B-spline elements are created by taking product of one dimensional B-spline elements. For example, 2D quadratic B-spline element has nine supports nodes and nine basis functions. 2D cubic B-spline element has sixteen supports nodes and sixteen basis functions.

Timoshenko Beam Example

Several elastostatic problems have been solved using IBFEM [13]-[16]. Here we provide one example for elastostatics from [15]. A cantilever beam with relatively large thickness is created. The length of 1.0m and the thickness of 0.2 m are used. According to Timoshenko beam theory, the tip deflection is given as $\delta_{tip} = \frac{P}{3EI}\left[\frac{1}{8}(4-5\nu)t^2L + L^3\right]$ where P is the applied load at the tip, E is the Young's modulus, I is the moment of the inertia of the beam cross section, ν is the Poisson's ratio, L is the length of the beam, t is the thickness of the beam.

Assuming that the material is isotropic, Young's modulus and Poisson ratio are defined as $E = 210GPa$, and $\nu = 0.25$. The uniform shear load of $-0.1MPa$ is applied at the tip. The expected tip deflection is $-4.8869\times10^{-5}m$ using the Timoshenko beam theory.

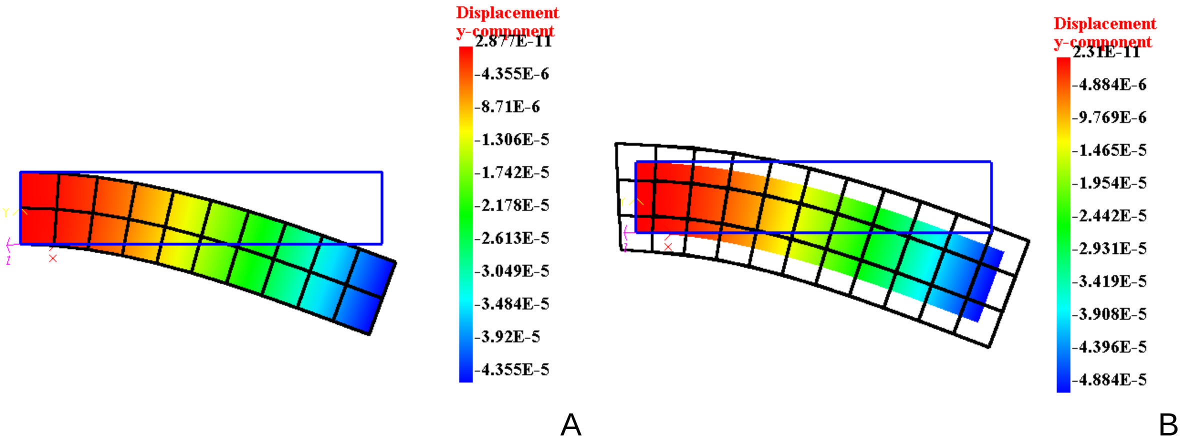

Figure 3-3. Displacement surface plots in y-component. A) Using 4 node bilinear elements B) Using 9 node B-spline elements

Figure 3-3 shows displacement contours using two element types. In the case of Figure 3-3 B, where quadratic B-spline elements are used, the computed tip displacement is much closer to the analytical solution.

CHAPTER 4
IMPLICIT BOUNDARY FINITE ELEMENT METHOD FOR 2D MAGNETOSTATICS

Solution Structure for 2D Magnetostatics

Under magneto static or quasistatic assumption, if material is homogenous and isotropic, and only current induces the magnetic field, the governing equation is

$$\nabla \times \mu^{-1}(\nabla \times \mathbf{A}) = \mathbf{J} \tag{4-1}$$

where, $\mathbf{A}$ is the magnetic vector potential, μ is the permeability of a material and $\mathbf{J}$ is the current density vector. The constitutive equation is defined as

$$\mathbf{H} = \frac{1}{\mu}\mathbf{B} = \frac{1}{\mu}\left(\nabla \times \mathbf{A}\right) \tag{4-2}$$

where, $\mathbf{B}$ is the magnetic flux density and $\mathbf{H}$ is the magnetic field density.

Figure 4-1 shows 2D assumption where, $\mathbf{J} = J(x,y)\hat{\mathbf{k}}$, and $\mathbf{A} = A(x,y)\hat{\mathbf{k}}$. That is, the current only flows in the z-direction and the magnetic potential only exists on the direction normal to the plane of analysis. The magnetic flux density and the magnetic field are vector fields in the plane x-y.

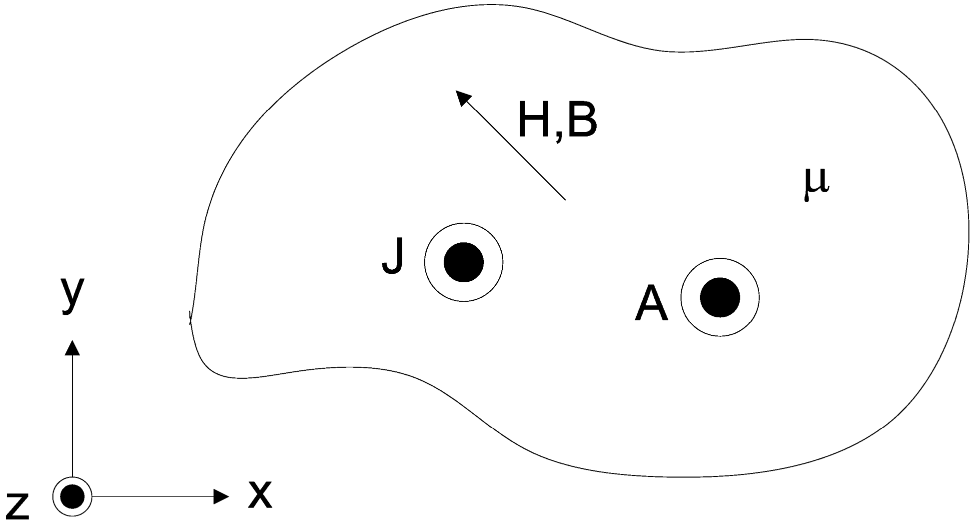

Figure 4-1. 2D magnetostatic problem

If the material is homogeneous, Equation 4-1 is expressed as the gradient of the scalar function A as following

$$\nabla \cdot \left(\frac{1}{\mu} \nabla A \right) = \frac{\partial}{\partial x}\left(\frac{1}{\mu} \frac{\partial A}{\partial x} \right) + \frac{\partial}{\partial y}\left(\frac{1}{\mu} \frac{\partial A}{\partial y} \right) = -J \qquad (4\text{-}3)$$

The constitutive equation for the 2D problem can be rewritten as

$$\mathbf{H} = \frac{1}{\mu}\mathbf{B} = \frac{1}{\mu}\left(\frac{\partial A}{\partial y}\hat{\mathbf{i}} - \frac{\partial A}{\partial x}\hat{\mathbf{j}} \right) \qquad (4\text{-}4)$$

The solution structure for the magnetic vector potential $\mathbf{A}$ is defined as

$$A(\mathbf{x}) = D(\mathbf{x})A^g(\mathbf{x}) + A^a(\mathbf{x}) = A^s(\mathbf{x}) + A^a(\mathbf{x}) \qquad (4\text{-}5)$$

where, A^g is a grid variable that is defined by piece-wise interpolation or using B-spline approximation over a structured grid. A^a is the boundary value function which has a value equal to the prescribed boundary conditions at the boundaries, $D(\mathbf{x})$ is a weighting function defined such that $D(\mathbf{x}) = 0$ at boundaries where essential boundary conditions are applied so that $A(\mathbf{x}){=}A^a(\mathbf{x})$ at these boundaries. The boundary value function A^a is constructed by interpolating nodal values within elements. The nodal values are selected such that at the boundary it has a value equal to the specified boundary condition.

Using the weighted residual method with the solution structure in Equation 4-3, the weak form for 2D magnetostatics is obtained as

$$\int_\Omega \nabla(\delta A^s)\mu^{-1}\nabla(A^s)d\Omega = \int_\Omega (\delta A^s)Jd\Omega + \int_\Gamma (\delta A^s)H_t\delta\Gamma - \int_\Omega \nabla(\delta A^s)\mu^{-1}\nabla(A^a)d\Omega \qquad (4\text{-}6)$$

where, $\delta\mathrm{A}^s$ is the virtual magnetic potential vector and H_t is the tangential component of the magnetic field.

Finite Element Formulation for 2D Magnetostatics

The grid variable A^g is interpolated within each element as $A^g = \{\mathbf{N}\}^T \{\mathbf{A}^g\}$ where, $\{\mathbf{N}\}^T$ is a row matrix containing the shape functions and $\{\mathbf{A}^g\}$ is a column matrix containing the nodal values of the grid variable. Similarly, the boundary value function is represented within each element as $A^a = \{\mathbf{N}\}^T \{\mathbf{A}^a\}$ where, $\{\mathbf{A}^a\}$ is column matrix containing the nodal values assigned such that A^a has the prescribed value at the boundary. Note that the same shape functions are used to interpolate A^g and A^a. If all the essential boundary conditions are homogeneous, so that $A=0$ is the only prescribed boundary condition, then the boundary value function A^a is zero everywhere and can be eliminated from the solution structure. Otherwise, nodes near the boundary are assigned values of A^a equal to the prescribed value. For 2D problems, the gradients of the boundary value function A^a is expressed as

$$\nabla A^a = \left\{ \frac{\partial A^a}{\partial x_1} \quad \frac{\partial A^a}{\partial x_2} \right\}^T = \sum_i \frac{\partial N_i}{\partial x_j} A_i^a = [\mathbf{B}]\{\mathbf{A}^a\} \tag{4-7}$$

The gradient of the homogenous part of the solution $\mathbf{A}^s$ is stated as

$$\nabla A^s = \left\{ \frac{\partial A^s}{\partial x_1} \quad \frac{\partial A^s}{\partial x_2} \right\}^T = \sum_i \left(D\frac{\partial N_i}{\partial x_j} + N_i \frac{\partial D}{\partial x_j} \right) A_i^g = [\bar{\mathbf{B}}]\{\mathbf{A}^g\} \tag{4-8}$$

Using Equations 4-7 and 4-8, the weak form is rewritten as

$$\begin{aligned} &\sum_{i=1}^{NE} \left\{\delta \mathbf{A}^g\right\}^T \int_{\Omega_e} \left[\bar{\mathbf{B}}\right]^T \mu^{-1} \left[\bar{\mathbf{B}}\right] \left\{\mathbf{A}^g\right\} d\Omega_e \\ &= \sum_{i=1}^{NE} \left\{\delta \mathbf{A}^g\right\}^T \int_{\Omega_e} \left[\mathbf{N}\right]^T J d\Omega_e + \sum_{i=1}^{NBE} \left\{\delta \mathbf{A}^g\right\}^T \int_{\Gamma} \left[\mathbf{N}\right]^T H_t d\Gamma - \sum_{i=1}^{NE} \left\{\delta \mathbf{A}^g\right\}^T \int_{\Omega_e} \left[\bar{\mathbf{B}}\right]^T \mu^{-1} \left[\mathbf{B}\right] \left\{\mathbf{A}^a\right\} d\Omega_e \end{aligned} \tag{4-9}$$

where, NE is the total number of grid elements and NBE is the number of grid elements on the natural boundary. $[\bar{\mathbf{B}}]$ is decomposed into two matrices $[\bar{\mathbf{B}}_1]$ and $[\bar{\mathbf{B}}_2]$ such that only $[\bar{\mathbf{B}}_2]$ contains derivates of the D-function which can have very large values near the boundary. They are expressed as

$$[\bar{\mathbf{B}}_1] = \bar{B}_{ij}^1 = D\frac{\partial N_i}{\partial x_j} \tag{4-10}$$

$$[\bar{\mathbf{B}}_2] = \bar{B}_{ij}^2 = N_i \frac{\partial D}{\partial x_j} \tag{4-11}$$

The element matrix to be assembled into the global equations can be obtained as

$$\left[\mathbf{K}^e\right] = \int_{\Omega_e} \left[\bar{\mathbf{B}}\right]^T \mu^{-1} \left[\bar{\mathbf{B}}\right] d\Omega_e = \left[\mathbf{K}_1^e\right] + \left[\mathbf{K}_2^e\right] + \left[\mathbf{K}_3^e\right] \tag{4-12}$$

$$\left[\mathbf{K}_1^e\right] = \int_{\Omega_e} \left[\bar{\mathbf{B}}_1\right]^T \mu^{-1} \left[\bar{\mathbf{B}}_1\right] d\Omega_e \tag{4-13}$$

$$\left[\mathbf{K}_2^e\right] = \int_{\Omega_e} \left[\bar{\mathbf{B}}_2\right]^T \mu^{-1} \left[\bar{\mathbf{B}}_2\right] d\Omega_e \tag{4-14}$$

$$\left[\mathbf{K}_3^e\right] = \int_{\Omega_e} \left(\left[\bar{\mathbf{B}}_1\right]^T \mu^{-1} \left[\bar{\mathbf{B}}_2\right] + \left[\bar{\mathbf{B}}_2\right]^T \mu^{-1} \left[\bar{\mathbf{B}}_1\right]\right) d\Omega_e \tag{4-15}$$

As $\left[\bar{\mathbf{B}}_2\right]$ has terms containing derivatives of the D-function, it is non-zero only within the narrow transition band near the boundary. Therefore, for all internal elements and boundary elements without essential boundary conditions $\left[\mathbf{K}_2^e\right]$ and $\left[\mathbf{K}_3^e\right]$ are zero. For boundary elements $\left[\mathbf{K}_1^e\right]$ is evaluated by subdividing these elements into triangles and integrating only within triangles that are inside the geometry. For boundary elements with boundary conditions, the volume integral for computing $\left[\mathbf{K}_2^e\right]$ and $\left[\mathbf{K}_3^e\right]$ can be converted to surface integrals because they contain $\left[\bar{\mathbf{B}}_2\right]$ which is non-zero only within the narrow transition band near the boundary. The components of $\left[\mathbf{K}_2^e\right]$, can be expressed using index notation as

$$\left[\mathbf{K}_2^e\right] = \int_{\Omega_e} \begin{bmatrix} N_1\mu^{-1}N_1 & \cdots & N_1\mu^{-1}N_N \\ & \ddots & \vdots \\ SYM & & N_N\mu^{-1}N_N \end{bmatrix} \left(\left(\frac{\partial D}{\partial x}\right)^2 + \left(\frac{\partial D}{\partial y}\right)^2 \right) d\Omega_e$$

$$= \int_{\Gamma_e} \begin{bmatrix} N_1\mu^{-1}N_1 & \cdots & N_1\mu^{-1}N_N \\ & \ddots & \vdots \\ SYM & & N_N\mu^{-1}N_N \end{bmatrix} \left(\int \left(\left(\frac{\partial D}{\partial x}\right)^2 + \left(\frac{\partial D}{\partial y}\right)^2 \right) dn \right) d\Gamma_e \tag{4-16}$$

where, dn is the increment on the normal direction of the boundary. Using index notation, the above equation is rewritten as

$$K_{2ij}^e = \int_{\Gamma_e} N_i \mu^{-1} N_j \Delta d\Gamma_e \tag{4-17}$$

where,

$$\Delta = \left(\int_0^\delta \sum_k \left(\frac{\partial D}{\partial x_k}\right)^2 \frac{1}{|\nabla\phi|} d\phi \right) \tag{4-18}$$

In the preceding equation, the volume integral in $\left[\mathbf{K}_2^e\right]$ has been converted into a combination of surface integral along the boundary and an integration over ϕ. Similarly, the third term, $\left[\mathbf{K}_3^e\right]$, can be stated using the index notation as

$$K_{3ij}^e = \int_{\Gamma_e} \sum_k \left(\frac{\partial N_i}{\partial x_k} \mu^{-1} N_j + \frac{\partial N_j}{\partial x_k} \mu^{-1} N_i \right) \Delta_k d\Gamma_e \tag{4-19}$$

where,

$$\Delta_k = \left(\int_0^\delta D \frac{\partial D}{\partial x_k} \frac{1}{|\nabla\phi|} d\phi \right) \tag{4-20}$$

All element stiffness matrices of $\left[\mathbf{K}_1^e\right]$, $\left[\mathbf{K}_2^e\right]$, and $\left[\mathbf{K}_3^e\right]$ are evaluated using Gaussian quadrature. For surface integrals, the boundary within element is approximately by sufficiently small straight line segments to achieve accuracy.

Solution Structure for 2D Magnetostatics with Permanent Magnet

When permanent magnets exist on analysis domain, a different constitutive equation is used for the domain with the permanent magnets. The permanent magnetic domain has the magnetization vector, $\mathbf{M}_0$ being a part of constitutive equation. The constitutive equation can be stated as

$$\mathbf{B} = \mu_0 \mu_r \mathbf{H} + \mu_0 \mathbf{M}_0 \tag{4-21}$$

where, $\mathbf{M}_0$ is the magnetization vector, μ_0 is the vacuum permeability called magnetic constant $4\pi \times 10^{-7}\,\mathrm{H/m}$, μ_r is the relative permeability which is the ratio of the permeability of a medium to μ_0. The magnetic field can be expressed as

$$\mathbf{H} = \frac{1}{\mu_0 \mu_r}\mathbf{B} - \frac{1}{\mu_r}\mathbf{M}_0 = \nu \mathbf{B} - \nu \mu_0 \mathbf{M}_0 \tag{4-22}$$

where, $\nu = \dfrac{1}{\mu_0 \mu_r}$ is the reluctivity. If the value of the reluctivity becomes constant, then the governing equation is restated as

$$\nabla \times \left(\nu \nabla \times \mathbf{A} - \nu \mu_0 \mathbf{M}_0 \right) = \mathbf{J} \tag{4-23}$$

The equation becomes a nonlinear Poisson’s equation for the vector potential. Multiplying the weight function $\delta \mathbf{A}$ on both sides and integrating, Equation 4-23 becomes

$$\int_\Omega \nabla \times (\nu \nabla \times \mathbf{A} - \nu \mu_0 \mathbf{M}_0) \cdot \delta \mathbf{A} d\Omega = \int_\Omega \mathbf{J} \cdot \delta \mathbf{A} d\Omega \tag{4-24}$$

Using Green’s first identity for vector fields, the left hand side term becomes

$$\begin{aligned} &\int_\Omega \nabla \times (\nu \nabla \times \mathbf{A} - \nu \mu_0 \mathbf{M}_0) \cdot \delta \mathbf{A} d\Omega = \\ &\int_\Omega (\nu \nabla \times \mathbf{A} - \nu \mu_0 \mathbf{M}_0) \cdot \left(\nabla \times \delta \mathbf{A} \right) d\Omega + \int_\Omega \nabla \cdot (\nu \nabla \times \mathbf{A} - \nu \mu_0 \mathbf{M}_0) \times \delta \mathbf{A} d\Omega \end{aligned} \tag{4-25}$$

Using the divergence theorem, the second term on the right hand side becomes

$$\int_{\Omega} \nabla \cdot (\nu\nabla \times \mathbf{A} - \nu\mu_0\mathbf{M}_0) \times \delta\mathbf{A} d\Omega = \int_{\Gamma} \left((\nu\nabla \times \mathbf{A} - \nu\mu_0\mathbf{M}_0) \times \delta\mathbf{A} \right) \cdot \mathbf{n} d\Gamma \, . \tag{4-26}$$

Using the identities of $F \times G = -G \times F$, and $(F \times G) \cdot T = F \cdot (G \times T)$, Equation 4-26 becomes

$$\int_{\Gamma} \left\{ (\nu\nabla \times \mathbf{A} - \nu\mu_0\mathbf{M}_0) \times \delta\mathbf{A} \right\} \cdot \mathbf{n} d\Gamma = \int_{\Gamma} \delta\mathbf{A} \cdot \left\{ (\nu\nabla \times \mathbf{A} - \nu\mu_0\mathbf{M}_0) \times \mathbf{n} \right\} d\Gamma \tag{4-27}$$

The weak form becomes

$$\begin{aligned} &\int_{\Omega} (\nabla \times \delta\mathbf{A}) \cdot (\nu\nabla \times \mathbf{A}) d\Omega \\ &= \int_{\Omega} (\nabla \times \delta\mathbf{A}) \cdot (\nu\mu_0\mathbf{M}_0) d\Omega - \int_{\Gamma} \delta\mathbf{A} \cdot \left\{ (\nu\nabla \times \mathbf{A} - \nu\mu_0\mathbf{M}_0) \times \mathbf{n} \right\} d\Gamma + \int_{\Omega} \mathbf{J}\delta\mathbf{A} d\Omega \end{aligned} \tag{4-28}$$

When a homogenous Neumann boundary condition is applied on the boundary, the tangential component of **H**, $\mathbf{H}_t = (\nu\nabla \times \mathbf{A} - \nu\mu_0\mathbf{M}_0) \times \mathbf{n}$, is set equal to zero. Thus, the line integral can be ignored. The weak form can be rewritten as

$$\int_{\Omega} (\nabla \times \delta\mathbf{A}) \cdot (\nu\nabla \times \mathbf{A}) d\Omega = \int_{\Omega} (\nabla \times \delta\mathbf{A}) \cdot (\nu\mu_0\mathbf{M}_0) d\Omega + \int_{\Omega} \mathbf{J}\delta\mathbf{A} d\Omega \tag{4-29}$$

In case of the 2D magnetostatic problem, the magnetic vector potential and the current density have only z components and the magnetization vector is in the xy- plane as shown in Figure 4-2.

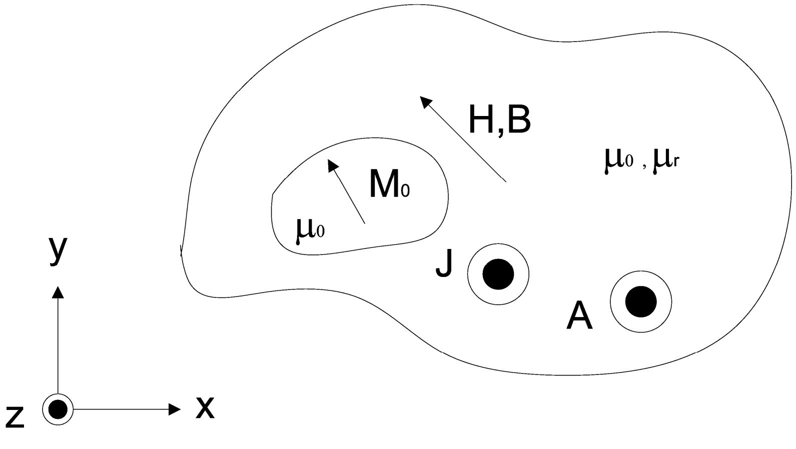

Figure 4-2. 2D magnetostatic problem with permanent magnet

The 2D weak form becomes

$$\int_{\Omega}\left(\nabla\cdot\delta\mathrm{A}\right)\cdot\left(\nu\nabla\cdot\mathrm{A}\right)d\Omega=\int_{\Omega}\left(\nabla\times\delta\mathrm{A}\right)\cdot\left(\nu\mu_0\mathbf{M}_0\right)d\Omega+\int_{\Omega}\mathbf{J}\delta\mathrm{A}d\Omega \tag{4-30}$$

If $\mathbf{M}_0=M_x\mathbf{i}+M_y\mathbf{j}$ and $\nabla\times\delta\mathrm{A}=\begin{vmatrix}\mathbf{i} & \mathbf{j} & \mathbf{k}\\ \frac{\partial}{\partial x} & \frac{\partial}{\partial y} & \frac{\partial}{\partial z}\\ 0 & 0 & \delta A\end{vmatrix}=\frac{\partial\delta A}{\partial y}\mathbf{i}-\frac{\partial\delta A}{\partial x}\mathbf{j}$, the weak form with permanent magnet can be rewritten as

$$\int_{\Omega}\left(\nabla\cdot\delta\mathrm{A}\right)\cdot\left(\nu\nabla\cdot\mathrm{A}\right)d\Omega=\int_{\Omega}\nu\mu_0\left(\frac{\partial\delta A}{\partial y}\cdot\mathrm{M_x}-\frac{\partial\delta A}{\partial x}\mathrm{M_y}\right)d\Omega+\int_{\Omega}\mathbf{J}\delta\mathrm{A}d\Omega \tag{4-31}$$

Using the solution structure of Equation 4-5, the weak form with permanent magnet is obtained as

$$\begin{aligned}&\int_{\Omega}\nabla(\delta\mathrm{A}^s)\mu^{-1}\nabla(\mathrm{A}^s)d\Omega\\&=\int_{\Omega}\nu\mu_0\left(\frac{\partial\delta A^s}{\partial y}\cdot\mathrm{M_x}-\frac{\partial\delta A^s}{\partial x}\mathrm{M_y}\right)d\Omega+\int_{\Omega}(\delta\mathrm{A}^s)Jd\Omega-\int_{\Omega}\nabla(\delta\mathrm{A}^s)\mu^{-1}\nabla(\mathrm{A}^a)d\Omega\end{aligned} \tag{4-32}$$

Solution Structure for Multiple Materials

When multiple materials are involved in the analysis, there can be discontinuity in the magnetic field at the interface even though **A** is continuous. To allow discontinuity in the magnetic field, separate grids are used for each material as shown in Figure 4-3.

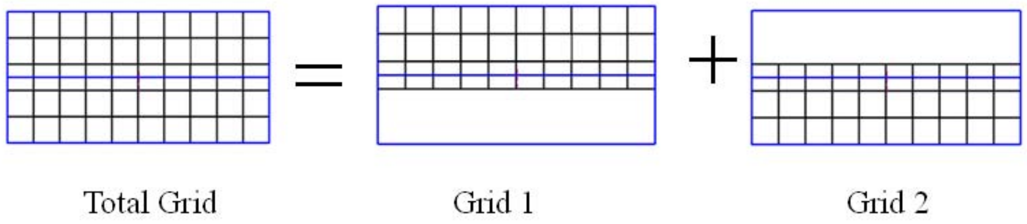
Total Grid

Grid 1

Grid 2

Figure 4-3. Two grids for two materials

At the interface the elements from neighboring grids overlap. A solution structure is needed for these overlapping elements to ensure that *A* is continuous while flux density **B** and magnetic field **H** can be discontinuous. Burla et al [16] suggested a modified solution structure using two different structured grids and solved an elastostatic problem for composite microstructures. According to [16], the modified solution structure at the material interface boundary is called *interface solution structure* as shown below

$$A^{g} = \left(1 - D\left(\phi(\mathbf{x})\right)\right) A^{g1} + D\left(\phi(\mathbf{x})\right) A^{g2} \tag{4-33}$$

where, A^{gi} is the field interpolated or approximated within the element from grid i, $(i = 1, 2)$, $D(\phi(\mathbf{x}))$ is the approximate step function and $\phi(\mathbf{x})$ is the implicit equation of the interface curve (represented using signed distance function). When the solution structure in Equation 4-33 is used in the weak form, element matrix for elements on the interface boundary contain terms that involve the gradient of $D(\phi(\mathbf{x}))$. The gradient of $D(\phi(\mathbf{x}))$ is very large near the interface. The terms in the volume integral for computing the element matrix are separated into those that contain the gradient of the shape functions and those that contain the gradient of the D-function. As explained earlier for elements on the external boundaries, the gradient of the D-function is zero outside a narrow band near the interface boundaries. Therefore, the volume integral for terms containing the gradient of the D-function can be converted into surface integrals for efficient computation. These techniques are described in detail in [16] for elastostatics and have been adopted here for magnetostatics. Moreover, these techniques have been extended to solve multi-material problems with more than two materials in this study.

At the interface between materials with different magnetic permeability, the required interface conditions, expressed in terms of the magnetic vector potential are

$$\mathbf{n}\times\left(\nu_1\nabla\times\mathbf{A}_1\right)=\mathbf{n}\times\left(\nu_2\nabla\times\mathbf{A}_2\right) \tag{4-34}$$

$$\mathbf{n}\cdot\left(\nabla\times\mathbf{A}_1\right)=\mathbf{n}\cdot\left(\nabla\times\mathbf{A}_2\right) \tag{4-35}$$

which means the tangential component of the magnetic field and the normal component of magnetic flux density are continuous. It is obvious that if the magnetic vector potential is continuous, that is $\mathbf{A}_1=\mathbf{A}_2$, then the interface condition (Equation 4-35) is automatically satisfied. However, the normal component of magnetic field and the tangential component of flux density can be discontinuous. To allow this discontinuity in the magnetic field and the magnetic flux density, separate grids are used for each material. Using two grids, the solution structure in Equation 4-33 combines the interpolation within the overlapping elements at an interface to represent the solution near the interface. When the D-function in unity, the solution is given by $A=A^{g2}$, which is the solution from the second grid and when the D-function is zero, the solution is given $A=A^{g1}$, which is the solution from first grid. In the region where the D-function varies from zero to unity, the solution is a blend of the solutions from the two grids. This way of constructing the solution structure ensures the continuity of the solution throughout the analysis domain. It also allows the derivative (and magnetic field and flux density) to be discontinuous at the interface. This property can be seen from the gradients of the solution structure as shown below

$$\frac{\partial A^g}{\partial x_j}=\left(\left(1-D\right)\frac{\partial A^{g1}}{\partial x_j}-\frac{\partial D}{\partial x_j}A^{g1}+D\frac{\partial A^{g2}}{\partial x_j}+\frac{\partial D}{\partial x_j}A^{g2}\right) \tag{4-36}$$

In this expression, the first term and the third term are continuous at the interface boundary while the second term and the fourth term are discontinuous at the interface boundary because the gradient of the D-function is zero for $\phi < 0$ and non-zero for $0 < \phi < \delta$. Therefore, these terms provide independent slopes on the two sides of the interface allowing discontinuous flux density when necessary and at the same time producing a continuous flux density if $A^{g1} = A^{g2}$.

Figure 4-4 graphically shows plots of components for the interface solution structure at the material interface boundary. Figure 4-4 A and B are weight functions for the grid 1 and the grid 2. When the solution structure behaves like a sinusoidal function, Figure 3-7 C and D represents A field distributions from the grid 1 and the grid 2.

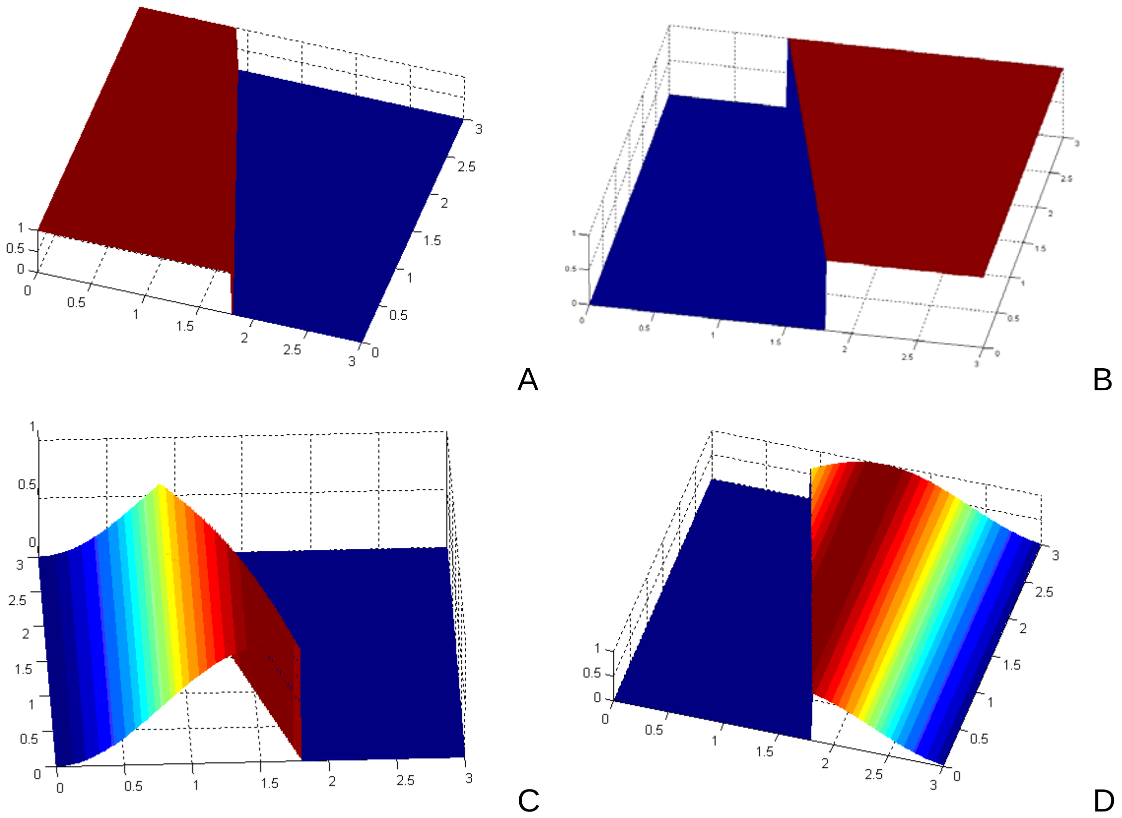

Figure 4-4. Component plots of interface solution structure at the material boundary. A) $1-D(\phi)$, B) $D(\phi)$, C) $\left(1-D(\phi)\right)A^{g1}$, and D) $D(\phi)A^{g2}$

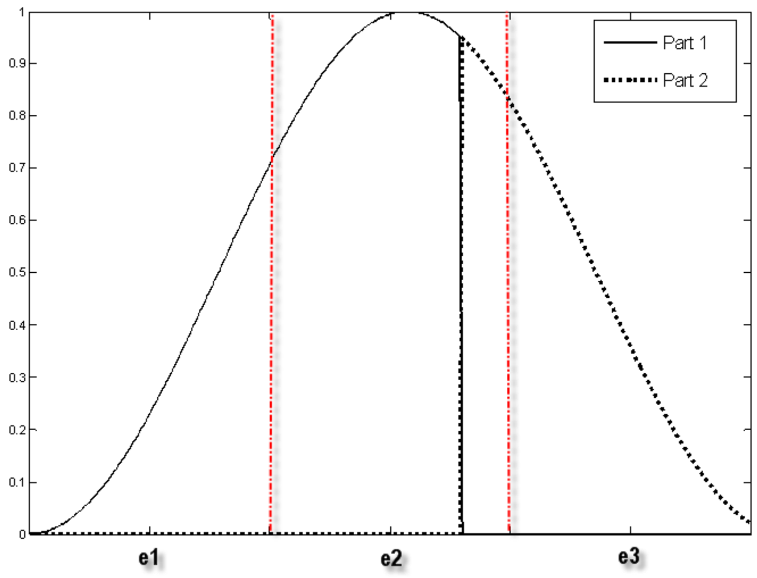

Figure 4-5. Interface solution structure at the material boundary

Figure 4-5 shows the interface solution structure at the material boundary following by Figure 4-4. The x-axis and the y-axis represent grid elements and the field value. Part 1 and Part 2 represents the grid 1 and the grid 2. Elements of e1 and e2 belong to Part 1 and elements of e2 and e3 belong to Part2. The element e2 is from each grid overlapping at the interface and the solution structure is used to blend solution from the two grids.

In order to apply the interface solution structure to a model containing more than three materials, preprocessing is required to create a contact list containing contact pairs. Each contact pair associated with two materials is predefined and then the interface solution structure can be applied at the interface boundary based on each contact pair.

Three parts with own grids are shown in Figure 4-6. For the first part (Figure 4-6 A), three boundary elements belong to the interface boundary elements. One boundary element belongs to the outer boundary elements. For the third part (Figure 4-6 C), three boundary elements belong to the interface boundary elements. Five boundary elements are outer boundary elements. Remained elements are inner elements.

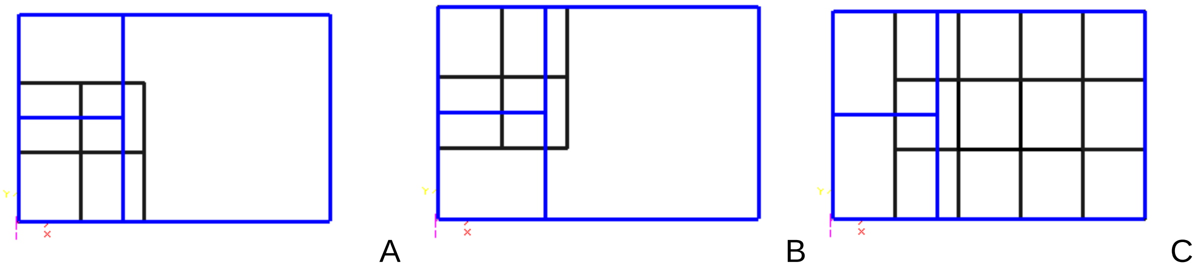

Figure 4-6. Three parts with each own grid. A) Part 1 with the grid 1, B) Part 2 with the grid 2, and C) Part 3 with the grid 3.

Using the interface boundary elements of each part, three contact pairs are defined. One is the pair of the 1st part and the 2nd part, which is defined as contact 1. Another is the pair of the 1st part and the 3rd part, which is defined as Contact 2. The last one is the pair of the 2nd part and the 3rd part, which is defined as Contact 3. These pairs are shown in Figure 4-7.

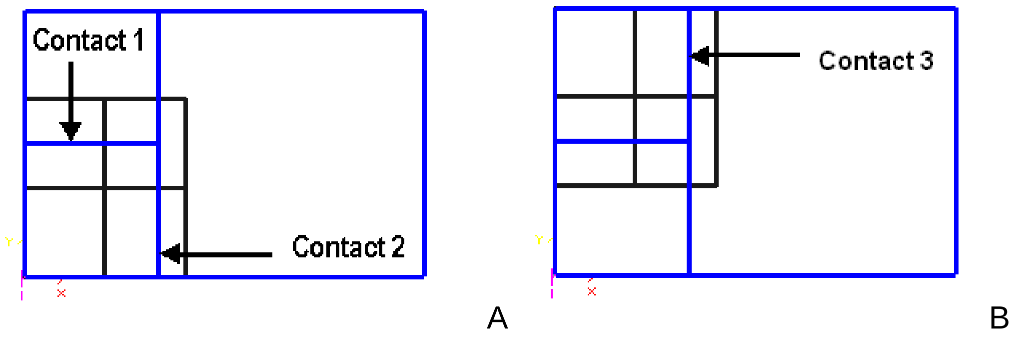

Figure 4-7. Contact pairs. A) Contact 1 and Contact 2, and B) Contact 3

For the contact pairs, the interface solution structure can be applied. Figure 4-8 shows four elements for the first part. For the outer boundary element e1, the solution structure is applied. For the other elements from e2 to e4, the interface solution structure can be applied.

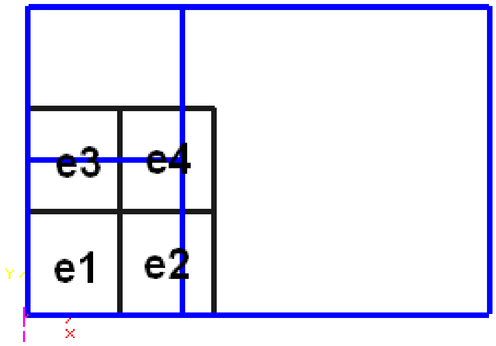

Figure 4-8. Four elements in Part 1

In order to express several interface boundaries among multi-materials, the D-function is redefined as $D_{ij}(\phi)$ where the subscripts i and j indicates the i th and the j th grids or parts. So then the generalized interface solution structure is restated as

$$A^{g} = \left(1 - D_{\mathrm{ij}}(\phi)\right) A^{g_i} + D_{\mathrm{ij}}(\phi) A^{g_j} \tag{4-37}$$

As the element e2 has the 2nd contact pair, the interface solution structure becomes

$$A^{g} = \left(1 - D_{13}(\phi)\right) A^{g_1} + D_{13}(\phi) A^{g_3} \tag{4-38}$$

where, $D_{13}(\phi)$ is the D-function with the interface boundary between the 1st grid and the 3rd grid. Similarly as the element e3 is related to the 1st contact pair, the interface solution structure is

$$A^{g} = \left(1 - D_{12}(\phi)\right) A^{g_1} + \mathrm{H}_{12}(\phi) A^{g_2} \tag{4-39}$$

As the element e4 is linked to the 1st and 2nd contact pairs, the interface solution structure can be stated as

$$A^{g} = \left(1 - D_{13}(\phi)\right) A^{g_1} + D_{13}(\phi) A^{g_3} + \left(1 - D_{12}(\phi)\right) A^{g_1} + D_{12}(\phi) A^{g_2} \tag{4-40}$$

Magnetic Force Computation

Several techniques for computing magnetic forces can be found in literature [25]-[30]. These include the virtual work principle [25]-[28], Maxwell's stress tensor method, equivalent source method, the force density method to list a few. These approaches have been implemented using FEM and therefore can be used with IBFEM. Assuming that the exact equation of the surface is available (preferable as a parametric equation), it is easier to implement a method that integrates surface force densities to compute the nodal force. The weak form for solid mechanics problems is the principle of virtual work, which can be stated as follows:

$$\int_{\Omega} \{\boldsymbol{\delta\varepsilon}\}^{T} [\mathbf{C}] \{\boldsymbol{\varepsilon}\} \, d\Omega = \int_{\Omega} \mathbf{f}_{m} \cdot \boldsymbol{\delta}\mathbf{u} d\Omega + \int_{\Gamma} \mathbf{t} \cdot \boldsymbol{\delta}\mathbf{u} d\Gamma \tag{4-41}$$

where, $[\mathbf{C}]$ is the stiffness matrix, $\{\boldsymbol{\varepsilon}\}$ is the strain matrix, $\mathbf{t}$ is the traction force on specified surface, and $\mathbf{f}_m$ is the magnetic force density. The force density is defined as follows

In a current carrying conductor, the force due to magnetic field is the Lorentz force, given by

$$\mathbf{f}_c = \mathbf{J} \times \mathbf{B} \tag{4-42}$$

where, $\mathbf{B}$ is the magnetic flux density. In a linear, isotropic and non-compressible ferromagnetic material,

$$\mathbf{f}_f = \frac{1}{2} H^2 \nabla \mu \tag{4-43}$$

The virtual work done by the force densities can be evaluated as follows:

$$\int_{\Omega} \mathbf{f}_m \cdot \boldsymbol{\delta}\mathbf{u} d\Omega = -\int_{\Omega} \frac{1}{2} H^2 \nabla \mu \boldsymbol{\delta}\mathbf{u} d\Omega + \int_{\Omega} (\mathbf{J} \times \mathbf{B}) \cdot \boldsymbol{\delta}\mathbf{u} d\Omega \tag{4-44}$$

The Lorentz force is evaluated easily as the body force term. The equivalent nodal forces due to this body force can be computed by integrating the virtual work over the volume of each element as follows

$$\left\{\mathbf{F}_b\right\} = \int_{\Omega_e} \left[\mathbf{N}\right]^T \left(\mathbf{J}\times\mathbf{B}\right) d\Omega \tag{4-45}$$

The volume integration of each element is evaluated using Gaussian quadrature.

To compute the force on the ferromagnetic materials, the volume integral of the force density $\mathbf{f}_f$ must be changed to surface integral. For a ferromagnetic object with permeability, μ_1, surrounded by a medium whose permeability is μ_2, the permeability can be considered to change from one value to the other over a band along the boundary whose width, measured in the normal direction, is Δn. The limit of $\Delta n \to 0$ represents the discontinuous variation at the boundary. The gradient of the permeability within this band can then be written as

$$\nabla\mu = \frac{\partial\mu}{\partial n}\hat{\mathbf{n}} \tag{4-46}$$

where, $\hat{\mathbf{n}}$ is the direction normal to the boundary between the two materials with different permeability as shown in Figure 4-9.

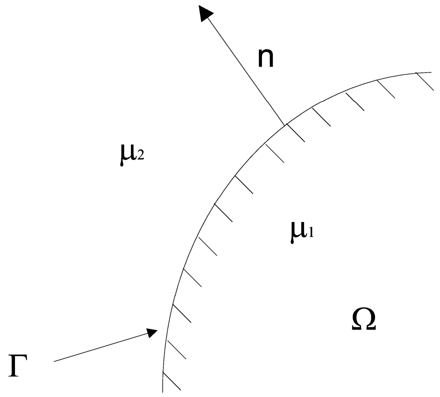

Figure 4-9. Material interface boundary: μ_1 (Inner material permeability) and μ_2 (Outer material permeability)

Using Equation 4-46, the force on the ferromagnetic material is expressed as

$$\begin{aligned}-\frac{1}{2}\int_{\Omega}\boldsymbol{\delta}\mathbf{u}^{\mathbf{T}}\left(\nabla\mu\left(\mathbf{H}\cdot\mathbf{H}\right)\right)d\Omega &= \int_{\Gamma}\int_{0}^{\Delta n}\left[-\frac{1}{2}(\mathbf{H}\cdot\mathbf{H})\frac{\partial\mu}{\partial n}\hat{\mathbf{n}}\right]dn\delta\mathbf{u}d\Gamma \\ &= \int_{\Gamma}\int_{\mu_1}^{\mu_2}\left[-\frac{1}{2}(\mathbf{H}\cdot\mathbf{H})\hat{\mathbf{n}}\right]d\mu\delta\mathbf{u}d\Gamma\end{aligned} \tag{4-47}$$

The surface force density term can be evaluated by expressing the square of magnetic field as a function of permeability. If there is no surface current then the tangential component of the magnetic field $\mathbf{H}_t$ does not vary across the boundary and can be treated as a constant. Similarly, the normal component of the magnetic flux density $\mathbf{B}_n$ is constant (by Gauss's law) and does not vary across the boundary even though the permeability is different on the two sides of the boundary. The square of the magnetic field can be expressed as the sum of the squares of the tangential component of the magnetic field $\mathbf{H}_t$ and the normal component of the magnetic flux $\mathbf{B}_n$ as

$$\mathbf{H}\cdot\mathbf{H} = H^2 = H_t^2 + \frac{{B_n}^2}{\mu^2} \tag{4-48}$$

Both the tangential component of magnetic field and the normal component of the magnetic flux density can be treated as constants for the integration in computing surface traction since these quantities do not vary in the direction normal to the interface between the two materials. Using the preceding equation for the square of magnetic field to compute the surface traction due to magnetic forces, Equation 4-47 is rewritten as

$$\int_{\Gamma}\left(-\frac{1}{2}\int_{\mu_2}^{\mu_1}\left(H_t^2+\frac{B_n^2}{\mu^2}\right)\hat{\mathbf{n}}d\mu\right)\delta\mathbf{u}d\Gamma = \int_{\Gamma}\delta\mathbf{u}\left[-\frac{1}{2}({H_t}^2(\mu_2-\mu_1))+\frac{1}{2}{B_n}^2\left(\frac{1}{\mu_2}-\frac{1}{\mu_1}\right)\right]\hat{\mathbf{n}}d\Gamma \tag{4-49}$$

As the material is assumed to be linear, H_t can easily be changed to B_t using the constitutive equation. The surface force density can be shown to be equal to

$$\mathbf{f}_s = \left[\frac{1}{2}\left(\frac{B_t^2}{\mu_1} - \frac{B_n^2}{\mu_1} \right)\hat{\mathbf{n}}_1 + \frac{1}{2}\left(\frac{B_t^2}{\mu_2} - \frac{B_n^2}{\mu_2} \right)\hat{\mathbf{n}}_2 \right] \tag{4-50}$$

where, μ_i and $\hat{\mathbf{n}}_i$ are the permeability and the outward normal vector of the *i*th material. If $\mu_2 < \mu_1$ it follows that $\mathbf{f}_s < 0$ therefore the direction of the surface traction $\mathbf{f}_S$ is opposite to $\hat{\mathbf{n}}$, which means that it acts in the direction of decreasing permeability. According to [30] an expression similar to Equation 4-50 has been deduced for the surface force densities between two linear media from a more general expression for magnetic force. The nodal forces at the boundary elements of each grid can be computed by integrating over the piece of the boundary that passes through the element. In other words, for a boundary element whose material property is μ_i the nodal forces are computed as:

$$\{\mathbf{F}_s\} = \int_{\Gamma_e} [\mathbf{N}]^T \frac{1}{2}\left(\frac{B_t^2}{\mu_i} - \frac{B_n^2}{\mu_i} \right)\hat{\mathbf{n}}_i d\Gamma \tag{4-51}$$

The boundary passing through each element is approximated by lines (2D) or triangles (3D) for the purpose of integration and Gaussian quadrature was used along each line segment or triangle.

CHAPTER 5
IMPLICIT BOUNDARY FINITE ELEMENT METHOD FOR 3D MAGNETOSTATICS

Governing Equation and Weak Form for 3D Magnetostatics

Several alternate formulations have been proposed in literature for 3D magnetostatic analysis using finite element method [31]-[39]. A formulation based on magnetic vector potential, **A**, is used in this study. The governing equations for 3D magnetostatics can be expressed in terms of magnetic vector potential as

$$\nabla\times\left(\nu\nabla\times\mathbf{A}\right)=\mathbf{J} \qquad \text{in } \Omega \tag{5-1}$$

where, Ω is the domain of analysis. The boundary of the analysis domain Γ consists of regions with specified natural boundary conditions and regions that are open boundaries, which are used to artificially truncate the analysis domain when in reality it extends to infinity. Often homogeneous essential boundary conditions are used on these open boundaries as an approximation if the boundary is far away from the sources. Several special techniques for modeling such open boundaries have been developed such as the infinite elements and asymptotic boundary condition [40]. Natural boundary conditions can be applied on boundaries (denoted as Γ_{H}) with known tangential component of the magnetic field or on boundaries (denoted as Γ_{B}) with known normal component of the flux density. If these boundaries are planes of symmetry then $\mathbf{n}\cdot\left(\nabla\times\mathbf{A}\right)=0$ on Γ_{B} and $\mathbf{n}\times\left(\nu\nabla\times\mathbf{A}\right)=0$ on Γ_{H}. To ensure uniqueness of the solution, the following essential boundary conditions are used to enforce these conditions [33].

$$\mathbf{n}\times\mathbf{A}=0 \qquad \text{on } \Gamma_{\mathrm{B}} \tag{5-2}$$

$$\mathbf{n}\cdot\mathbf{A}=0 \qquad \text{on } \Gamma_{\mathrm{H}} \tag{5-3}$$

Figure 5-1 shows an example domain of analysis which may contain regions of different materials (Ω_1 and Ω_2) as shown. Γ_{12} is the interface surface between the two sub-domains Ω_1 and Ω_2 as shown in Fig. 2. At the interface, the tangential component of the magnetic field and the normal component of the flux density are continuous.

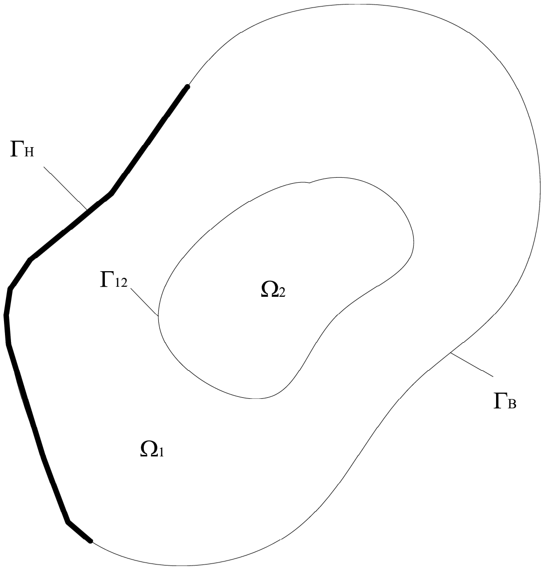

Figure 5-1. Analysis domain and boundaries

The weak form for these governing equations and boundary conditions, obtained using the weighted residual method, is

$$\int_{\Omega} (\nabla \times \delta\mathbf{A}) \cdot (\nu \nabla \times \mathbf{A}) d\Omega = \int_{\Gamma_H + \Gamma_B} \delta\mathbf{A} (\mathbf{H} \times \mathbf{n}) d\partial\Gamma + \int_{\Omega} \mathbf{J} \delta\mathbf{A} d\Omega \tag{5-3}$$

where, $\delta\mathbf{A}$ is the vector weighting function. This weak form is used in the traditional FEM to compute the element matrices by integrating the left hand side over the volume of each element. When a structured mesh is used for the analysis, the boundaries pass through the elements so that it is necessary to integrate over partial volume of the element that is inside the boundary. Several techniques [41]-[42] have been developed for integrating over partial elements approximated as polygons. Alternatively, tetrahedral elements could be generated within these partial elements for integration purpose. Even though, this is like mesh generation within the boundary elements, the generated tetrahedrons are used only for Gaussian quadrature and not to represent the solution. The boundary is approximated during these integration techniques by triangles but this approximation is independent of the structured mesh that is used for interpolating or approximating the field variables. So the geometry can be represented reasonable accurately even if a sparse mesh is used for the analysis.

Solution Structure for 3D Magnetostatics

For three dimensional magnetostatics, a solution structure for the magnetic vector potential $\mathbf{A}(\mathbf{x})$ could be defined as

$$\mathbf{A}(\mathbf{x}) = \left[\mathbf{D}(\mathbf{x})\right]\mathbf{A}^g(\mathbf{x}) + \mathbf{A}^a(\mathbf{x}) = \mathbf{A}^s(\mathbf{x}) + \mathbf{A}^a(\mathbf{x}) \tag{5-4}$$

where, $\mathbf{D}(\mathbf{x})$ is diagonal matrix whose components are defined such that $\mathrm{D}_{ii}(\mathbf{x}) = 0$ at the boundaries where essential boundary conditions are applied on the *i*th component of $\mathbf{A}$. Substituting the solution structure (Equation 5-4) into the weak form (Equation 5-3), a modified weak form of the 3D magnetostatic equation can be derived as

$$\int_\Omega \left(\nabla\times\delta\mathbf{A}^s\right)\cdot\left(\nu\nabla\times\mathbf{A}^s\right)d\Omega = \int_\Omega \mathbf{J}\delta\mathbf{A}^s d\Omega - \int_\Omega \left(\nabla\times\delta\mathbf{A}^s\right)\cdot\left(\nu\nabla\times\mathbf{A}^a\right)d\Omega \tag{5-5}$$

where, $\delta\mathbf{A}^s$ is the virtual magnetic potential vector. The grid variable vector, $\mathbf{A}^g$, is interpolated within each element as $\mathbf{A}^g = \left[\mathbf{N}\right]^T\left\{\mathbf{A}^g\right\}$ where, $\left[\mathbf{N}\right]^T$ is a matrix containing the shape functions and $\left\{\mathbf{A}^g\right\}$ is a column matrix containing the nodal values of the grid variable vector. For brick elements with 8 nodes, the size of $\left\{\mathbf{A}^g\right\}$ is 24 because the nodal degree of freedom is 3. Similarly, the boundary value function, $\mathbf{A}^a$, is defined by interpolating nodal values within each element as $\mathbf{A}^a = \left[\mathbf{N}\right]^T\left\{\mathbf{A}^a\right\}$ where, $\left\{\mathbf{A}^a\right\}$ is column matrix containing the nodal values of $\mathbf{A}^a$. These nodal values are assigned such that, at the boundaries, this function will have a values prescribed by the boundary condition. Using the solution structure, the magnetic flux for the boundary value function can be derived as

$$\nabla \times \mathbf{A}^a = \left[\mathbf{B}^C\right]\left\{\mathbf{A}^a\right\} \tag{5-6}$$

where, the 'curl' matrix $\left[\mathbf{B}^C\right]$ for the boundary value function is defined as

$\left[\mathbf{B}^C\right] = \left[\left[\mathbf{B}_1{}^C\right] \ \left[\mathbf{B}_2{}^C\right] \ \ldots \ \left[\mathbf{B}_n{}^C\right]\right]$, where,

$$\left[\mathbf{B}_i{}^C\right] = \begin{bmatrix} 0 & -\dfrac{\partial N_i}{\partial z} & \dfrac{\partial N_i}{\partial y} \\ \dfrac{\partial N_i}{\partial z} & 0 & -\dfrac{\partial N_i}{\partial x} \\ -\dfrac{\partial N_i}{\partial y} & \dfrac{\partial N_i}{\partial x} & 0 \end{bmatrix} \tag{5-7}$$

for $i \in Z = \left[1, N\right]$. The curl of $\mathbf{A}^s$ can be computed as

$$\nabla \times \mathbf{A}^s = [\bar{\mathbf{B}}^C]\left\{\mathbf{A}^g\right\} \tag{5-8}$$

For convenience, $\left[\bar{\mathbf{B}}^C\right]$ is defined as a sum of two matrices such that the first one only contains derivatives of the shape function and the second matrix contains the derivatives of the D-function. $\left[\bar{\mathbf{B}}^C\right] = \left[\bar{\mathbf{B}}_1{}^C\right] + \left[\bar{\mathbf{B}}_2{}^C\right]$, where

$$\begin{aligned} \left[\bar{\mathbf{B}}_1{}^C\right] &= \left[\left[\bar{\mathbf{B}}_{11}{}^C\right] \ \left[\bar{\mathbf{B}}_{12}{}^C\right] \ \ldots \ \left[\bar{\mathbf{B}}_{1n}{}^C\right]\right] \\ \left[\bar{\mathbf{B}}_2{}^C\right] &= \left[\left[\bar{\mathbf{B}}_{21}{}^C\right] \ \left[\bar{\mathbf{B}}_{22}{}^C\right] \ \ldots \ \left[\bar{\mathbf{B}}_{2n}{}^C\right]\right] \end{aligned} \tag{5-9}$$

$$\left[\bar{\mathbf{B}}_{1i}{}^C\right] = \begin{bmatrix} 0 & -D_{22}\dfrac{\partial N_i}{\partial x_3} & D_{33}\dfrac{\partial N_i}{\partial x_2} \\ D_{11}\dfrac{\partial N_i}{\partial x_3} & 0 & -D_{33}\dfrac{\partial N_i}{\partial x_1} \\ -D_{11}\dfrac{\partial N_i}{\partial x_2} & D_{22}\dfrac{\partial N_i}{\partial x_1} & 0 \end{bmatrix} \tag{5-10}$$

$$\left[\bar{\mathbf{B}}_{2i}{}^{C}\right]=\begin{bmatrix} 0 & -N_i\dfrac{\partial D_{22}}{\partial x_3} & N_i\dfrac{\partial D_{33}}{\partial x_2} \\ N_i\dfrac{\partial D_{11}}{\partial x_3} & 0 & -N_i\dfrac{\partial D_{33}}{\partial x_1} \\ -N_i\dfrac{\partial D_{11}}{\partial x_2} & N_i\dfrac{\partial D_{22}}{\partial x_1} & 0 \end{bmatrix} \tag{5-11}$$

In the preceding equations, $i=1,2...n$, where, *n* is the number of nodes per element.

The element matrix that is assembled into the global equations can be defined as

$$\left[\mathbf{K}^e\right]=\int_{\Omega_e}\left\{\left[\bar{\mathbf{B}}^C\right]^T\nu\left[\bar{\mathbf{B}}^C\right]\right\}d\Omega_e=\left[\mathbf{K}_1^e\right]+\left[\mathbf{K}_2^e\right]+\left[\mathbf{K}_3^e\right] \tag{5-12}$$

$$\left[\mathbf{K}_1^e\right]=\int_{\Omega_e}\left\{\left[\bar{\mathbf{B}}_1{}^C\right]^T\nu\left[\bar{\mathbf{B}}_1{}^C\right]\right\}d\Omega_e \tag{5-13}$$

$$\left[\mathbf{K}_2^e\right]=\int_{\Omega_e}\left\{\left[\bar{\mathbf{B}}_2{}^C\right]^T\nu\left[\bar{\mathbf{B}}_2{}^C\right]\right\}d\Omega_e \tag{5-14}$$

$$\left[\mathbf{K}_3^e\right]=\int_{\Omega_e}\left(\left\{\left[\bar{\mathbf{B}}_1{}^C\right]^T\nu\left[\bar{\mathbf{B}}_2{}^C\right]\right\}+\left\{\left[\bar{\mathbf{B}}_2{}^C\right]^T\nu\left[\bar{\mathbf{B}}_1{}^C\right]\right\}\right)d\Omega_e \tag{5-15}$$

Since $\left[\bar{\mathbf{B}}_2{}^C\right]$ contains the derivates of $\mathrm{D}_{ii}(\mathbf{x})$, it is non-zero only within the narrow transition band near the boundary. Therefore, for all internal elements and boundary elements without essential boundary conditions $\left[\mathbf{K}_2^e\right]$ and $\left[\mathbf{K}_3^e\right]$ are zero. Within the transition band, the derivatives of $\mathrm{D}(\mathbf{x})$ can have large magnitude. For the boundary elements with boundary conditions, the volume integral for computing $\left[\mathbf{K}_2^e\right]$ and $\left[\mathbf{K}_3^e\right]$ must be converted to surface integrals as follows to compute them accurately.

$$\left[\mathbf{K}_2^e\right]==\int_{\Gamma_e}\left\{\int_0^{\delta}\left(\left[\bar{\mathbf{B}}_2{}^C\right]^T\nu\left[\bar{\mathbf{B}}_2{}^C\right]\right)\frac{1}{|\nabla\phi|}d\phi\right\}d\Gamma_e \tag{5-16}$$

$$\left[\mathbf{K}_3^e\right]==\int_{\Gamma_e}\left\{\int_0^{\delta}\left(\left[\bar{\mathbf{B}}_1{}^C\right]^T\nu\left[\bar{\mathbf{B}}_2{}^C\right]+\left[\bar{\mathbf{B}}_2{}^C\right]^T\nu\left[\bar{\mathbf{B}}_1{}^C\right]\right)\frac{1}{|\nabla\phi|}d\phi\right\}d\Gamma_e \tag{5-17}$$

To derive the preceding equations, we make use of the fact that $\left[\bar{\mathbf{B}}_2{}^C\right]$ is zero except in the narrow band $0\le\phi\le\delta$. Therefore, the volume integral is converted into a surface integral along the boundary Γ_e and an integral over the transition band (normal to the surface). Note that if ϕ is a signed distance function then $|\nabla\phi| = 1$. If the width of the band δ is very small, then one can assume that the shape functions are constant within the band, allowing the integral over ϕ to be determined analytically. Alternatively, the integration over ϕ can also be evaluated numerically.

Current Density Computation

In three-dimensional space, magnetic force computation and multi-material analysis has the same approach as in two dimensional problems. Just as the magnetic vector potential becomes a vector for 3D problems, the current density also becomes a vector. The current density is a spatial function or a vector field for 3D magnetostatic problems so that the current density distribution should be computed prior to 3D magnetostatic analysis. Assuming that 3D problems are static, it is possible to compute electric and magnetic fields separately. In the first step, the currents in the conductor are computed. The computed values are introduced as sources for the 3D magnetostatics in the second step. Figure 5-2 shows governing equations for electrostatics and magnetostatics and the current density as sources. *V* is the electrical potential and σ is the electrical conductivity. The current density is defined as $\mathbf{J} = -\sigma\nabla V$. As the governing equation for electrostatics is one of Laplace's equations, the solution structure and finite element implementation for 3D electrostatics is identical to ones in the previous 2D magnetostatics.

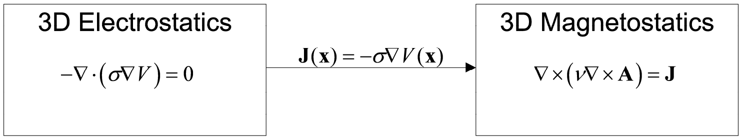

Figure 5-2. Sequential analysis for 3D Magnetostatics.

CHAPTER 6
OPEN BOUNDARY TECHIQUES FOR IBFEM

Overview of Open Boundary Techniques for IBFEM

Researchers have developed several tools for the computation of the solution fields for open boundary problems, which are boundary value problems that need infinite solution domain. Since electromagnetic field problems are the infinite domain problems, several tools, called open boundary techniques, are developed for the magnetostatic analysis. The techniques includes truncation of outer boundaries, ballooning, infinite elements, infinitesimal scaling, spatial transformations, boundary relaxation approach, database approach, hybrid approaches, asymptotic boundary conditions (ABC), and measured equation of invariance (MEI) and so on [40]. Each open boundary technique has both merits and demerits as shown in Table 6-1 [40]. Unfortunately, no all-purpose powerful technique exists, so a researcher should choose one of these according to their application.

Table 6-1. Comparison of different open boundary techniques [40]

Methods	Advantages	Disadvantages
Truncation	Simple	Large number of unknowns
Iteration	Simple	Remeshing
Relaxation	Simple	More than 1 solutions
Ballooning	Accurate/sparse	Only 2D Laplace equation
Infinite elements	Sparse	Exterior inaccurate
Infinitesimal scaling	Accurate	Nonlinear equation and dense matrix
Spatial transformation	Sparse	No current source
Hybrid method	Accurate	Dense matrix
1st-order ABC	Sparse/efficient	Circular/spherical boundaries
MEI	Sparse	Selection of metrons

Among open boundary techniques for FEM, only some techniques are suitable for use with IBFEM. Some techniques are not suitable for IBFEM because those techniques require the conformal meshing or have other limitations. The unsuitable techniques include the ballooning method, the infinitesimal scaling approach, and the database approach. One of the most simple and efficient methods is the ballooning method [43]-[46]. The method needs a special meshing technique as shown in Figure 6-1. An outer boundary of a discretized region called annulus is moved outward from a center recursively. All nodes lie on the radial lines extending from a center point *o*. Using a fixed ratio *r* called the mapping ratio, new annulus can be added in the radial direction.

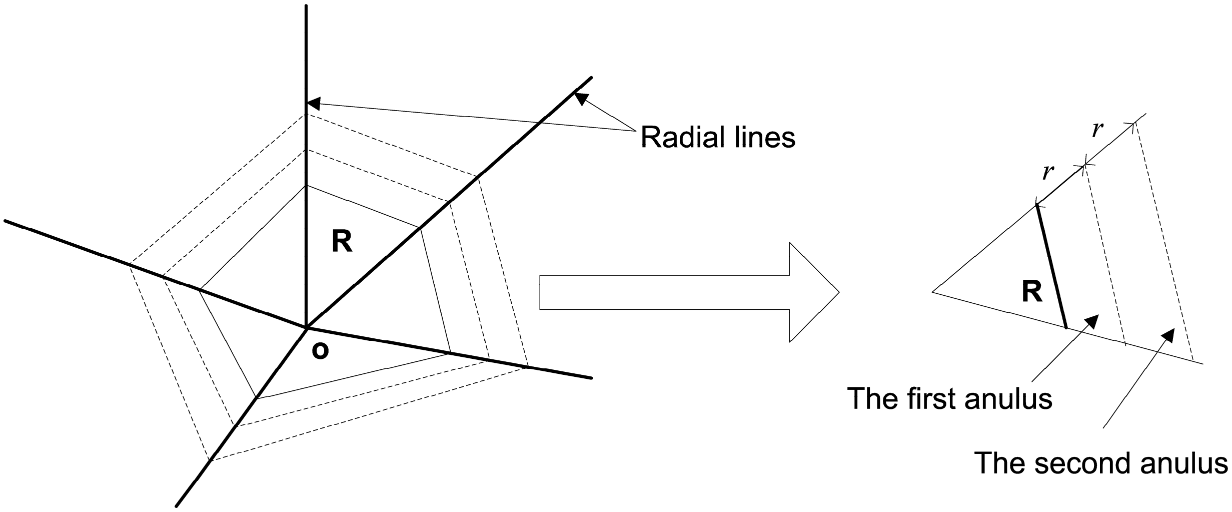

Figure 6-1. Two-dimensional interior region with an exterior annulus

Based on the mesh, the method can create fast and accurate results. However, there are disadvantages such as having to select the center point and the mapping ratio for well-established mesh. Additionally, the method is only applicable to 2D Laplace's equations. The special meshing technique is not suitable for IBFEM so that it can not adopt this ballooning method. Secondly, the infinitesimal scaling approach [40] also requires such an annulus between interior and exterior region making it unsuitable for IBFEM. Thirdly, the database approach, developed by Sun et al [47] and Chen et al [48], requires preprocessing to assemble and eliminate matrices of the exterior region. The information is saved in a database so that it is used during the solving procedure.

In this research, IBFEM is extended to use the following techniques: the truncation approach, the asymptotic boundary condition, and the infinite element. The approach involves the truncation of outer boundaries is to impose homogeneous essential boundary conditions at the far away boundaries. The technique assumes that the distance of the outer boundary from the center is at least five times the size of the region of interest. The method is easy to be implemented, but it is computationally expensive due to the large analysis domain. Therefore, there is no effort to adopt this method for IBFEM. Unlike the truncation approach, the other two techniques have implementation issues that are described in the following sections.

Asymptotic Boundary Conditions for IBFEM

Considering computational efficiency, the asymptotic boundary condition is one of the most attractive approaches because the method guarantees matrix sparsity [40]. It is very similar to absorbing boundary conditions in high frequency calculations. In static and quasi-static electromagnetic fields, the asymptotic boundary condition is used. Many researchers had solved open boundary problems using this technique. Brauer et al. [49] introduced the magnetic vector potential based problems using vector asymptotic boundary conditions. As the asymptotic boundary conditions are derived using the spherical coordinate system, circular or spherical boundaries are needed for the vector asymptotic boundary conditions. In order avoid the inconvenience of having circular boundaries, Chen, Konrad, and Baronijan [50] developed techniques to solve axisymmetric electrostatic problems with rectangular boundaries. Chen, Konard, and Biringer [51] introduced the vector asymptotic boundary conditions for three dimentional magnetostatic problems with box boundaries. Gratkowski et al. [52] solved the axisymmetric magnetostatic problems with arbitrary boundaries.

Derivation of Asymptotic Boundary Conditions

The magnetic vector potential is defined as follow

$$\mathbf{B} = \nabla \times \mathbf{A} \tag{6-1}$$

Using Equation (6-1), the Ampere's law can be restated as

$$\nabla \times \frac{1}{\mu}\mathbf{B} = \nabla \times \frac{1}{\mu}\left(\nabla \times \mathbf{A}\right) = \nabla\left(\nabla \cdot \mathbf{A}\right) - \nabla^2 \mathbf{A} = -\nabla^2 \mathbf{A} = \mathbf{J} \tag{6-2}$$

where, $\nabla \cdot \mathbf{A} = 0$ that is the Coulomb gauge condition. When **A=0** at infinity, the general solution of the Poisson's equation is

$$\mathbf{A}(\mathbf{r}) = \frac{\mu}{4\pi}\int \frac{\mathbf{J}(\mathbf{r}')}{\left|\mathbf{r} - \mathbf{r}'\right|} d\mathbf{v}' \tag{6-3}$$

where, $\mathbf{J}(\mathbf{r}')$ is current density at position $\mathbf{r}'$ and $\left|\mathbf{r} - \mathbf{r}'\right|$ is distance from the current source. When $\mathbf{r}$ is much larger than $\mathbf{r}'$, the solution asymptotically becomes

$$\mathbf{A}(\mathbf{r}) \approx \frac{\mu_0}{4\pi r}\int \mathbf{J}(\mathbf{r}') d\mathbf{v}' + \frac{\mu_0}{4\pi r^2}\int \mathbf{J}(\vec{\mathbf{r}})\vec{\mathbf{r}} \cdot \vec{\mathbf{r}} d\mathbf{v}' \tag{6-4}$$

where, $\vec{\mathbf{r}}$ is the unit radial direction vector. When $\mathbf{r} >> \mathbf{r}'$, $\int \mathbf{J}(\mathbf{r}') d\mathbf{v}' \approx 0$. Therefore, the magnetic vector potential approximately becomes

$$\mathbf{A}(\mathbf{r}) \approx \frac{\mu_0}{4\pi r^2}\int \mathbf{J}(\vec{\mathbf{r}})\vec{\mathbf{r}} \cdot \vec{\mathbf{r}} d\mathbf{v}' \approx \frac{1}{r^2}\vec{\mathbf{a}}(\theta, \phi) \tag{6-5}$$

where, $\vec{\mathbf{a}}(\theta, \phi)$ is a function in the spherical coordinate system. The leads to following equation:

$$\frac{\partial \mathbf{A}}{\partial r} + \frac{2}{r}\mathbf{A} = 0 \tag{6-6}$$

which is called the first-order asymptotic boundary condition (ABC).

Two Dimensional Asymptotic Boundary Conditions

The asymptotic boundary conditions were originally based on circular or spherical boundaries. In two dimensional domain, Gartkowski et al. developed this method for arbitrary outer boundaries [52]. Cartesian coordinates and rectangular outer boundaries are used so that IBFEM can be easy to adopt this approach. For 2D Magnetostatic problems, the magnetic potential vector exists only on the z component. On the rectangular boundaries for IBFEM, the line segment 1-2 with the unit normal of (1,0,0) is shown in Figure 6-2.

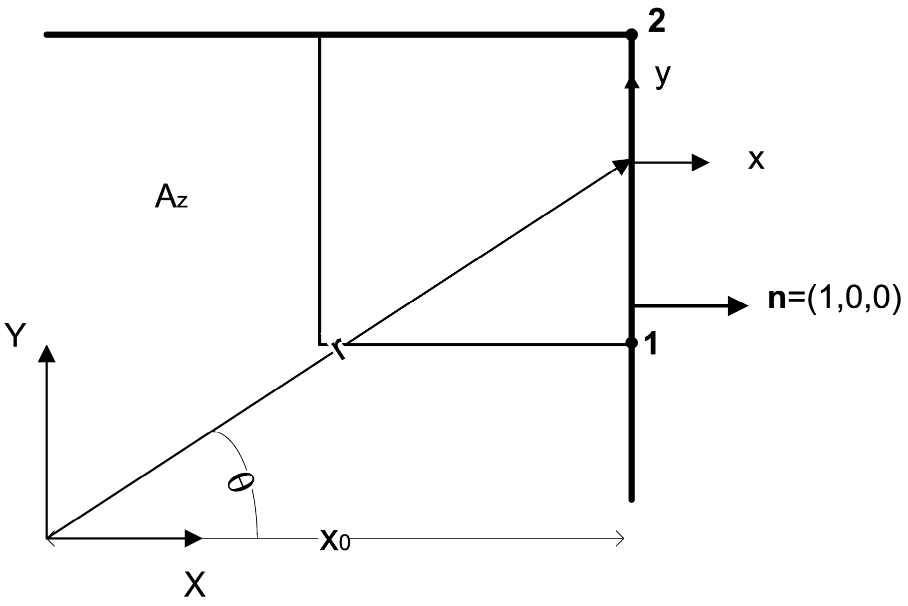

Figure 6-2. Structured grid and rectangular boundary

The derivative of A in the radial direction on the line segment becomes

$$\frac{\partial A_z}{\partial r}=\frac{\partial A_z}{\partial x}\frac{\partial x}{\partial r}+\frac{\partial A_z}{\partial y}\frac{\partial y}{\partial r}=\frac{\partial A_z}{\partial x}\cos\theta+\frac{\partial A_z}{\partial y}\sin\theta \tag{6-7}$$

Substituting Equation 6-7 into Equation 6-6, the equation becomes

$$\frac{\partial A_z}{\partial x}\frac{x_0}{r}+\frac{\partial A_z}{\partial y}\frac{y}{r}+\frac{2}{r}A_z=0 \tag{6-8}$$

Since $\cos\theta = \frac{x_0}{r}$ and $\sin\theta = \frac{y}{r}$. Therefore, ABC on a line segment 1-2 in Figure 6-2 can be written as

$$\frac{\partial A_z}{\partial x} = -\frac{2}{x_0}A_z - \frac{y}{x_0}\frac{\partial A_z}{\partial y} \tag{6-9}$$

which means the derivative of the magnetic vector potential in the normal direction can be decomposed of two terms: the derivative of the magnetic vector potential in the tangential direction and the magnetic vector potential.

According to Gratkowski et al [52], the coefficients of the boundary matrix can be calculated from

$$K_{ij} = \frac{\nu}{x_0}\int_{\Gamma_e}\left(2N_iN_j + y\left(N_i\frac{\partial N_j}{\partial y} + N_j\frac{\partial N_i}{\partial y}\right)\right)d\Gamma_e \tag{6-10}$$

Similarly, the line segments with the unit normal of (0,1,0) can have the following ABC

$$\frac{\partial A_z}{\partial y} = -\frac{2}{y_0}A_z - \frac{x}{y_0}\frac{\partial A_z}{\partial x} \tag{6-11}$$

The coefficients of the boundary matrix become

$$K_{ij} = \frac{\nu}{y_0}\int_{\Gamma_e}\left(2N_iN_j + x\left(N_i\frac{\partial N_j}{\partial x} + N_j\frac{\partial N_i}{\partial x}\right)\right)d\Gamma_e \tag{6-12}$$

Infinite Elements for IBFEM

Since Ungless and Bettess [53] first proposed the infinite element technique, many researchers have developed the technique with two approaches: decay interpolation function approach (or displacement descent formulation) and mapped finite element approach (or coordinate ascent formulation). Bettess [54]-[56] developed the decay interpolation function approach for potential and elasticity problems. The method was extended to solve the Helmholtz equations by Rahman and Davies [56], McDougall and

Webb [58] and Towers, McCowen, and Macnab [59]. This approach uses the finite element shape functions multiplied by a decay function such as the reciprocal decay function [53] or the exponential decay function [55]. The modified shape functions make a field variable decrease to the specified far field value. Within the element, the numerical volume integration is done using Guass-Lagueree quadrature instead of Gauss-Legendre quadrature used in the finite element method because the integration range is different.

The mapped finite element approach was initially developed by Beer and Meek[60], and Zienkiewicz et al [61]. Abdel-Fattah et al [62] generalized the method for static analysis in one-, two- and three- dimensional infinite domain. The approach transforms a regular finite domain into an infinite domain using the mapping of the shape function and the numerical integration of Gauss-Legendre quadrature. Using this approach, open boundary electromagnetic field problems were solved by Rahman and Davies [56], McDougall and Webb [58] and Gratkowski and Ziolkowski [63].

These two approaches for infinite element implementation have similar performance. For IBFEM, the first approach was implemented. When a structured mesh is used, the shapes of the infinite elements are known so that the infinite elements can be treated as virtual elements. Based on the assumption, the decay function infinite element approach can be easily implemented without creating extra structured elements on the infinite domain.

Decay Interpolation Function Approach

The mapping functions used for infinite elements are the same as shape function. They are denoted as M_i, $i = 1 \text{ to } n$, where n is the total number of nodes in the element.

When the element is an isoparametric element, the shape functions for the infinite element are multiplied by the decay functions as follows

$$N_i(s,t) = f_i(s,t)M_i(s,t) \tag{6-17}$$

where, $N_i(s,t)$ are the shape functions on the infinite domain and $f_i(s,t)$ are decay functions. Figure 6-3 shows coordinate transformation for the decay function infinite element. When the decay direction is the radial direction *r* in the global coordinate system, the infinite element can be transferred from the global coordinate system to the parametric coordinate system as shown in Figure 6-3. In the parametric coordinate system, the decay direction becomes the positive *s* direction and $s \in [-1, \infty)$. When an element matrix, **K**, is obtained taking a volume integral of the element, Gauss-Laquerre integration is used instead of Gauss-Lagendre scheme that is used for the traditional finite element method because the integration is done from -1 to the infinity in the parametric space.

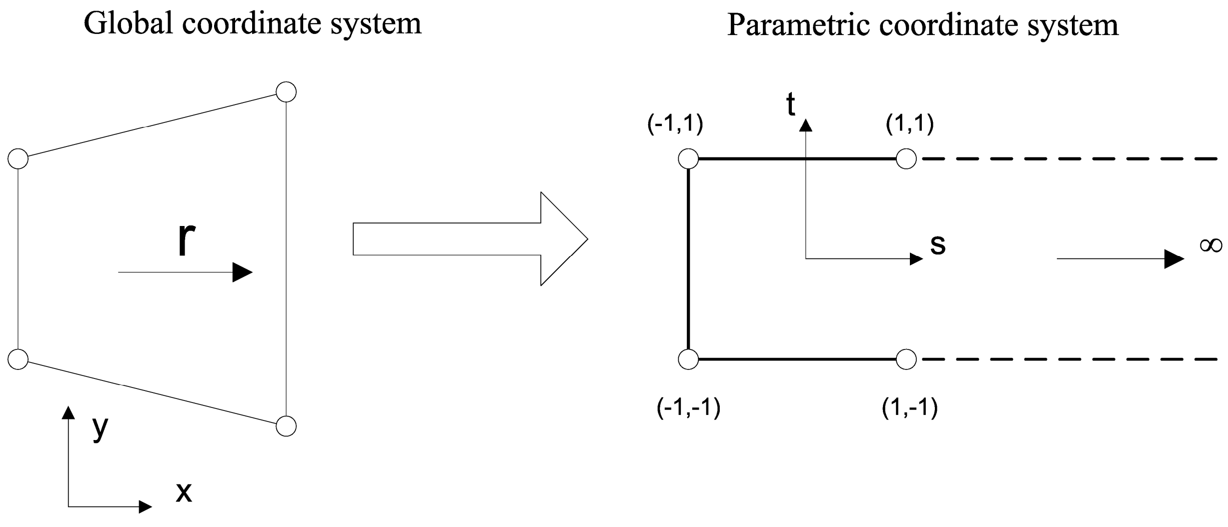

Figure 6-3. Coordinate transformation for the decay function infinite element

The decay function should be unity at its own node, (s_i, t_i), however do not have to be zero at the other nodes. Under these assumptions, the decay function can be one of several decay patterns such as reciprocal decay type, exponential decay type, sinusoidal decay type, and so on. The selection of the decay function is contingent on the type of the problems being solved. For magnetostatics, an exponential decay pattern is suitable.

Assuming that the decay direction is the positive s direction, the exponential decay function is

$$f_i(s,t) = \exp[(s_i - s)/L] \tag{6-18}$$

where, L is defined as decay parameter to determine the degree of decay. If the decay directions are the positive s and t directions, the decay function can be stated as

$$f_i(s,t) = \exp[(s_i + t_i - s - t)/L] \tag{6-19}$$

Figure 6-4 shows 1D shape functions using exponential decay functions. The shape functions using exponential decay functions are $N_1 = \exp[(-1-s)/L]\left(\frac{1-s}{2}\right)$ and $N_2 = \exp[(1-s)/L]\left(\frac{1+s}{2}\right)$. Figure 6-4 shows plots of the shape functions for different decay parameter.

If a decay pattern for the problem is known, a value of the decay parameter can be estimated. Many unbounded potential problems are governed by the reciprocal decay pattern. In this case, the decay behavior can be expressed by using the exponential decay functions with proper decay parameter. Supposing there are two functions: $\frac{A}{r}$

and $B\exp(-s/L)$ where A and B are arbitrary values, $r = r_1$ at $s = -1$, and $r = r_2$ at $s = 1$, two functions have same values at two points as follows

$$\frac{A}{r_1} = B\exp(1/L) \qquad (6\text{-}20)$$

$$\frac{A}{r_2} = B\exp(-1/L) \qquad (6\text{-}21)$$

After eliminating A and B, the decay parameter is estimated using r_1 and r_2 as follow

$$L = -2\ln\left(\frac{r_1}{r_2}\right) \quad (6\text{-}22)$$

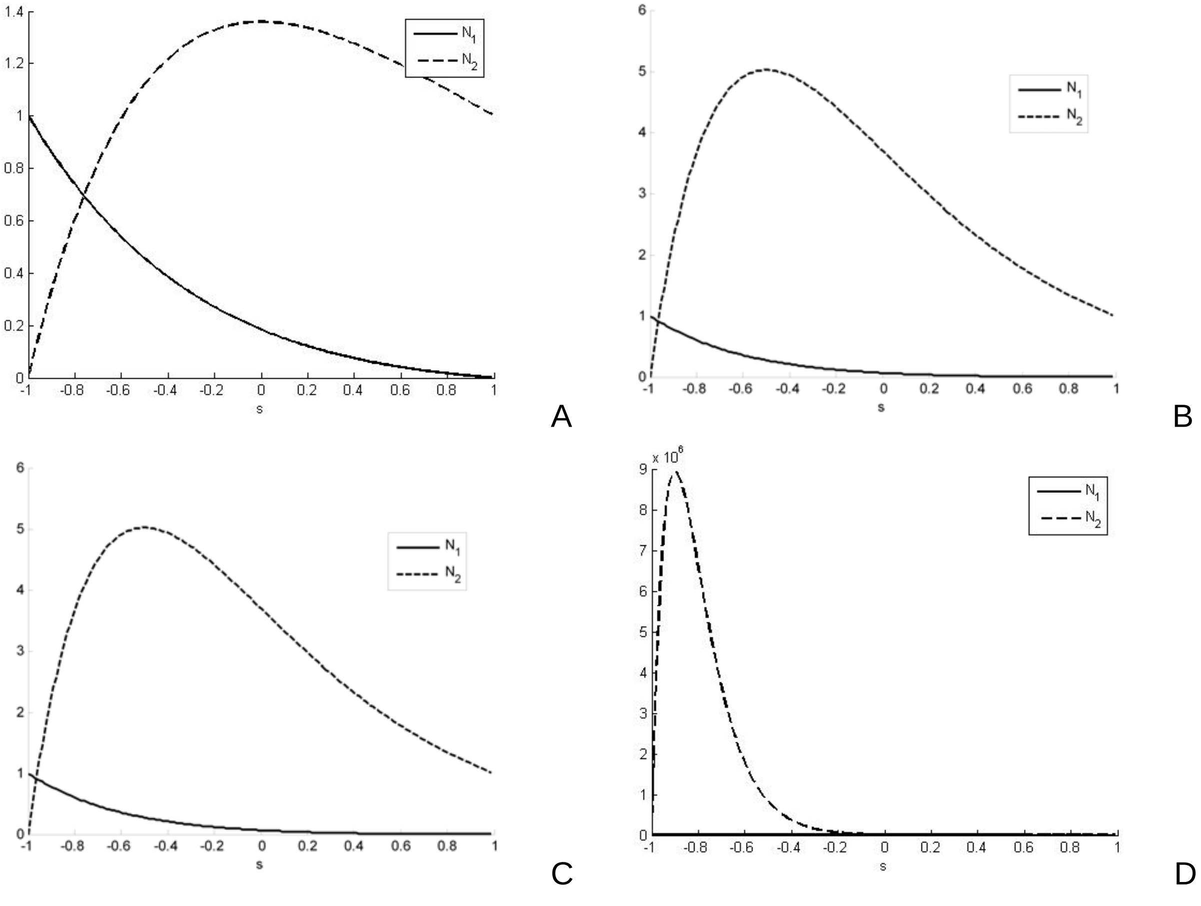

Figure 6-4. 1D shape functions using exponential decay functions. A) L=1, B) L=2, C) L=0.5, and L=0.1

Decay Function Infinite Element for IBFEM

The decay function infinite element is easy to implement for a structured mesh. As the infinite elements are rectangular, the Jacobian matrix of the infinite element is easy to compute. When the field variable is zero on far away boundaries, the grid elements for the infinite domain need not be created so that the infinite elements can be virtual elements. Figure 6-5 shows structured grids with the infinite elements.

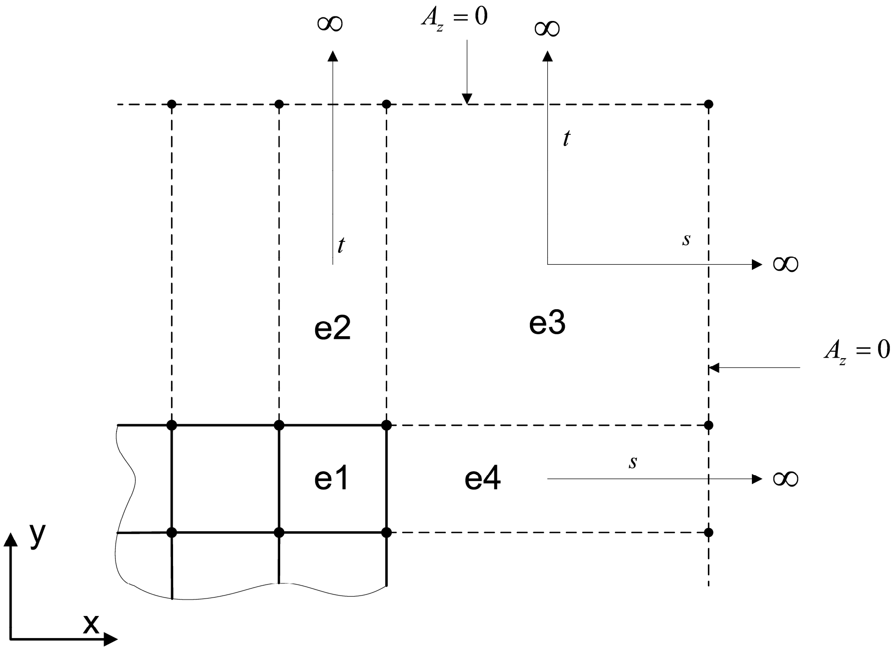

Figure 6-5. Structured grids with the infinite elements

Element e1 belongs to structured grid and the other elements e2, e3, and e4 are the infinite elements. e2 and e4 are extended to infinity in one direction. e3 is extended in infinity in two directions.

Figure 6-6 illustrates an example with three elements: two finite elements and one infinite element. The boundary conditions are the solution $P = 1$ at x=0 and $P = 0$ at infinity.

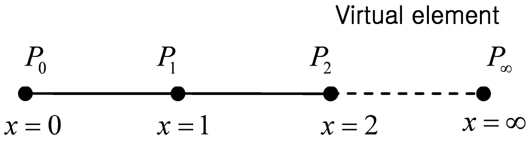

Figure 6-6. Domain of integration

The differential equation is

$$\frac{d^2P}{dx^2}=0 \tag{6-23}$$

For the infinite element, the mapping function and the shape function are defined as

$$M_1=\frac{1+s}{2} \qquad s\in[1,\infty) \tag{6-24}$$

$$N_1=\left(e^{(1-s)/L}\right)\left(\frac{1+s}{2}\right) \qquad s\in[1,\infty) \tag{6-25}$$

As $P=0$ at infinity, K_{11}, coefficient of the infinite element matrix, is stated as follow

$$K_{11}=\int_1^\infty \frac{\partial N_1}{\partial x}\frac{\partial N_1}{\partial x}\frac{dx}{ds}ds=\int_1^\infty e^{(2-2s)/L}p_{11}(s)ds \tag{6-26}$$

where, $p_{11}(s)=\left(\frac{\partial M_1}{\partial s}-\frac{1}{L}M_1\right)^2$ and $\frac{dx}{ds}=1$. Substituting $s=\frac{L}{2}s'+1$, the coefficient

becomes

$$K_{11}=\int_0^\infty e^{-s'}p_{11}(s)\frac{ds}{ds'}ds'=\int_0^\infty e^{-s'}p_{11}(s)\frac{L}{2}ds' \tag{6-27}$$

The integration is done using Guass-Laguerее integration with following modified weights and abscissas

$$W_{new}=W_{old}\frac{L}{2}e^{2/L} \tag{6-28}$$

$$s=\frac{L}{2}s'+1 \tag{6-29}$$

A solution for this example is provided by Chari and Salon [63]. Figure 6-7 shows the reference solution by Chari and Salon [63] and the computed solution varying with the decay factor *L*. It graphically represents that the solution is very sensitive to the decay factor. Thus, it is necessary to choose proper value of the decay factor according a physical phenomenon.

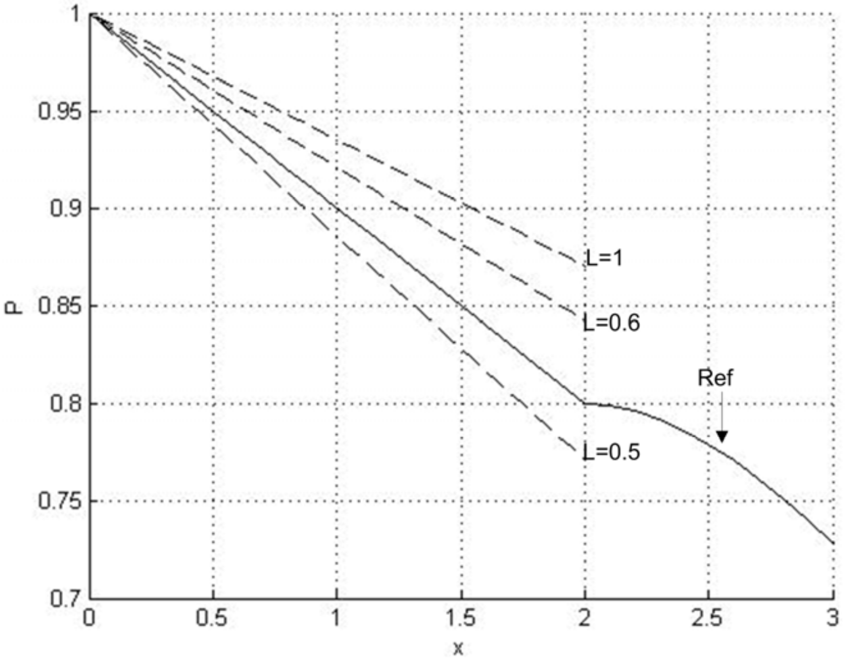

Figure 6-7. Solution plots for 1D infinite element example

CHAPTER 7
RESULTS AND DISCUSSIONS

Two Dimensional Magnetostatic Problems

IBFEM was implemented by modifying a finite element program. Four magnetostatic examples are examined to validate this method and show the benefits of IBFEM. These examples are published in [66]. The first example is a two dimensional model of a coaxial cable. The second example is a planar solenoid with a clapper armature [18]. Both problems were selected because they have analytical solutions for comparison. The third example is a planar solenoid with a damaged armature. This example illustrates that even when the geometry is changed the same grid still provides reasonable answers while with FEM a new mesh is needed that is harder to generate as the geometry gets complicated. The final example is a 2D model of a switched reluctance motor (SRM). For all these examples, the geometry was created in commercial CAD software (Pro/Engineer) and imported into the analysis software (IBFEM).

Example 7-1-1: 2D Coaxial Cable

A coaxial cable, which consists of an inner conductor, an insulator, and an outer conductor, is modeled. Due to circular symmetry of the geometry, only a quadrant of the coaxial cable cross-section is created. Figure 7-1 shows the coaxial cable model using three separate structured grids. The radii of the inner conductor, the insulator and the outer conductor are a, b and c. The inner and outer conductors carry the same amount of total current in opposite directions. The total current flowing through each conductor is I. The current flows in the axial direction (the z-direction) and the current density is assumed to be uniform.

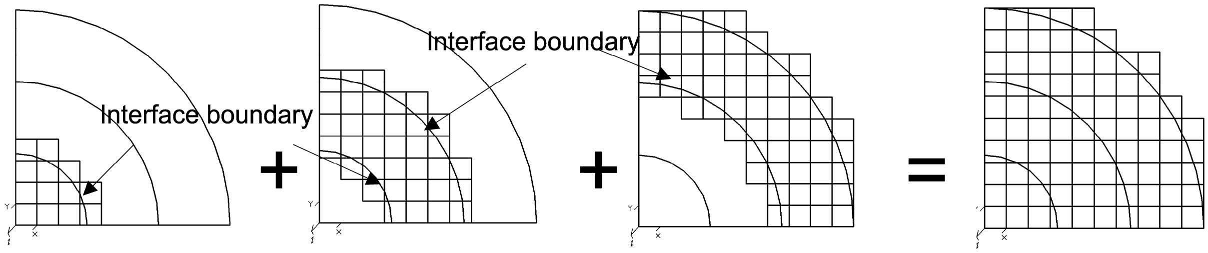

Inner conductor : Grid1 Insulator : Grid 2 Outer conductor : Grid 3 Coaxial cable : Total Grid

Figure 7-1. 2D coaxial cable model with structured grids

The analytical solution of the magnetic field in circumferential direction can be derived as

$$H_\theta = \begin{cases} r\left(2\pi a^2\right)^{-1} I & ,0 \le r < a \\ \left(2\pi r\right)^{-1} I & ,a \le r < b \\ \left(c^2 - r^2\right)\left(c^2 - b^2\right)^{-1}\left(2\pi r\right)^{-1} I & ,b \le r < c \\ 0 & ,c \le r \end{cases} \tag{7-1}$$

where, r is the radial distance. The following values of current and radii were used in the numerical model: $I = 1000A$, $a = 0.5$, $b = 1$, and $c = 1.5$ mm.

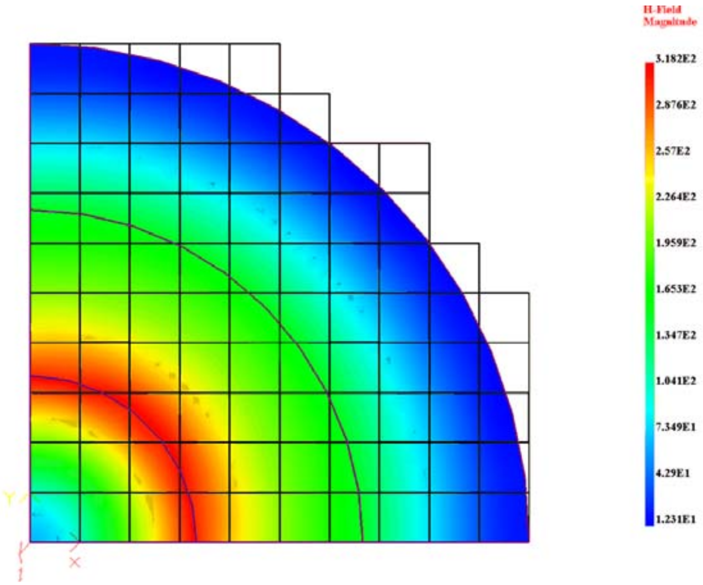

Figure 7-2. Magnitude of H field

Figure 7-2 shows the magnitude of the magnetic field that was computed using the quadratic B-spline elements. It shows that the maximum magnetic field value is at the interface between the inner conductor and the insulator and has a value of 3.182×10^2 A/mm. This is very close to the value obtained from the analytical solution which is 3.183×10^2 A/mm.

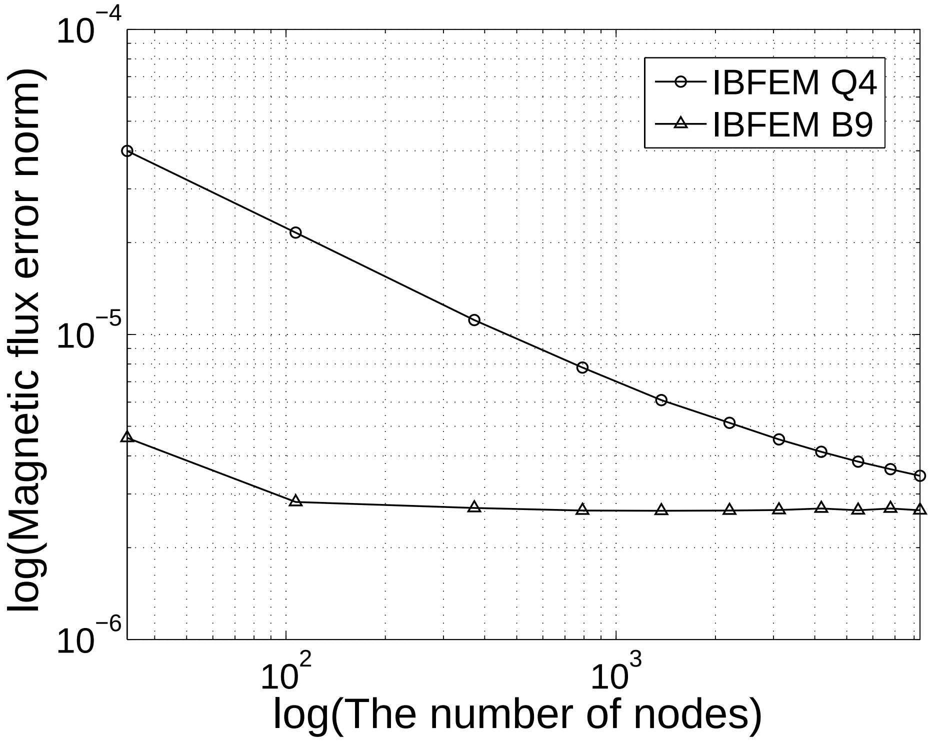

Figure 7-3. Convergence plot for H1 norm

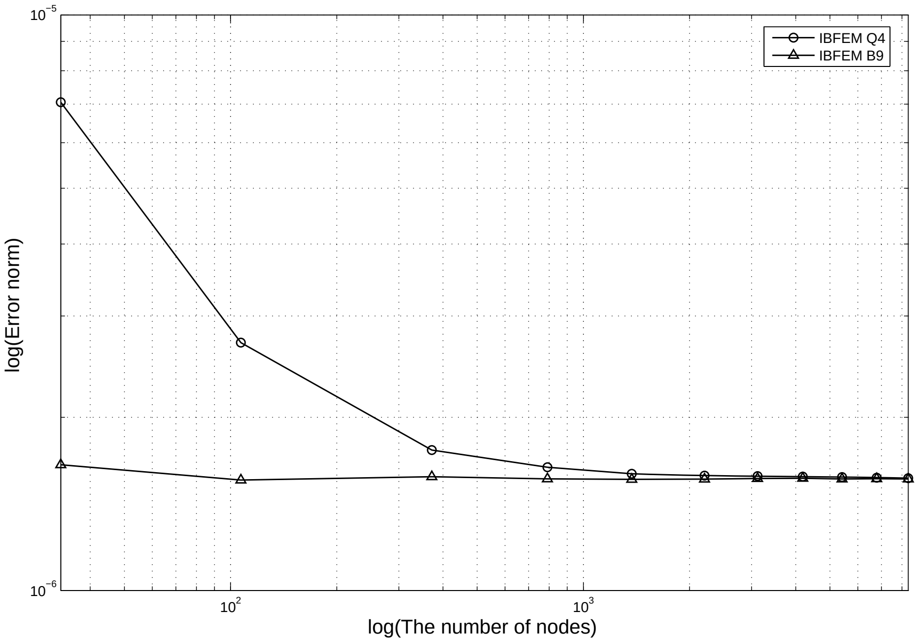

Figure 7-4. Convergence plot for L2 norm

Figure 7-3 shows the convergence of H_1 error norm which is the root mean square error in flux density field over the domain and can be defined as

$$\|H_1\| = \left(\int_{\Omega} \left(\mathbf{B}^e - \mathbf{B}^h \right)^T \cdot \left(\mathbf{B}^e - \mathbf{B}^h \right) d\Omega \right)^{\frac{1}{2}} \tag{7-2}$$

where, $\mathbf{B}^e$ is the exact value of the magnetic flux from the analytical solution and $\mathbf{B}^h$ is the corresponding computed value. Fig. 7-4 shows convergence of L_2 error norm of *A(x,y)*. This error norm is defined as

$$\|L_2\| = \left(\int_{\Omega} \left(A^e - A^h \right)^T \cdot \left(A^e - A^h \right) d\Omega \right)^{\frac{1}{2}} \tag{7-3}$$

where, A^e is the exact value of the magnetic potential from the analytical solution and A^h is the computed value. The plot shows faster convergence for B-spline elements but the rate of convergence decreases with increasing number of nodes.

Example 7-1-2: 2D Clapper Solenoid Actuator

The clapper armature solenoid is composed of an armature, a stator, and coils. A two-dimensional planar model is shown in Figure 7-5 where symmetry is used to model just half of the system. The dimensions of the components provided in [18] were used in the model to compare with the approximate solution. Relative permeability of the armature and the stator was assumed to be $\mu_r = 2000$. The stator winding has 200 turns and a current I = 2A. When current flows through the coil, an attractive force is generated between the armature and the stator, which produces linear motion similar to clapping. Figure 7-5 shows a typical grid that is used to model this problem where each part has its own grid and elements of these grids overlap only at the interfaces.

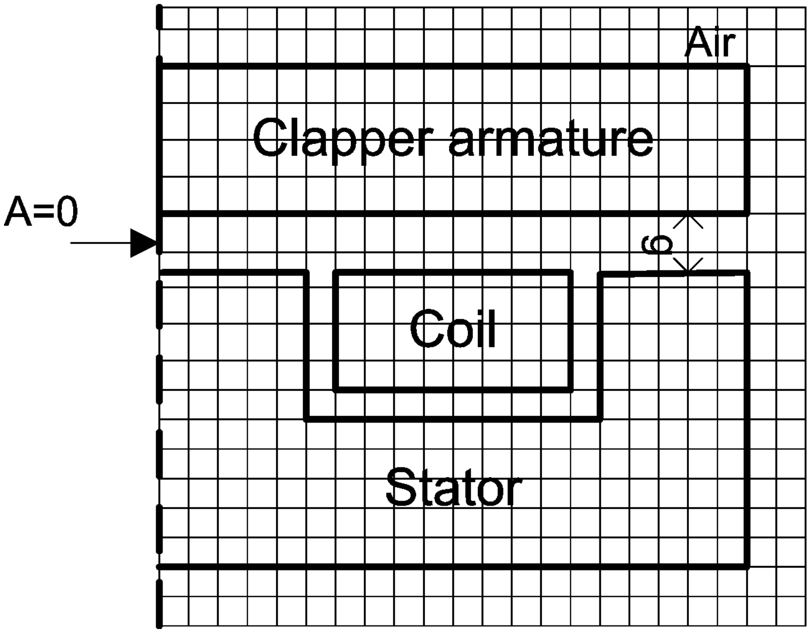

Figure 7-5. 2D Clapper solenoid with structured grid

Brauer [18] has provided an approximate solution for this problem using the reluctance method and using FEM when the gap width is 2mm. The total force obtained by the reluctance method is 122.62N and the force computed by FEM is 135.9N. For the

IBFEM model, a grid consisting of quadratic B-spline elements was used for the results shown in Figure 7-6 B. Essential boundary conditions are applied along the axis of symmetry to enforce symmetry.

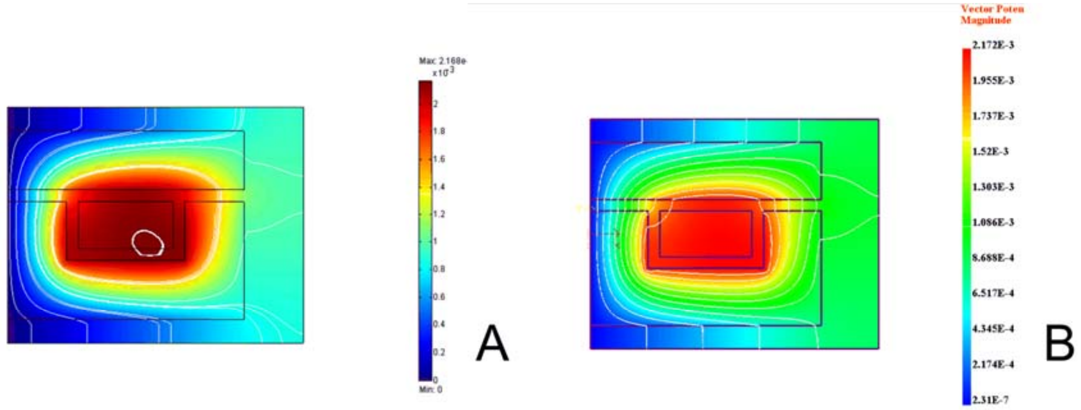

Figure 7-6. Magnetic vector potential and magnetic flux lines. A) Comsol, and B) IBFEM

Figure 7-6 shows flux lines and the plot of magnetic vector potential when the width of the air gap is 2mm. Figure 7-6 A shows the result using commercial FEA software (COMSOL). The result from IBFEM is shown in Figure 7-6 B. The patterns of flux lines are similar for both results and the values of magnetic vector potential obtained are very close. Using the magnetic field computed using IBFEM, the total force was 140.0N, which is quite close to the total forces obtained by reluctance method and FEM in [18]. Figure 7-7 shows the total force on the clapper armature as a function of the gap width. In the Figure, the computed values of total force for different gap width are compared with approximate (analytical) forces determined using reluctance method and Maxwell’s stress tensor.

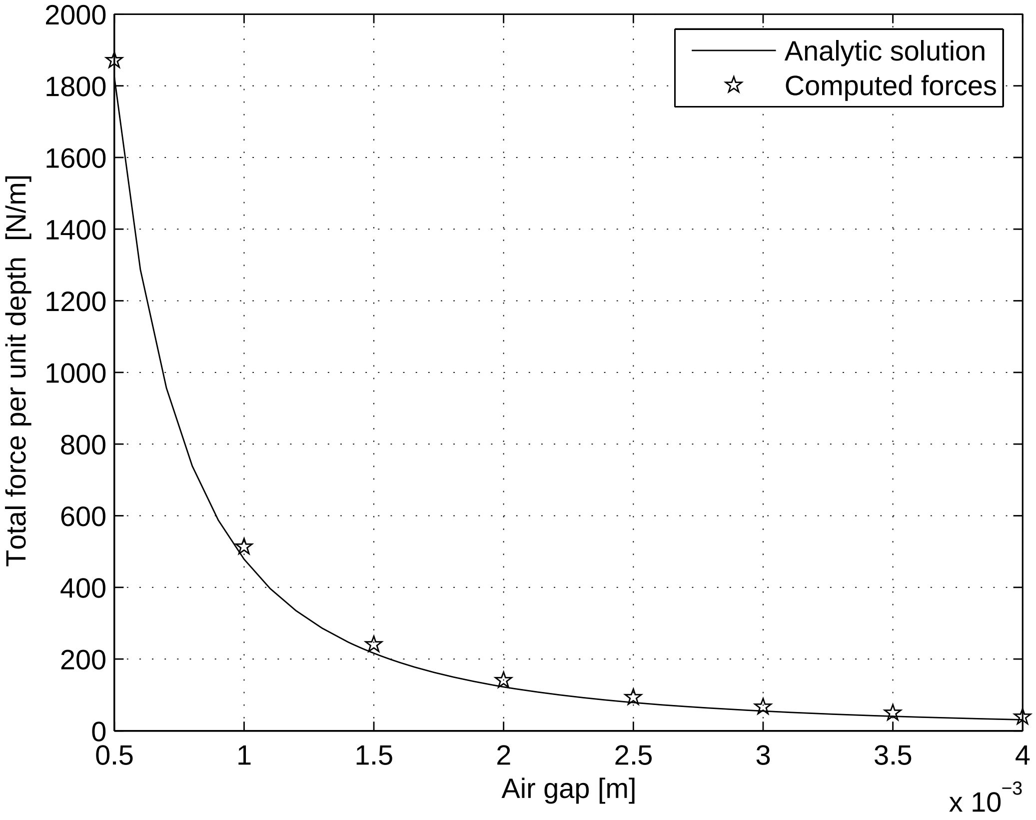

Figure 7-7. Magnetic force versus air gap length

Example 7-1-3: 2D Clapper Solenoid Actuator with Artificial Damage

The clapper armature in above example has been remodeled in this example with an artificial damage added by editing one of the edges of the 2D geometry as shown in Figure 7-8 A. As in the previous example, air gap width equal to 2mm was used to compute the results shown in Figure 7-8 B. This example was created to show that significant increase in complexity of the model geometry does not pose a problem and in fact the same grid that was used in the last example was used for this example too. The computed force on the armature with the damage was 83.56 N compared to 140N without the damage. Figure 7-8 B displays the contour and a plot of the magnetic vector potential. The computed magnetic potential varies smoothly between the two materials (iron and air) in the damaged area despite the increase in geometric complexity.

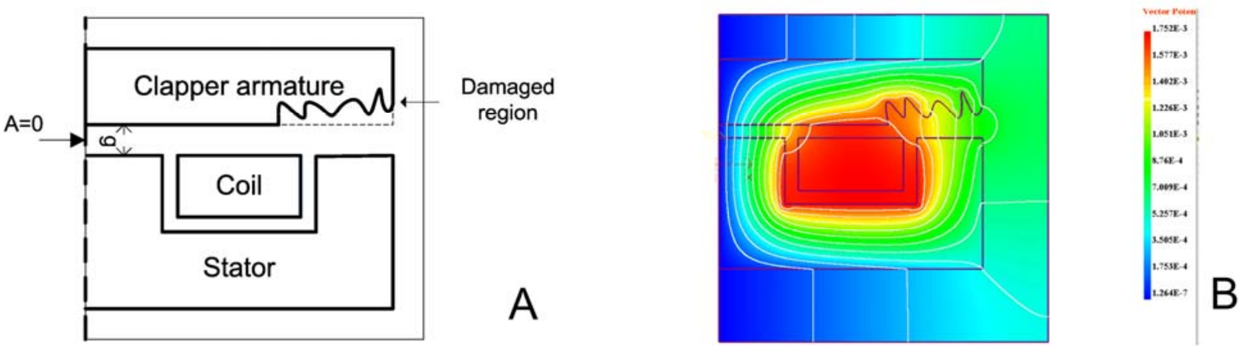

Figure 7-8. Clapper solenoid with artificial damage. A) Damaged region and boundary condition, and B) Flux lines and surface plot of A

Example 7-1-4: 2D Switched Reluctance Motor

A 2D planar model of the Switched Reluctance Motor (SRM) is shown in Figure 7-9. SRM is a DC motor where the stator has windings around the poles while the rotor does not have any windings. The motor is called 6/4 Pole SRM because the stator has 6 poles and the rotor has 4 poles.

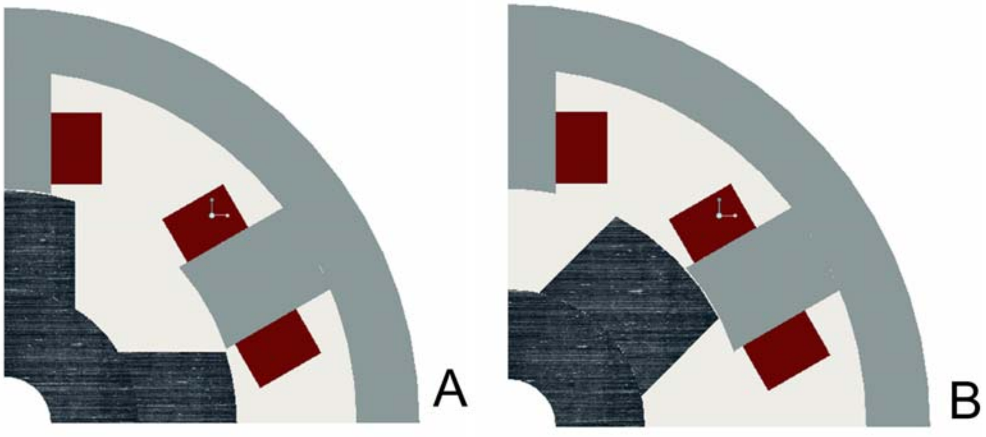

Figure 7-9. 2D Planar model of switched reluctance motor. A) Aligned position, and B) Unaligned position.

According to Arumugam et al [64], the main dimensions of the motor are:

Stator core outer diameter = 16.51 cm.

Stator bore diameter =9.3cm.

Length of iron core =10.8cm.

Stator pole arc =1.88cm.

Height of stator pole =2.355cm.

Length of air gap = 0.0255cm.

Rotor pole arc =2.83cm.

Height of rotor pole =1.95cm.

Diameter of the shaft = 1.858 cm

Number of turns per pole =222

Current is applied to the coils around the poles of the stator sequentially to produce a torque on the rotor as it rotates. The stator and the rotor are made of iron with relative permeability of 2000. A quarter of the motor is modeled in both its aligned and unaligned orientation. The number of turns in the coil is assumed to be 500 and the current is 2 A. Currents only flows into coils attached to the top pole of the stator. Essential boundary condition (A=0) is imposed on peripheries of the shaft and the stator and the vertical axis. B-spline elements are used for the analysis so that accurate results are obtained even with a sparse grid as shown in Figure 7-10 and Figure 7-11. The flux lines computed here are similar those computed by FEM [64]. Note that the air gap is very small compared to the average element size in the grid. Despite the geometric complexity and large number of parts and materials involved, this approach for analysis yields results using structured grids comparable to results from traditional FEM using conforming mesh.

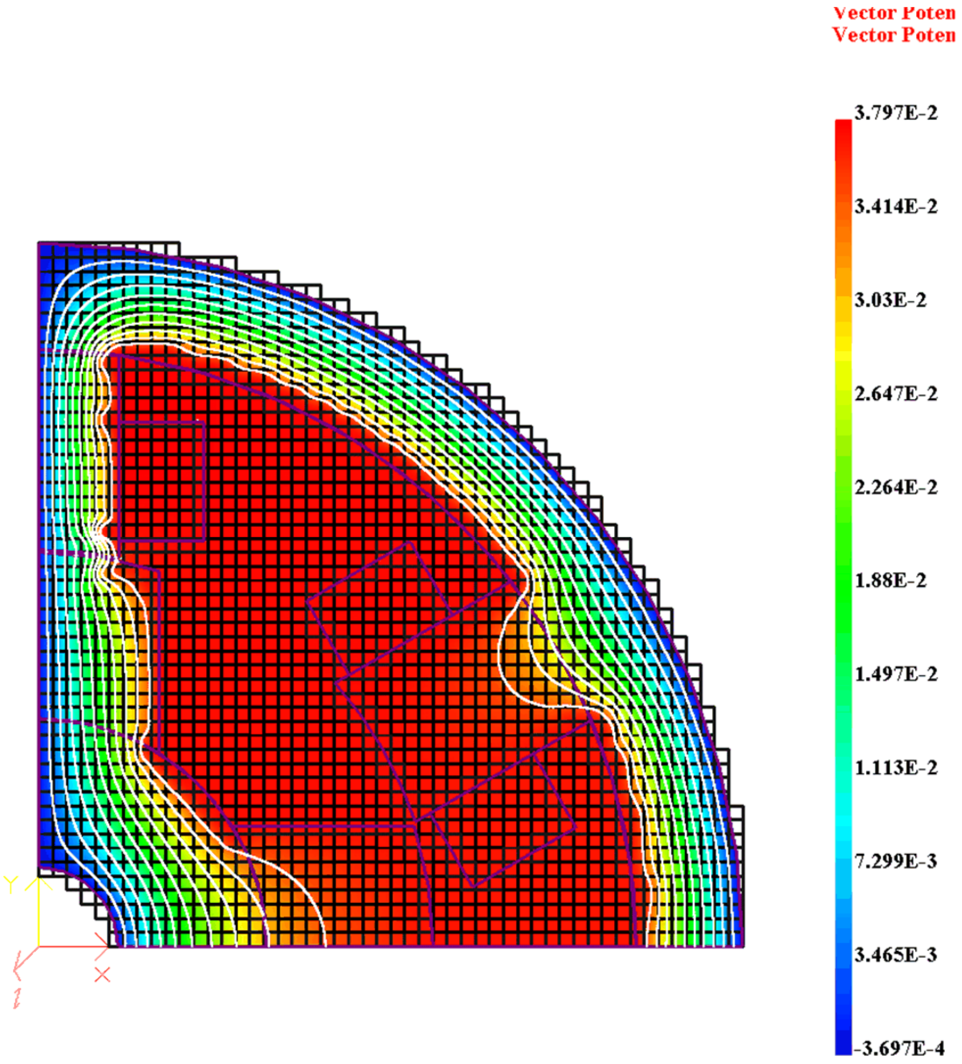

Figure 7-10. Magnetic vector potential and magnetic flux lines in the aligned position

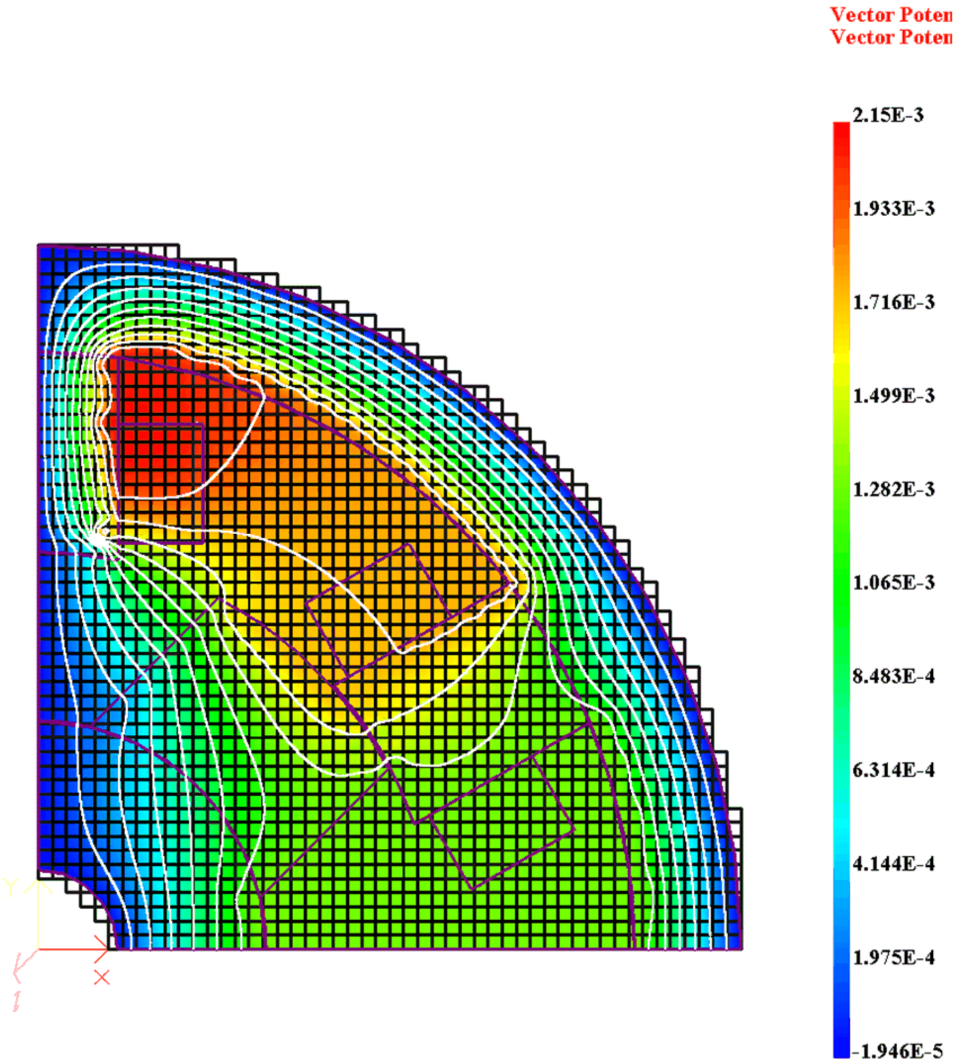

Figure 7-11. Magnetic vector potential and magnetic flux lines in the unaligned position

Three Dimensional Magnetostatic Problems

Several 3D examples are examined here to validate the implicit boundary method. The examples are published in [67]. The first example is an iron material in homogenous magnetic field. This example allows us to study the continuity or discontinuity of components of the flux density computed using IBFEM at material interfaces. The second example is a 3D coaxial cable that has an analytical solution for comparison. The third and the fourth examples are two solenoid actuators with plunger and clapper armatures. For each solenoid actuator, a cylindrical and a block like shape are analyzed. For the cylindrical actuator, the computed force and magnetic flux density are compared with 2D FEM solutions and the analytical solution from [18].

Example 7-2-1: Iron Block in a Homogenous Magnetic Field

The example of an iron cube in air subject to homogenous magnetic field has been used to verify a variety of formulations [4]-[5], [7], [51]. Figure 7-12 shows one-eighth of the system modeled considering its symmetry. The relative permeability of iron cube is 1000. The modeled region is subjected to a homogenous magnetic flux density $\mathbf{B}_0$ in the z-direction.

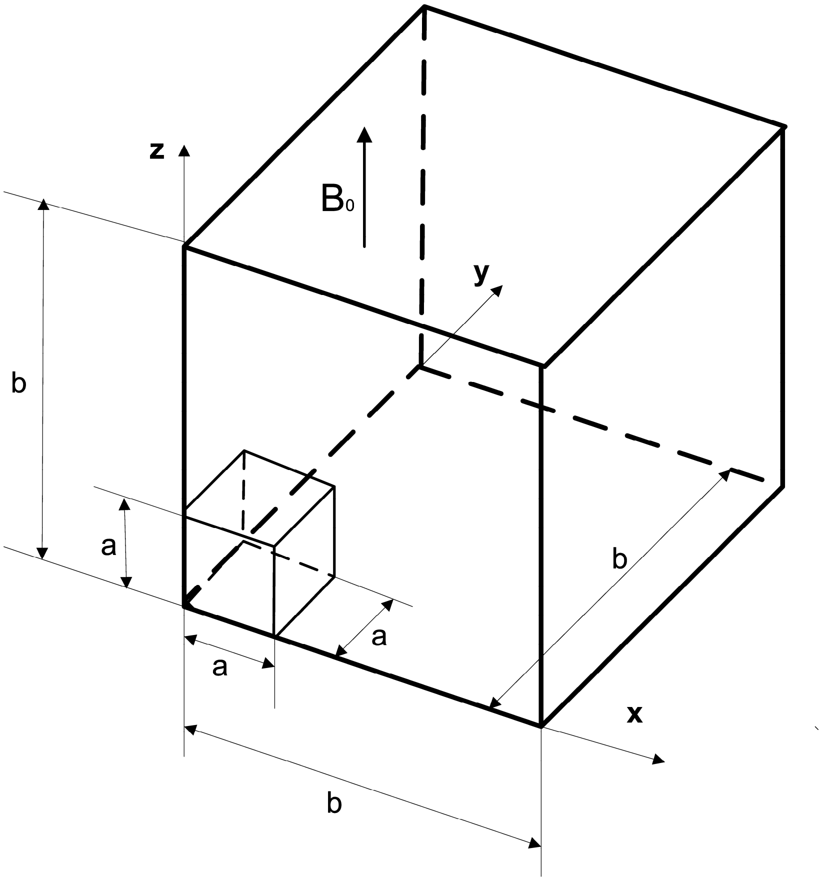

Figure 7-12. Iron cube in homogeneous magnetic field

The half-length of the iron cube edge is ‘a’. The symmetry planes are x=0, y=0 and z=0. The planes; x=b, y=b, and z=b represent the outer boundaries. A homogeneous magnetic field is applied in the z-direction with the aid of boundary conditions. On the outer boundaries, the Dirichlet boundary conditions are: $A_y = \frac{B_0 b}{2}$ and $A_z = 0$ on x=b and $A_x = -\frac{B_0 b}{2}$ and $A_z = 0$ on y=b. The dimensions used are $a = 20mm$, $b = 40mm$ and the flux density magnitude is $B_0 = 1.0\ \mathrm{T}$. In addition to these, the following essential boundary conditions are also imposed

$$\mathbf{n} \times \mathbf{A} = 0 \qquad \text{on } \Gamma_B \text{ (x=0 and y=0)} \tag{7-4}$$

$$\mathbf{n} \cdot \mathbf{A} = 0 \qquad \text{on } \Gamma_H \text{ (z=0 and z=b)} \tag{7-5}$$

As the magnetic flux density only exists in the z-direction, the normal components of magnetic flux density must be zero on the symmetry planes and the tangential component of magnetic field must be zero on planes normal to the z-direction.

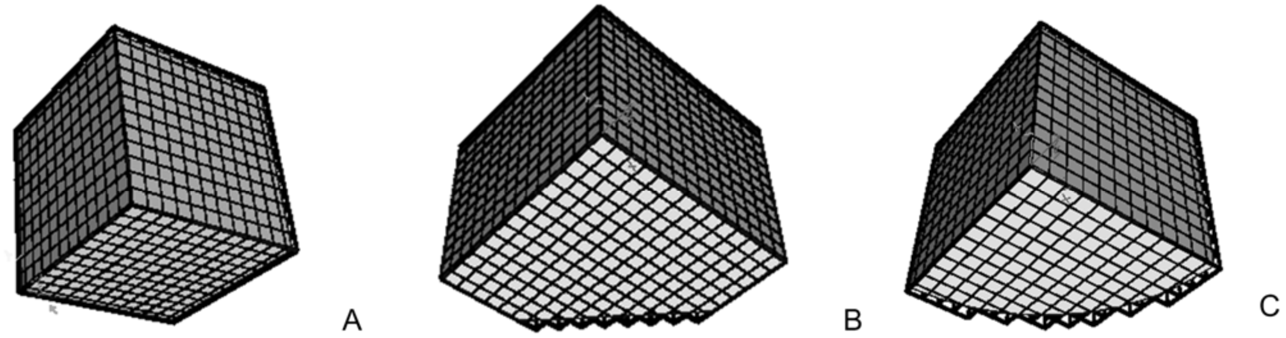

Figure 7-13. Iron objects with the same grid density. A) Cube, B) Octagonal prism, and C) Cylinder

In addition to modeling the iron cube, we have modeled two other shapes: octagonal prism and cylinder for the iron part as shown in Figure 7-13. Figure 7-13 shows the cube, the right octagonal prism, and the cylinder with the same grid density. The height of three objects is 20mm. The edge length of the right octagonal prism is 20mm. The cylinder is 20mm in radius. Along the observation line y=z=10mm, the location of boundary varies with change in the shape of the iron parts as shown in Figure 7-14.

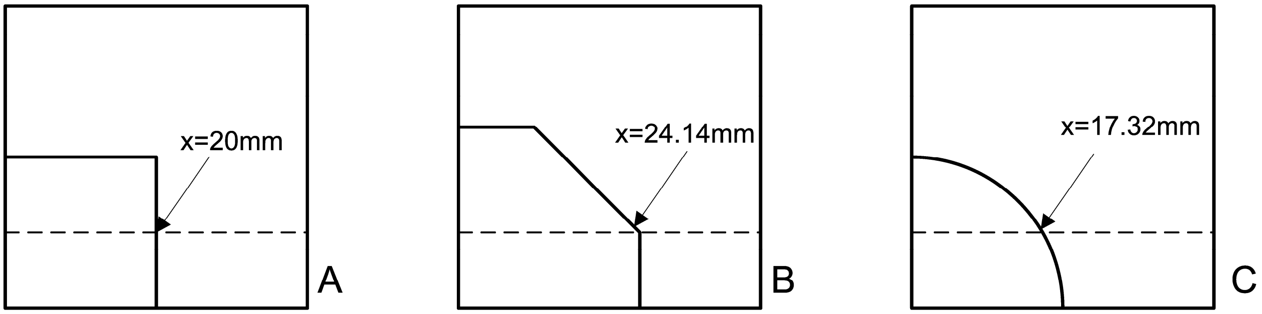

Figure 7-14. Cross-sections with the line y=z=10mm. A) Cube, B) Octagonal prism, and C) Cylinder

For the cube, the discontinuity happens at x=20mm, for the right octagonal prism, at x=24.14mm, for the cylinder, at x=17.32mm. The total number of elements is 12167. Using the same number of elements and the same boundary conditions as above, the variation on the three components of B along the line y=z=10mm are obtained as shown in Figure 7-15.

Figure 7-15 A shows that magnetic flux density in the x-direction is continuous only when the shape of the iron is cube because only in this case the normal component is parallel to the x-direction.

The discontinuity or continuity of magnetic flux density is successfully shown. But the discontinuity between two materials is not as sharp as in FEM. In order to improve IBFEM result, local grid refinement is needed.

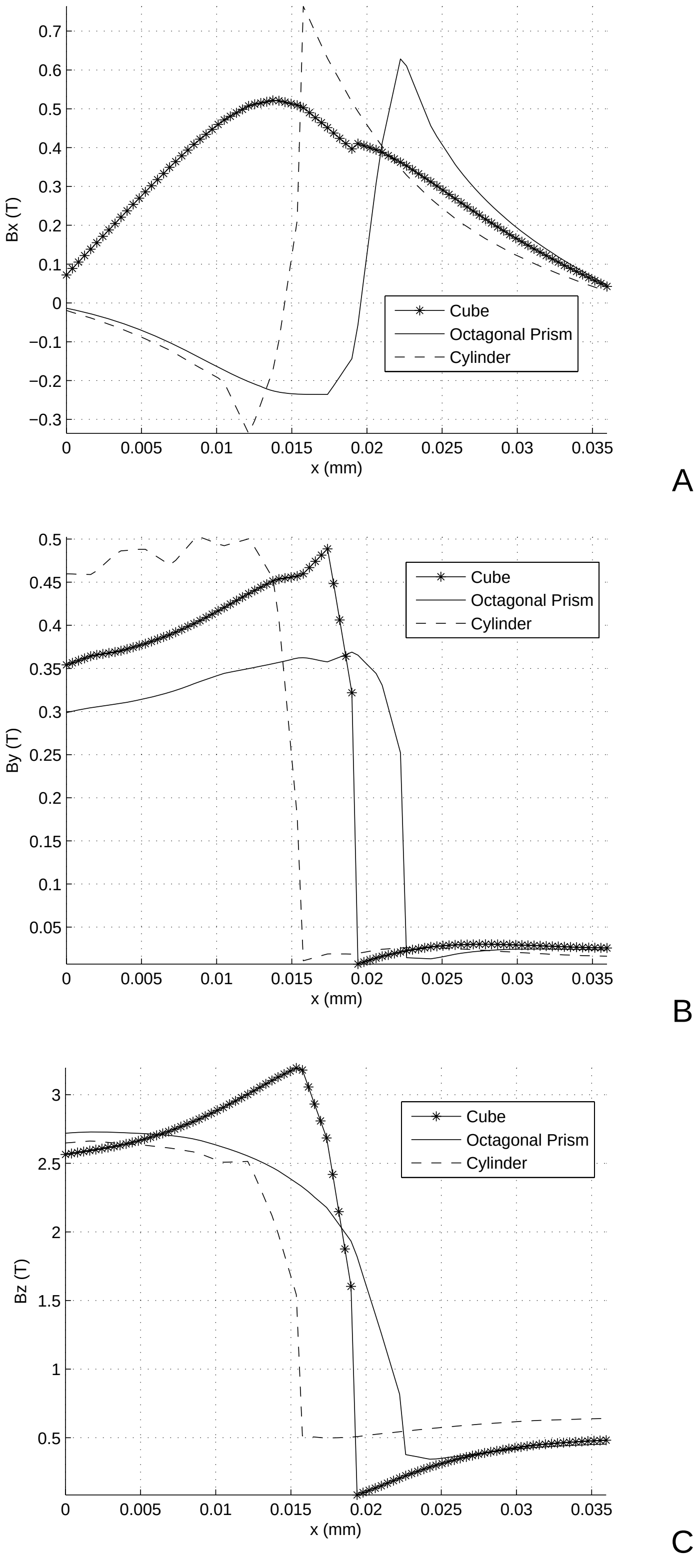

Figure 7-15. Components of B along the line y=z=10mm. A) Bx, B) By , and C) Bz

Example 7-2-2: 3D Coaxial Cable

A coaxial cable consists of an inner conductor, an insulator, and an outer conductor. A coaxial cable problem is a well-known problem for 2D magnetostatic - problem. As the current density and the magnetic vector potential has only one component in the z-direction, the analytical solution is easily obtained using the ampere’s law. Using this example, we tried to solve an electro-magnetostatic problem sequentially. In the first step, the current density in each conductor is calculated through 3D electrostatics. In the next step, using the computed current density, magnetic field in circumferential direction is obtained through 3D magnetostatic analysis. The calculated magnetic field is compared with the analytical solution.

The governing equations for the electro-magnetostatic problem are described as follows

$$\begin{aligned} -\nabla\cdot\left(\sigma\nabla V\right) &= 0 && \text{in } \Omega \\ \nabla\times\left(\nu\nabla\times\mathbf{A}\right) &= \mathbf{J} && \text{in } \Omega \end{aligned} \tag{7-6}$$

where, the current density for magnetostatics is $\mathbf{J} = -\sigma\nabla V$. Due to circular symmetry of the geometry, only a quadrant of the coaxial cable is created. Figure 7-16 shows the coaxial cable model using three separate structured grids.

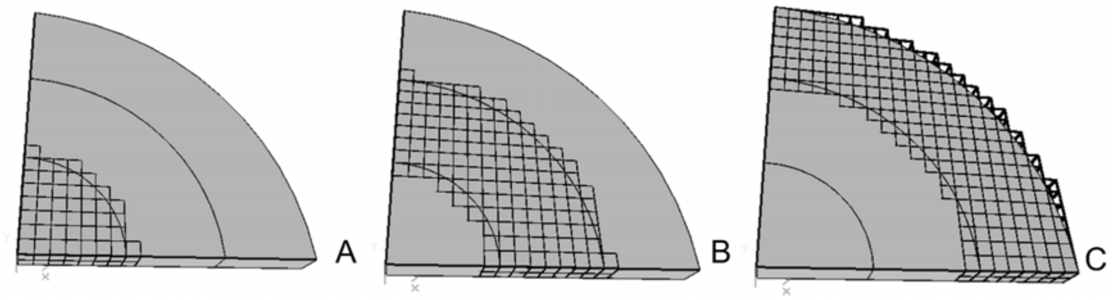

Figure 7-16. 3D coaxial cable model with the structured grid. A) Inner conductor, B) Insulator, and C) Outer conductor

The radii of the inner conductor, the insulator and the outer conductor are a , b and c . The height of the three components is d . The inner and outer conductors carry the same amount of total current in opposite directions. The total current flowing through each conductor is I . The current flows in the axial direction (the z-direction) and the current density is assumed to be uniform. The analytical solution of the magnetic field in circumferential direction can be Equation 7-1 from the 2D coaxial cable example. The following values of current and radii were used in the numerical model: $I = 1000A$, $a = 0.5$, $b = 1$, $c = 1.5$ and $d = 0.2$ mm. The current density of the inner conductor is computed to be 1273 A/mm2 and 254.6 A/mm2 in the outer conductor. The electric conductivity of the conductors is set equal to $10^3 S/mm$, and the insulator is equal to $10^{-3} S/mm$. In order to obtain $I = 1000A$, the voltage difference in the top and the bottom surfaces is set to 0.25 V in the inner conductor and 0.05 in the outer conductor. Figure 7-17 shows the magnitude of the magnetic field that was computed using 8 node hexahedral elements. It shows that the maximum magnetic field value is at the interface between the inner conductor and the insulator and has a value of $3.351 \times 10^2 A/mm$. This is close to the value obtained from the analytical solution which is $3.183 \times 10^2 A/mm$.

Figure 7-18 shows the magnetic field in the hoop direction varying with the radius. H8 means hexahedron element with 8 nodes. H8S stands for H8 with smoothing. After smoothing, the result of IBFEM is very close to the analytical solution.

Figure 7-19 shows the convergence plot for H1 norm using 8 node hexahedral elements. H1 norm is defined as Equation 7-2. The H1 norm decreases as the larger number of elements is used.

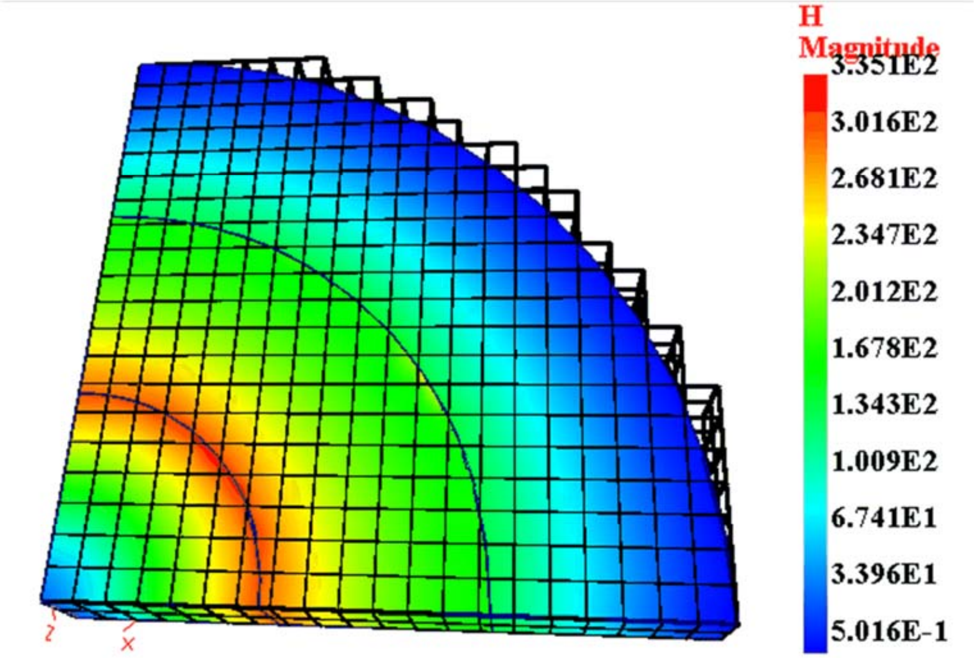

Figure 7-17. Magnitude of H field for 3D coaxial cable

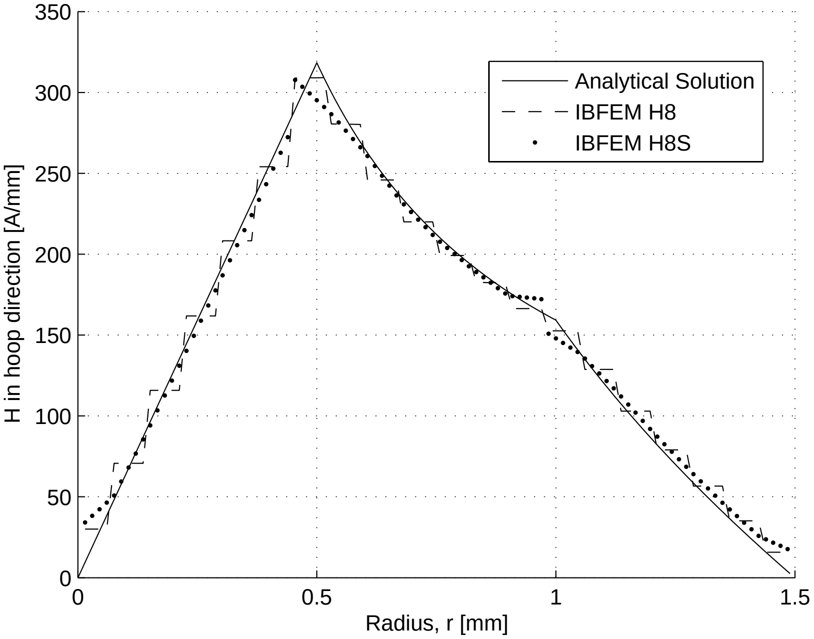

Figure 7-18. Magnetic field in the circumferential direction versus. radius

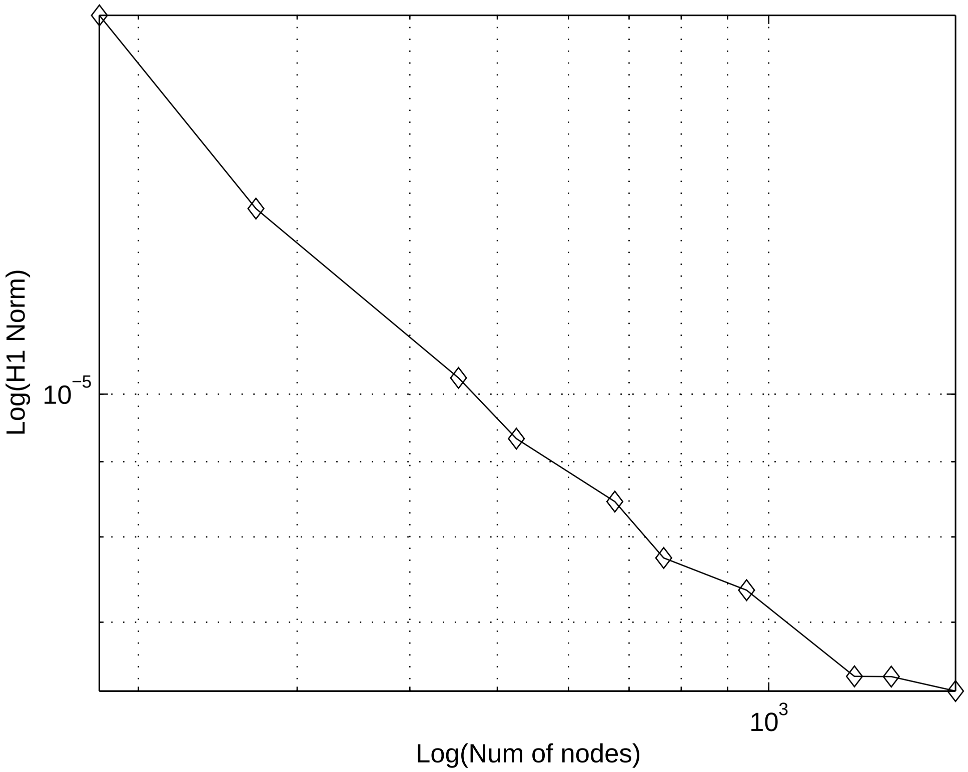

Figure 7-19. Convergence plot for H1 norm

Example 7-2-3: 3D Plunger Solenoid Actuator

Solenoid actuators have armature (moving part) and stator (stationary part). The armature is made of steel laminates in order to reduce eddy current effect. The stator has solenoid coil which is wound into shapes such as cylinder, cubic, parallelepiped and so on. Solenoid actuators can produce linear motion of the armature and have several types of actuators depending on the shape of the armature.

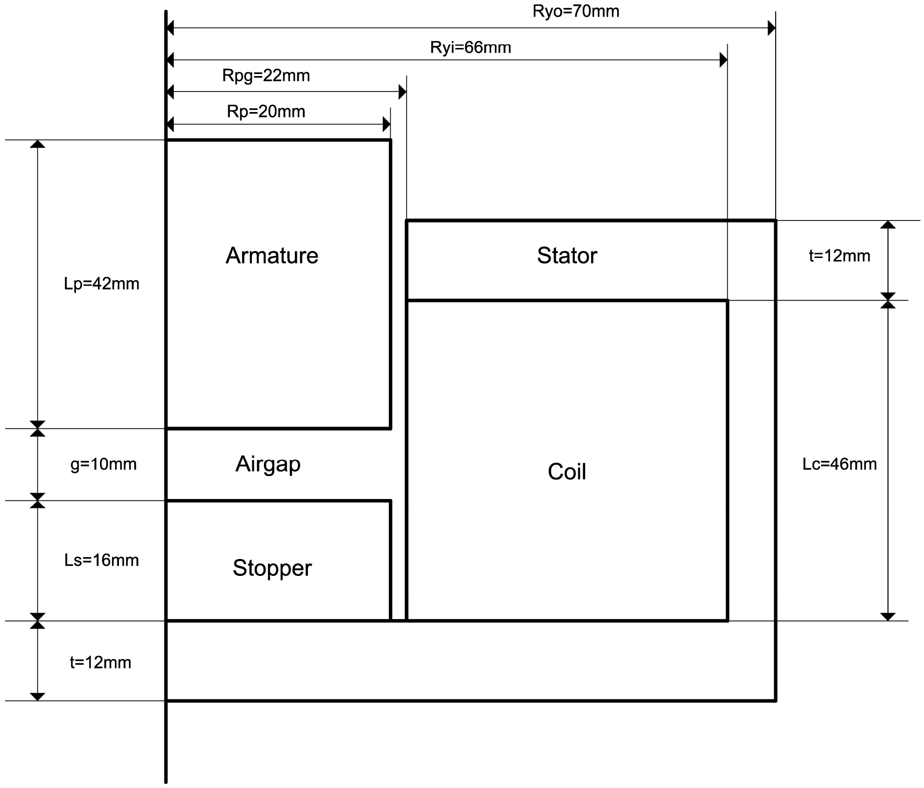

Figure 7-20. Plunger solenoid actuator of axisymmetric geometry

Figure 7-20 shows a solenoid actuator with plunger armature from [18]. The plunger is cylindrical and the solenoid is axisymmetric. The magnetic force only acts at the end of the plunger. The number of turns N=400 and the current I=4A. The relative permeability of the stator, the armature and the stopper is $\mu_r = 2000$ and $\mu_r = 1$ in the coil. The dimensions are provided in the Figure 7-20. Using the reluctance method, the magnetic flux density in the air gap is B=0.1715 T and the magnetic force is F =14.7 N. Brauer [18] also provided the following 2D FEM results: B=0.170 T and F =19.34 N. Using the similar dimensions, two different plunger solenoid actuators with different shapes were created as shown in Figure 7-21.

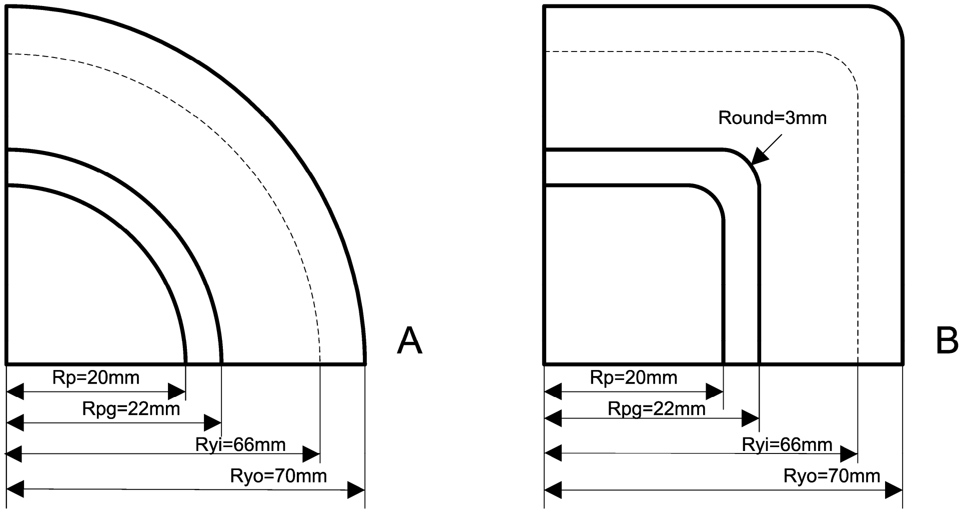

Figure 7-21. Top views of two plunger actuators. A) Cylindrical plunger, and B) Brick plunger

Figure 7-21 A is the top view of the cylinder actuator. Figure 7-21 B is the top view of the brick shaped actuator. The corners of the brick plunger are rounded. The former can be modeled as 2D axisymmetric magnetostatic problem. However, the latter one can only be analyzed using 3D magnetostatics.

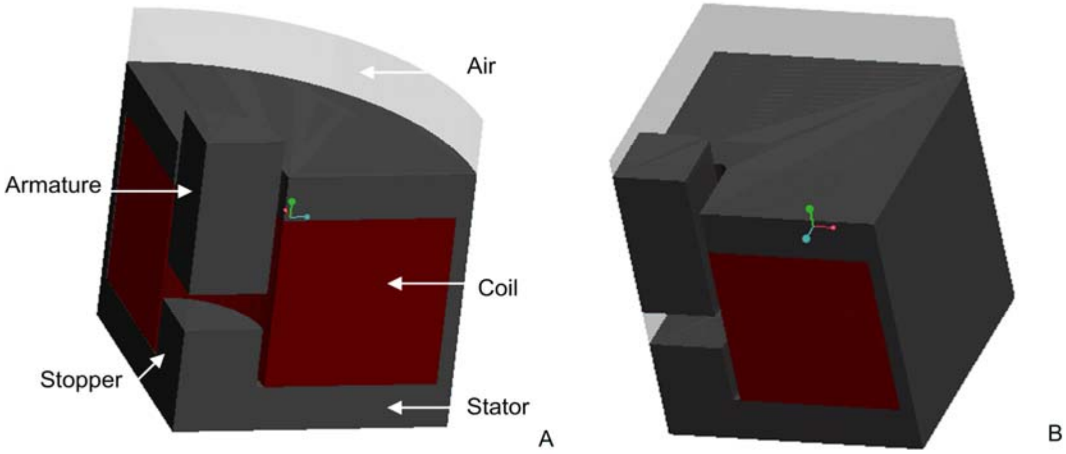

Figure 7-22. 3D solid model of solenoid actuators with plunger armatures. A) Cylindrical plunger, and B) Brick plunger.

Figure 7-22 shows 3D solenoid actuator model created by Pro/Engineering. In order to reduce the computation effort, we created one fourth of the whole model and modeled air only over the armature. The armature is moveable in the y-direction. In order to obtain the same current density as in the 2D axisymmetric problem, a voltage difference is applied between the two faces of the coil part. The voltage difference is equal to 0.0546 V when the conductivity of the coil is $\sigma = 10^6 S/m$. The essential boundary conditions of $V1 = 0.0273$ and $V2 = -0.0273$ are imposed on each face of coil parts. The same voltage boundary conditions are applied for the brick actuator.

Using the computed current density from 3D electrostatics, we can calculate magnetic flux density and magnetic field. The boundary conditions at the symmetric planes are applied as $\mathbf{n} \times \mathbf{A} = 0$. The computed magnetic flux density is shown in Figure 7-23.

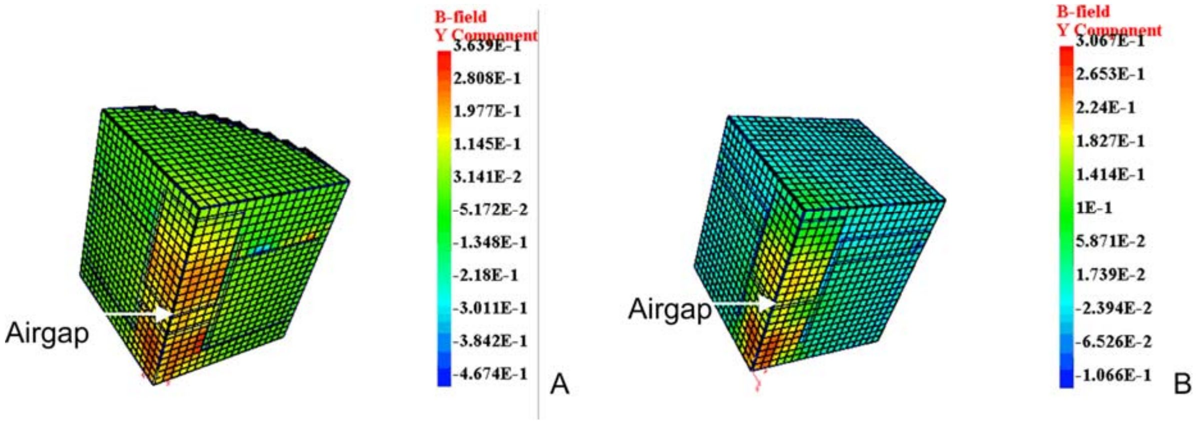

Figure 7-23. The magnetic flux density in the y-direction for two plunger solenoids. A) Cylindrical plunger, and B) Brick plunger

According to [18], the analytical solution is 0.1715 T and the FEM result is about 0.170 T. The computed magnetic flux density is between 0.114 and 1.977 T for the cylindrical plunger. The computed magnetic field density in the y-direction is shown in Figure 7-24.

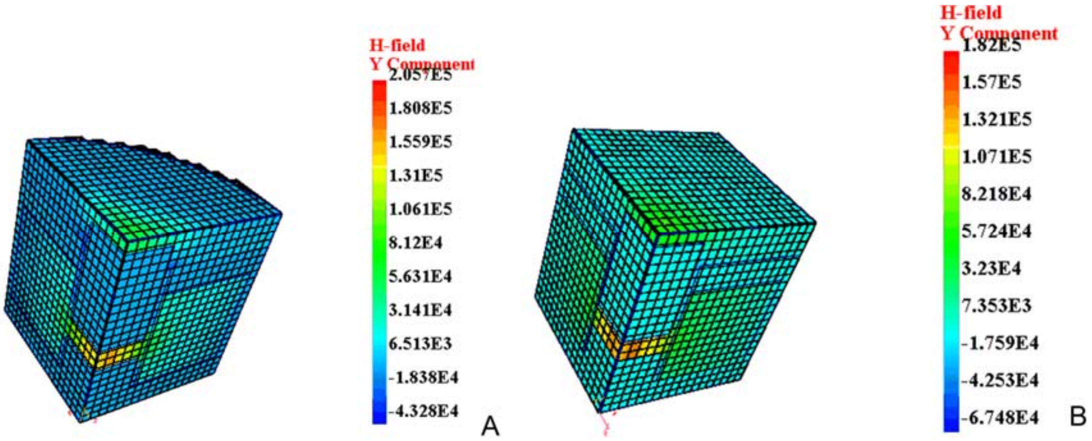

Figure 7-24. The magnetic field in the y-direction for two plunger solenoids. A) Cylindrical plunger, and B) Brick plunger

Figure 7-24 A shows the computed magnetic field in the y-direction is approximately equal to $1.364\times10^{5}\ \mathrm{A/m}$ which is computed using the reluctance method [18]. Using the magnetic field and flux density, the computed magnetic force on the cylindrical armature is 18.33 N which is quite close to the force calculated by 2D FEM. For the brick armature, the computed force is 19.56 N. According to this analysis, the force on the brick armature is larger than that on the cylindrical armature because the cross-sectional area of the brick armature ($1.592\times10^{-3}\ \mathrm{m}^{2}$) is larger than the area of the cylindrical armature ($1.257\times10^{-3}\ \mathrm{m}^{2}$).Figure 7-25 shows magnetic force versus gap length. When the gap is changed from 2mm to 10mm, the magnetic force decreases. Even though the gap varies, the same mesh is used for all the models. For the cylindrical plunger solenoid, the number of nodes is 10984. For the brick plunger solenoid, the total number of nodes is 10876. When the shape of the actuator is a cylinder, the analytical solution using the reluctance method can be compared with the results of 3D cylindrical plunger model. The computed values are higher than the analytical values because the reluctance method ignores fringing effect. Magnetic force of the brick plunger is a little higher than the force of the cylindrical plunger.

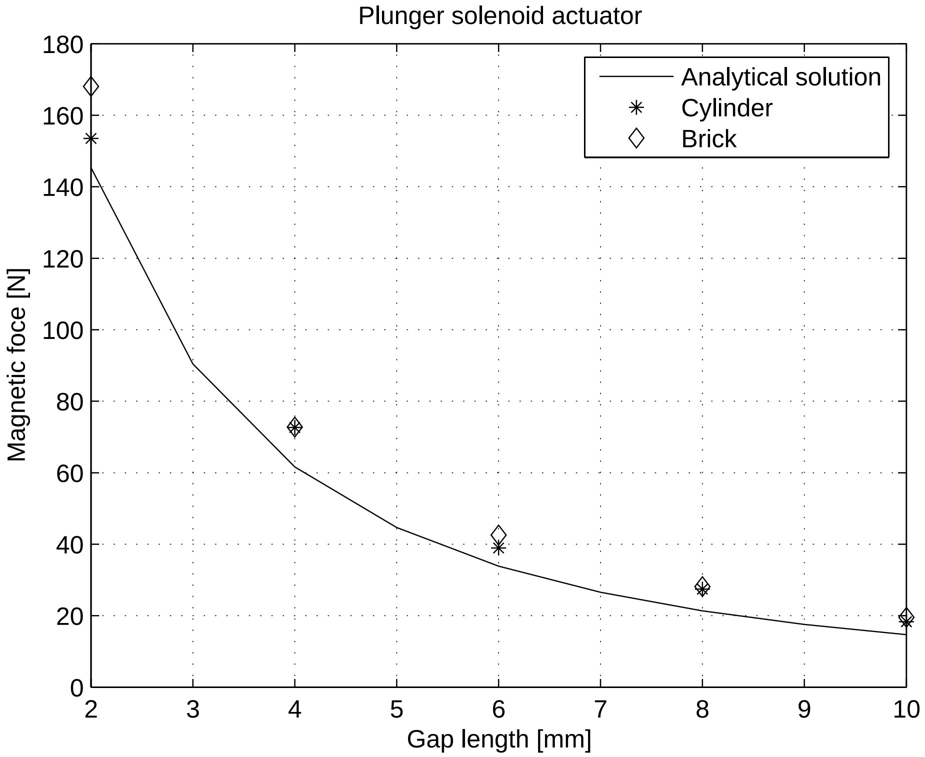

Figure 7-25. Magnetic force versus gap length for plunger solenoids

Example 7-2-4: 3D Clapper Solenoid Actuator

One of other popular solenoid actuators is a clapper solenoid actuator. Figure 7-26 shows a solenoid actuator with clapper armature from [18]. Clapper armature can have linear movement by using voltage or current control. Armature and stator are made of thin steel laminations with relative permeability of 2000. This clapper solenoid actuator is axisymmetric. The number of turns N=2000 and the current I=1A. The dimensions are provided in the Figure 7-26. Using the reluctance method, the magnetic flux density in the right air gap is B=0.56 T and the magnetic force is F =240 N. According to [18], 2D FEM results are B=0.82 T on the inner pole and 0.45 T on the outer pole and F =279.41 N. Using the similar dimensions, two different shapes of the clapper solenoid actuators are created in shown in Figure 7-27.

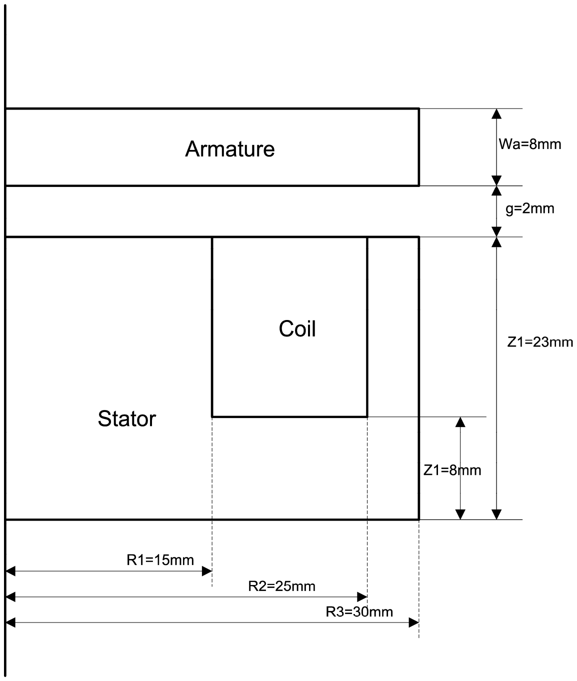

Figure 7-26. Clapper solenoid actuator of axisymmetric geometry

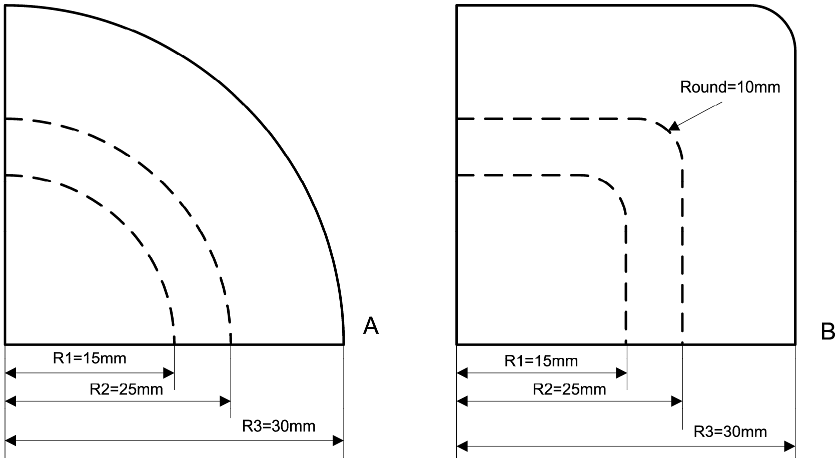

Figure 7-27. Top views of two clapper actuators. A) Cylindrical clapper, and B) Brick clapper.

Figure 7-27 A is the top view of the cylinder actuator. Figure 7-27 B is the top view of the brick actuator. The corners of the brick armature are rounded. The former can be approximated for 2D axisymmetric magentostatic analysis. However, the latter one should be analyzed using 3D magnetostatics.

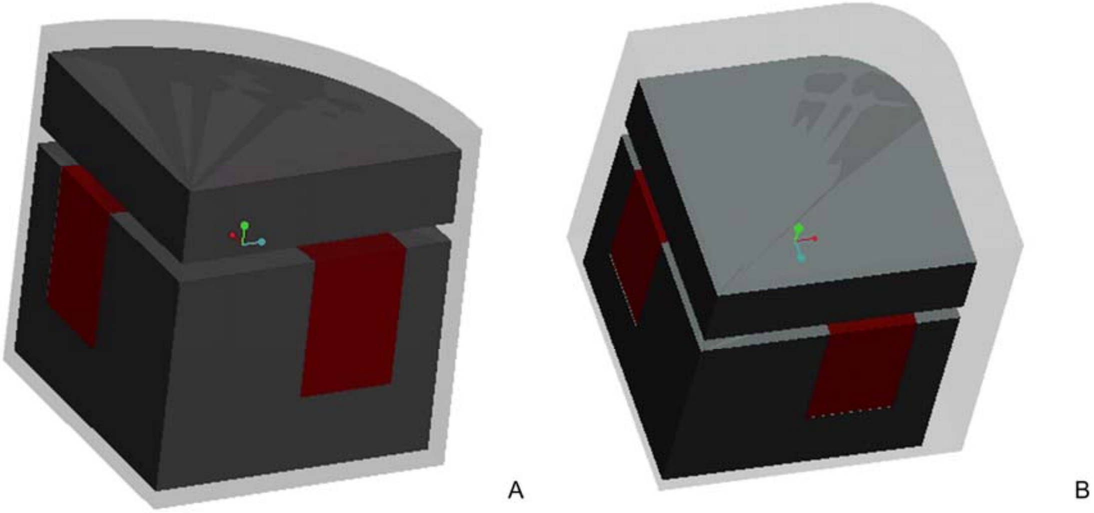

Figure 7-28. 3D solid model of solenoid actuator with clapper armatures. A) Cylindrical clapper, and B) Brick clapper

Figure 7-28 shows 3D solenoid actuator model created by Pro/Engineering. In order to reduce the computation effort, we created one fourth of the whole model and the air model that only covers the armature. The armature is moveable in the y-direction. In order to obtain the same current density as in 2D axisymmetric problem, the voltage difference, equal to 0.4188 V, was applied between two faces of the coil part. The conductivity of the coil is $\sigma = 10^6 S/m$. The essential boundary conditions of $V1 = 0.2094$ and $V2 = -0.2094$ are imposed on each face of coil parts. The same voltage boundary conditions are applied for the brick actuator.

After computing current density distribution on conductor, we can calculate magnetic flux density and magnetic field. The boundary conditions at the symmetric planes are applied as $\mathbf{n} \times \mathbf{A} = 0$. The computed magnetic flux density is shown in Figure 7-29.

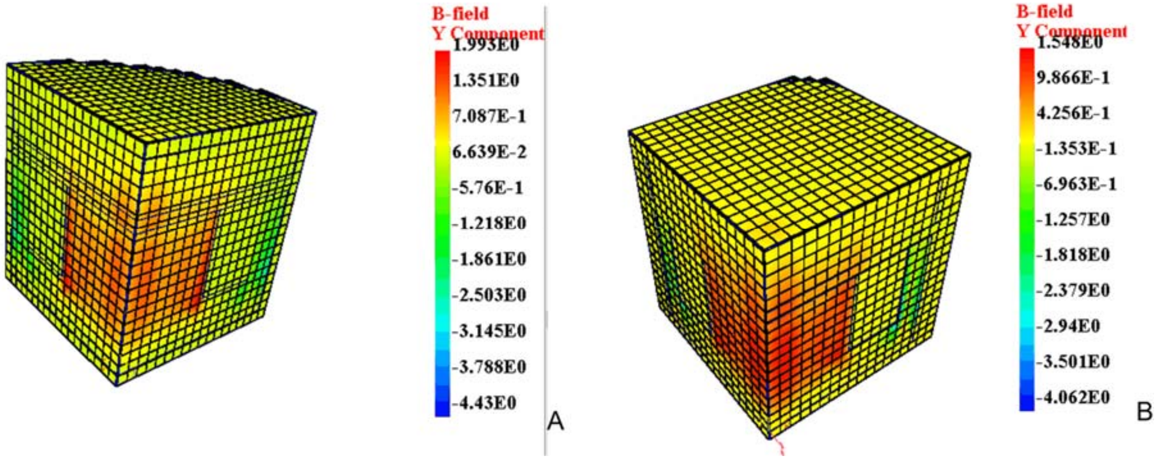

Figure 7-29. The magnetic flux density in the y-direction for two clapper actuators. A) Cylindrical clapper, and B) Brick clapper

The computed magnetic flux density is approximately 1.3 T for the cylindrical clapper.

The computed magnetic field density in the y-direction is shown in Figure 7-30.

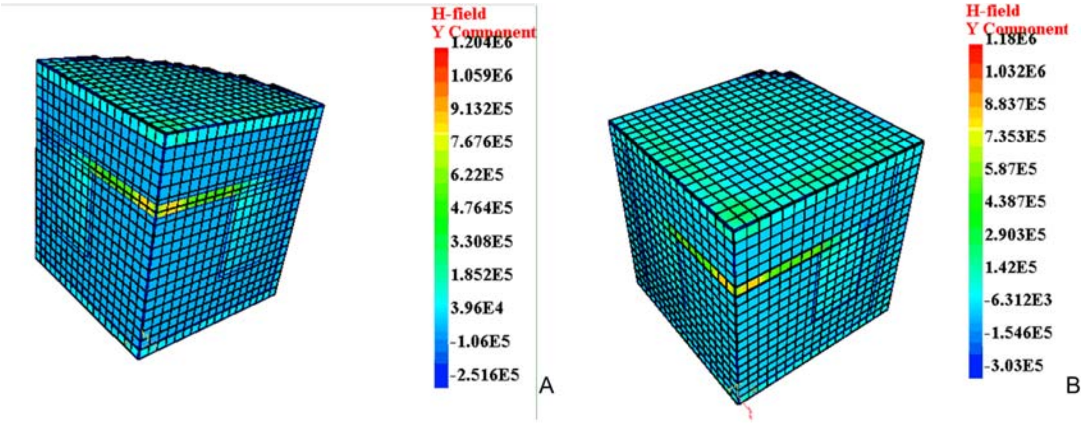

Figure 7-30. The magnetic field in the y-direction for two clapper actuators. A) Cylindrical clapper, and B) Brick clapper

Figure 7-30 A shows that the computed magnetic field in the y-direction is approximately $7.6\times10^{5}\ \mathrm{A/m}$. Using the magnetic field and flux density, the computed magnetic force on the cylindrical armature with the forced area of $2.827\times10^{-3}\ \mathrm{m}^{2}$ is 284.76 N which is quite close to the force calculated by 2D FEM. For the brick armature with the forced area of $3.514\times10^{-3}\ \mathrm{m}^{2}$, the computed force is 320 N.

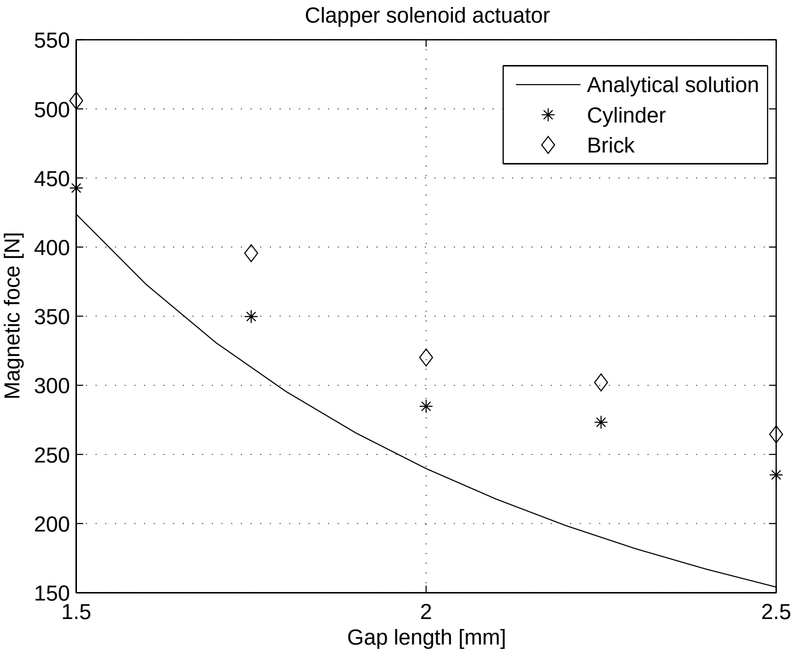

Figure 7-31. Magnetic force versus gap length for clapper solenoids

Figure 7-31 shows magnetic force varying with the gap length. The gap length is changed from 1.5mm to 2.5mm. The analytical solution for the cylindrical clapper actuator is lower than the computed one. The magnetic force of the brick clapper actuator is higher than that of the cylindrical clapper actuator because the forced area on the armature is larger.

Magnetostatic Problems with Permanent Magnets

Two examples including the permanent magnet are examined here to validate the implicit boundary method. The first example is borrowed from the model library of the commercial software (Comsol). Using a U-shaped permanent magnet, the computed magnetic fluxes are compared to the results of Comsol. The second example is a 3D cylindrical permanent magnet that has an analytical solution for comparison.

Example 7-3-1: U-Shaped Permanent Magnet

A U-shaped permanent magnet is analyzed using IBFEM and compared with a commercial software (Comsol). The drawing of the model is shown in Figure 7-32 A. The example is a 2D magnetostatic problem that includes three different regions; iron, air, magnets. *R1* and *R2* represent the magnets or magnetization regions. *R3* represents iron. *R4* indicates air. *R1* and *R2* are magnetized in the x-direction. *R1* has magnetization equal to 7.5e5 A/m, and *R2* has magnetization equal to -7.5e5 A/m. Homogenous essential boundary conditions are applied on the boundaries of *R4*.

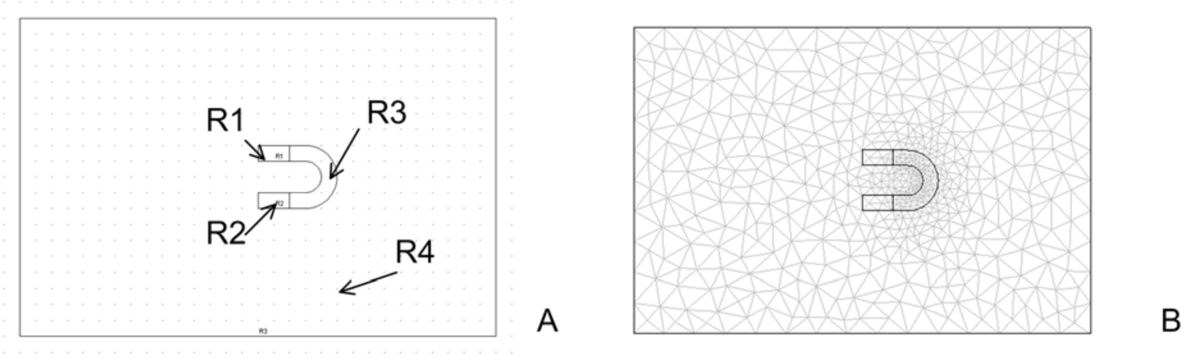

Figure 7-32. U-shaped permanent magnet model. A) Geometry model, and B) Conformal mesh

The finite element model uses 10286 quadrilateral elements to solve this problem as shown in Figure 7-32 B. The density of conformal mesh is denser near the permanent magnet.

Figure 7-33 and Figure 7-34 show surface plots and contour plots for magnetic vector potential. Figure 7-33 is the result from Comsol and Figure 7-34 is from IBFEM. In IBFEM, four node bilinear elements are used and the total number of the elements is 6600. According to the figures, both results are similar not only graphically but also numerically in terms of the magnetic vector potential.

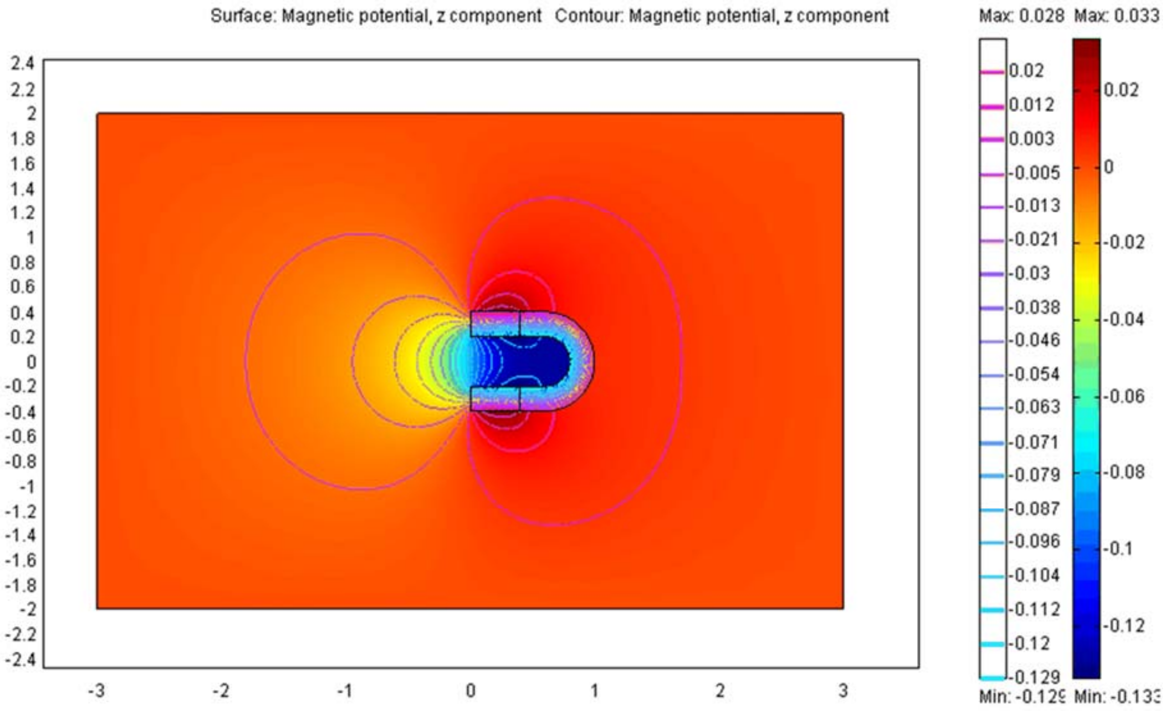

Figure 7-33. Surface and contour plots for magnetic potential from Comsol

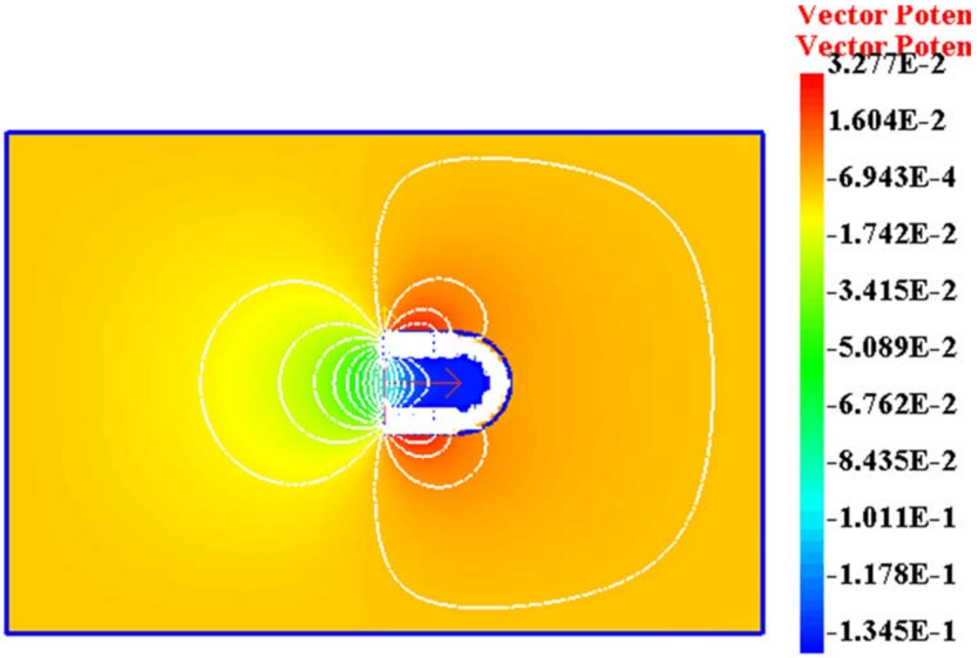

Figure 7-34. Surface and contour plots for magnetic potential from IBFEM

In order compare two results precisely, the magnetic field in the x-direction and the magnetic field density norm are obtained along a line. The line for comparison is shown in Figure 7-35. Figure 7-36 shows the magnetic field in the x-direction. IBFEM 3220e stands for IBFEM result using 3220 elements. The line plots show that the two IBFEM results are quite close to Comsol result.

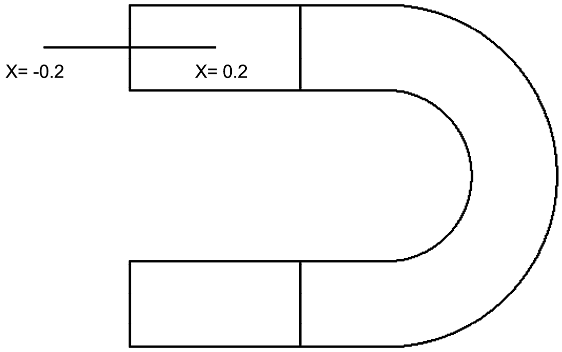

Figure 7-35. The observation line for the comparison

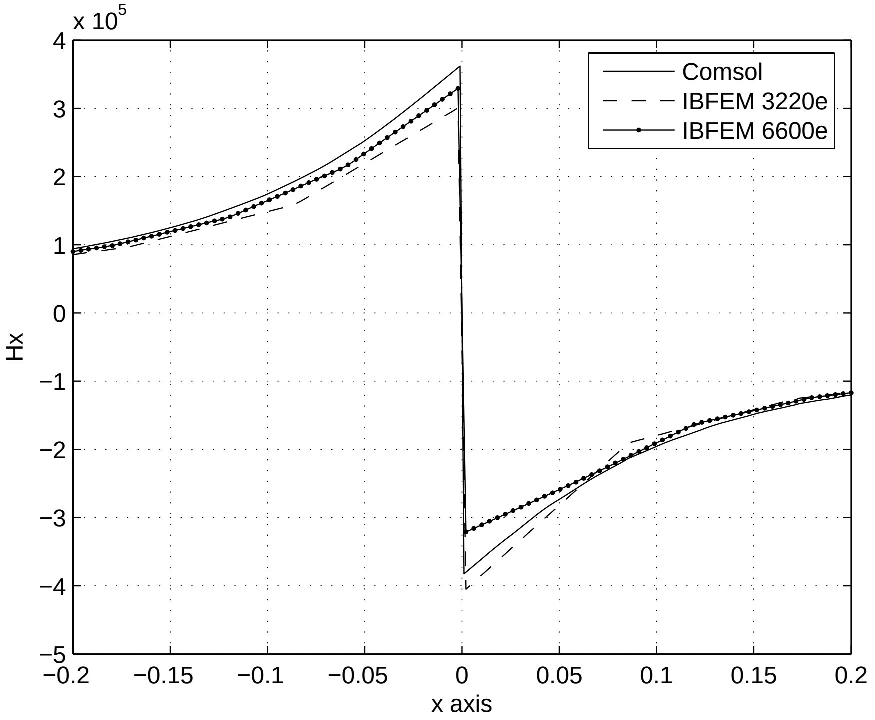

Figure 7-36. Magnetic field in the x-direction on the line

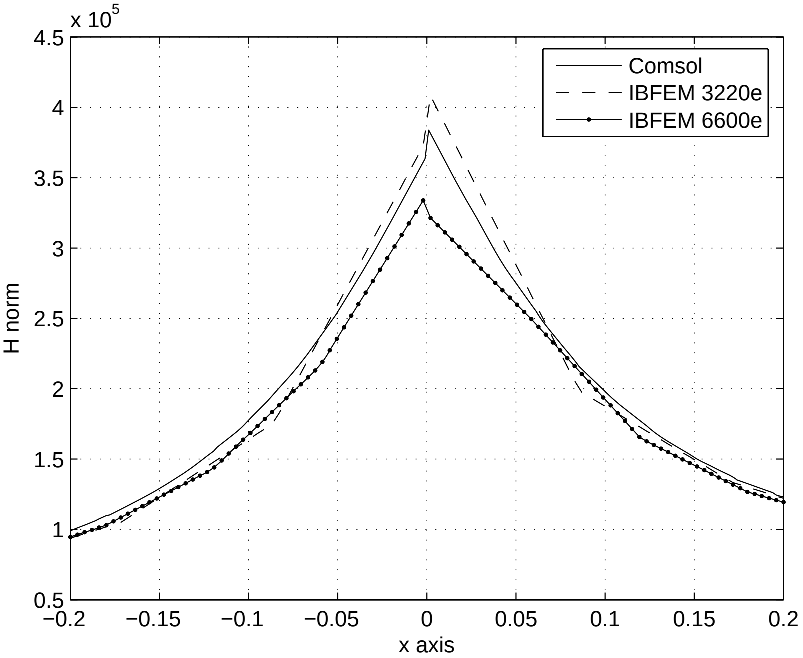

Figure 7-37. Magnetic field norm on the line

Example 7-3-2: Three Dimensional Cylindrical Magnet

A 3D cylindrical permanent magnet in free space is modeled as shown in Figure 7-38. Considering the symmetry, one fourth of the permanent magnet is created in order to reduce computation.

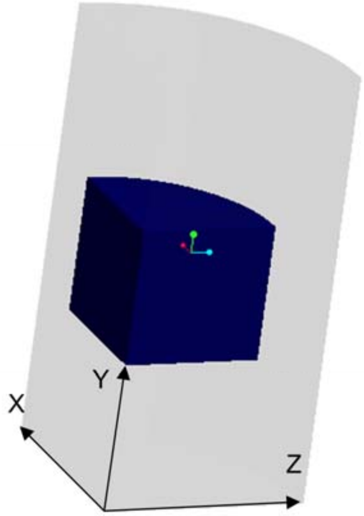

Figure 7-38. 3D solid model for cylindrical magnet in the air

Boundary conditions are $\mathbf{n}\times\mathbf{A}=0$ on the symmetry planes (x=0 and z=0). The radius r and the height h of the magnet are defined as 1 m. The magnetization vector (M_0) is 1 A/m in the y-direction. Under the conditions, the analytical solution of the magnetic field along the y axis is given by [2]:

$$H_y=\frac{M_0}{2}\left[\frac{B_-}{A_-}-\frac{B_+}{A_+}+\gamma\right] \tag{7-6}$$

where, $A_{\mp}=\sqrt{\left(\frac{R}{d}\right)^2+\left(\frac{z}{d}\mp\frac{1}{2}\right)^2}$, $B_{\mp}=\frac{z}{d}\mp\frac{1}{2}$, and $\gamma=\begin{cases}0 & \text{if } |z|\geq d/2\\ 2 & \text{if } |z|<d/2\end{cases}$.

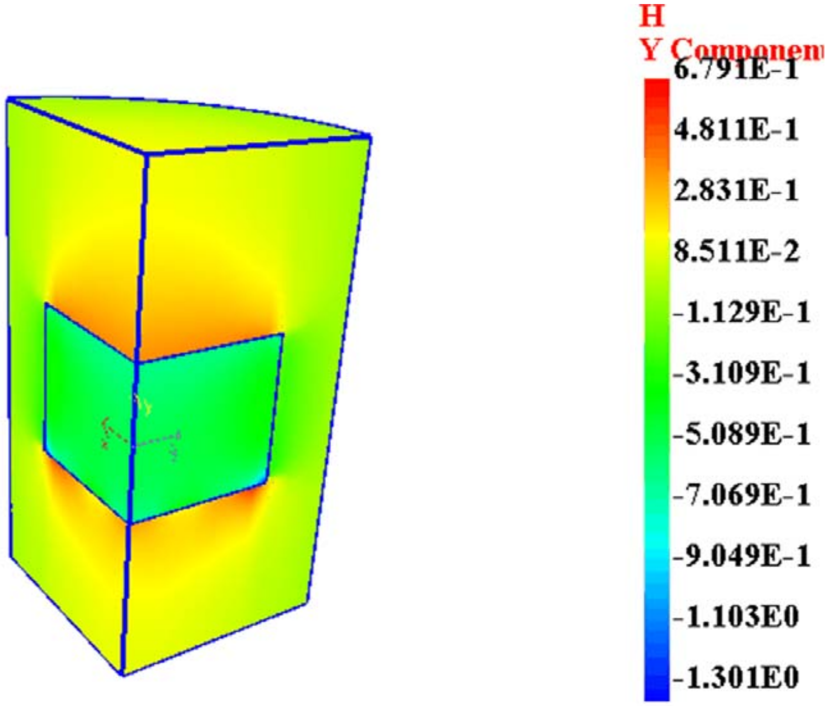

Figure 7-39. Magnetic field in the y-direction

Figure 7-39 shows the magnetic field in the y-direction. Eight node hexahedral elements are used and the total number of the elements is 20000. The result graphically shows the discontinuity at the material interface. Figure 7-40 shows the line plots for the magnetic field along the y axis. The result of Comsol was computed using a 2D axisymmetric model. As shown in the Figure, IBFEM result is close to the analytical solution and the comsol result. Some discrepancy of the magnetic field is founded at the location where it is far from the interface boundary. The result may be more accurate when the number of elements increases, the quadratic or cubic elements are used or an open boundary technique is applied.

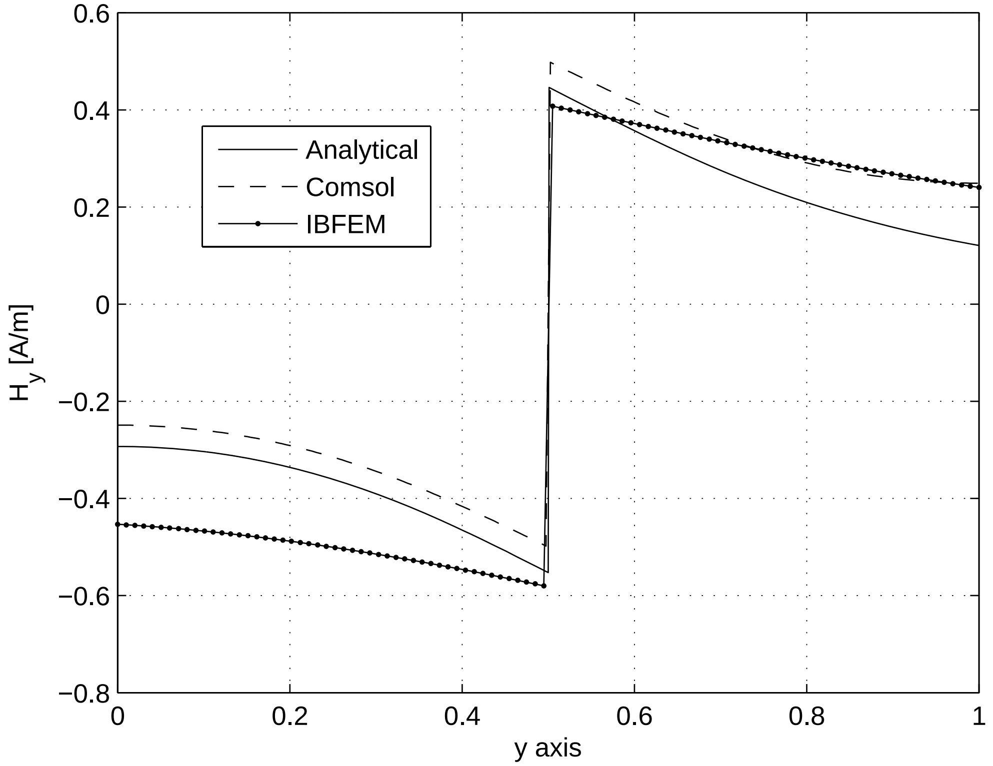

Figure 7-40. Magnetic field along y axis

Magnetostatic Problems with Open Boundary Techniques

Several examples with the open boundary techniques are examined here to validate the implicit boundary method. The first example is Example 7-3-1 with smaller analysis domain. The second is the entire model of the previous solenoid actuator from Example 7-1-2. The third example is to compute Lorentz force between two wires. These examples show how the open boundary techniques could improve results.

Example 7-4-1: U-Shaped Permanent Magnet with Open Boundary Techniques

For the previous example (Example 7-3-1), the large unbounded domain (6 x 4) was necessary with the truncation approach. The small air domain (1.6 x 1.4) is created as shown in Figure 7-41.

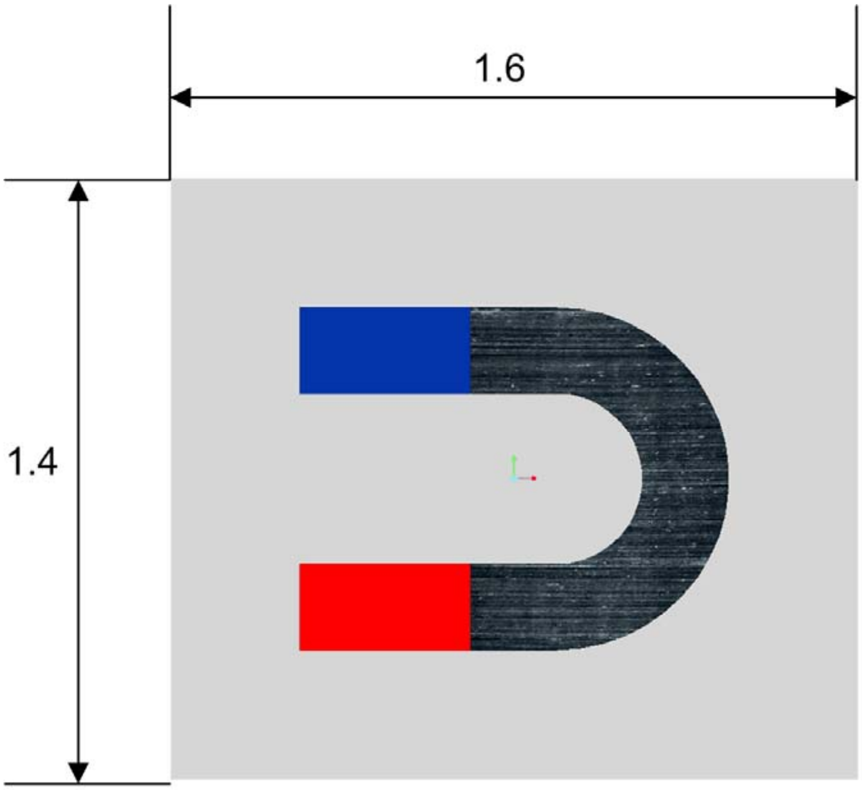

Figure 7-41. U-shaped permanent magnet with the reduced air domain

Two open boundary techniques (asymptotic boundary conditions and decay function infinite method) are applied on the outer boundaries. Figure 7-42 shows contour plots for magnetic vector potential for each technique. The total number of four node bilinear elements used in the model is 8888. The decay factor $L = 1$ for the decay function is used in infinite element method. Figure 7-42 A shows different contour pattern when the homogenous essential boundary is applied on the outer boundaries. Figure 7-43 shows magnetic field in the x-direction on the observation line as shown in Figure 6-35. EBC stands for the homogenous essential boundary conditions. The results using ABC are quite similar to the Comsol result. The result obtained using EBC has the largest error among them.

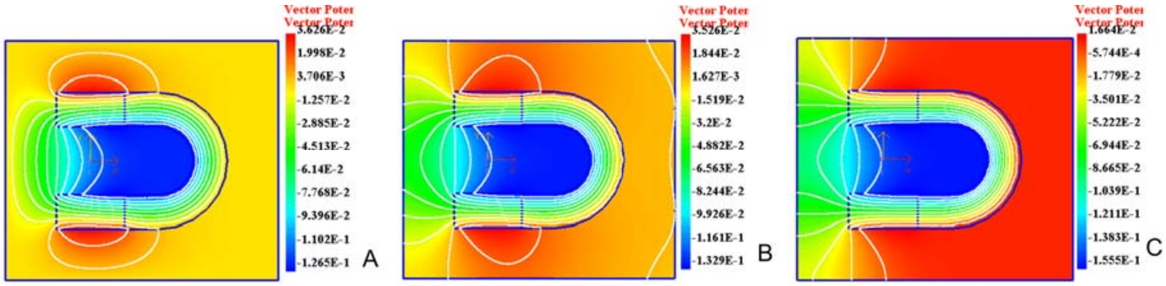

Figure 7-42. Contour plots for magnetic vector potential. A) Homogenous essential boundary conditions, B) Asymptotic boundary conditions and C) Decay function infinite element with *L*=1.

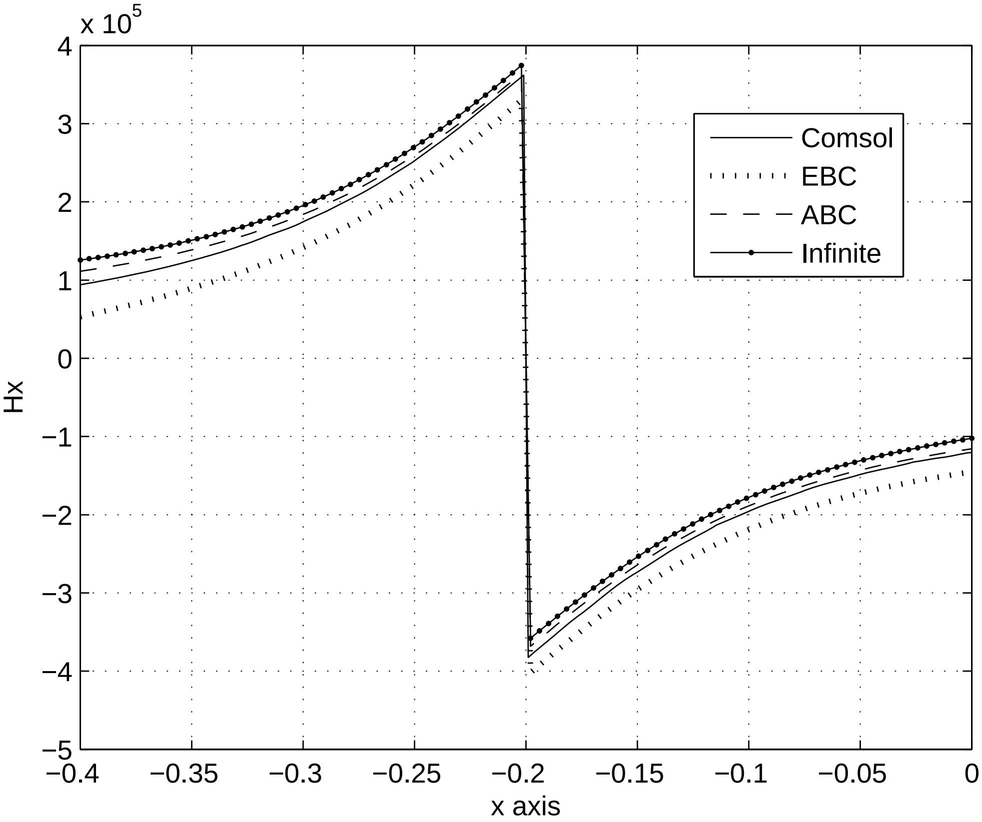

Figure 7-43. Magnetic field in the x-direction on the observation line

Example 7-4-2: 2D Clapper Solenoid Actuator with Open Boundary Techniques

The second example for open boundary techniques is extended from the previous solenoid actuator (Example 7-1-2). The whole actuator including smaller air domain is created as shown in Figure 7-44. Three open boundary techniques are applied on the other boundaries. The magnetomotive force *NI* and material properties of components are the same as in Example 7-1-2.

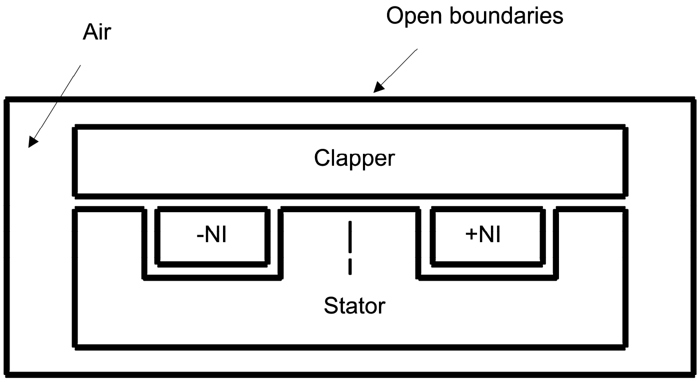

Figure 7-44. 2D Clapper solenoid actuator

When the gap length is 2mm, Figure 7-45 shows the contour plots for magnetic vector potential. Among the three results, the result using the homogenous essential boundary conditions differs from the other two. The quadratic b-spline elements are used for the analysis. The total number of elements is 7049. The computed forces for all open boundary techniques are as follows:

Homogenous essential boundary conditions (EBC): 269 N/m

Asymmetric boundary conditions (ABC): 276 N/m

Decay function infinite element method with L=1 (Infinite): 282 N/m.

The computed force using EBC is the lowest value. These computed forces can be also compared with the following values: the approximate solution using the reluctance method is 245.2N/m and the force computed by FEM with the ballooning method is 272 N/m from [18]. The computed force using ABC is quite close to the reference force from [18]. Therefore, using ABC can produce the most reliable answer in three techniques.

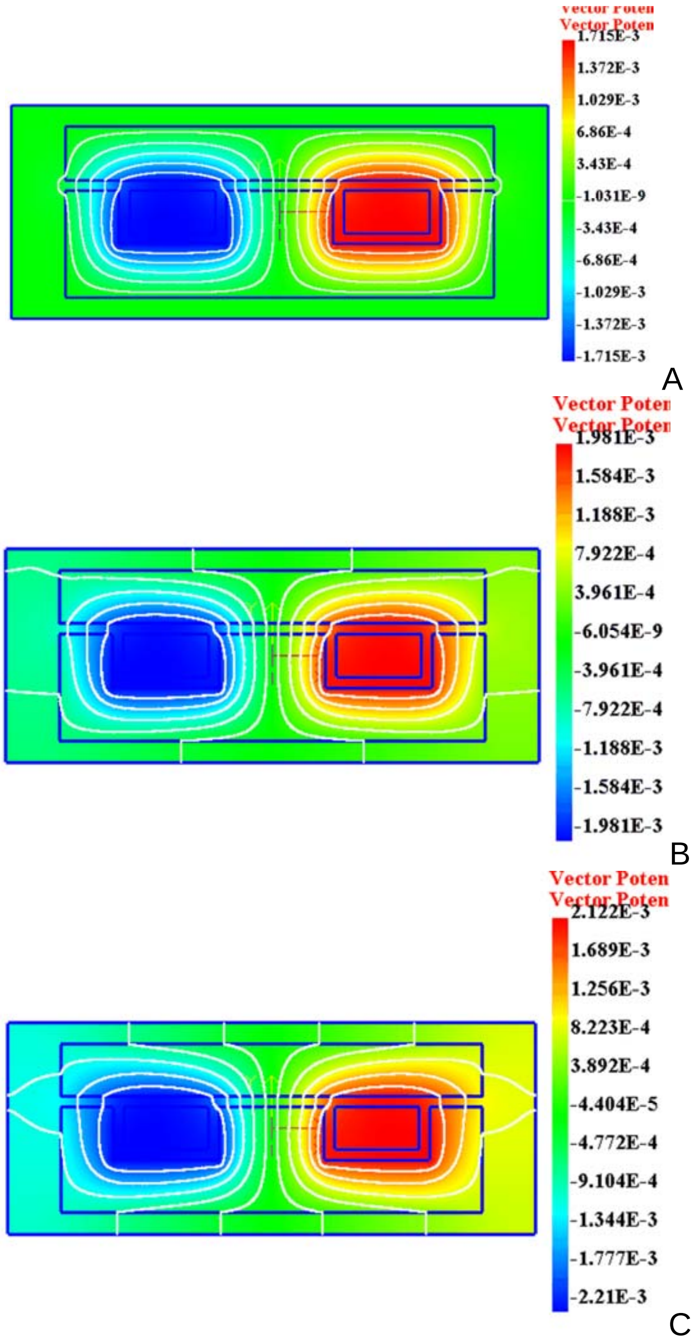

Figure 7-45. Contour plots of magnetic vector potential. A) Homogenous essential boundary conditions, B) Asymptotic boundary conditions and C) Decay function infinite element with *L*=1.

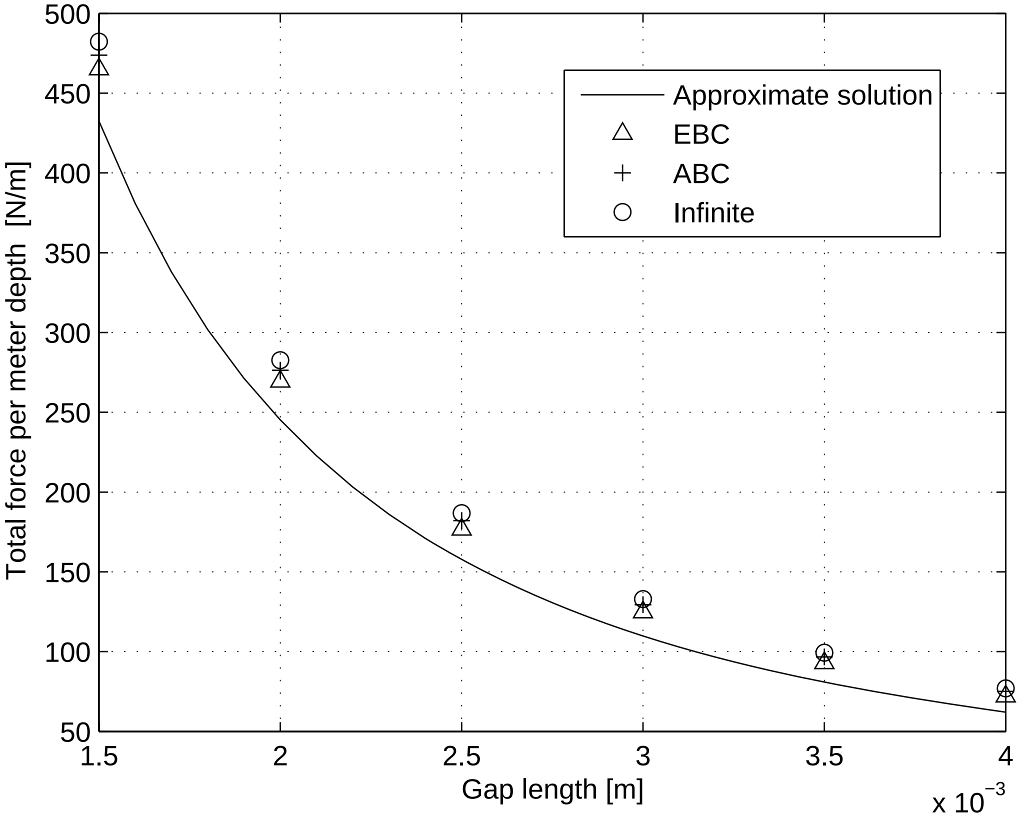

Figure 7-46. Magnetic force versus gap length

Figure 7-46 show the total force on the clapper armature as a function of the gap width. All computed values of total force follow the approximate solution using the reluctance method. The computed force using ABC is the best answer among them, a force that exits between the force using EBC and the force using the infinite element method.

Example 7-4-3: Force Between Two Parallel Wires

Two long straight parallel wires are separated by a distance *d*. The wires carry the same amount of current in the same direction as shown in Figure 7-47. Then an attractive force is created between the two wires.

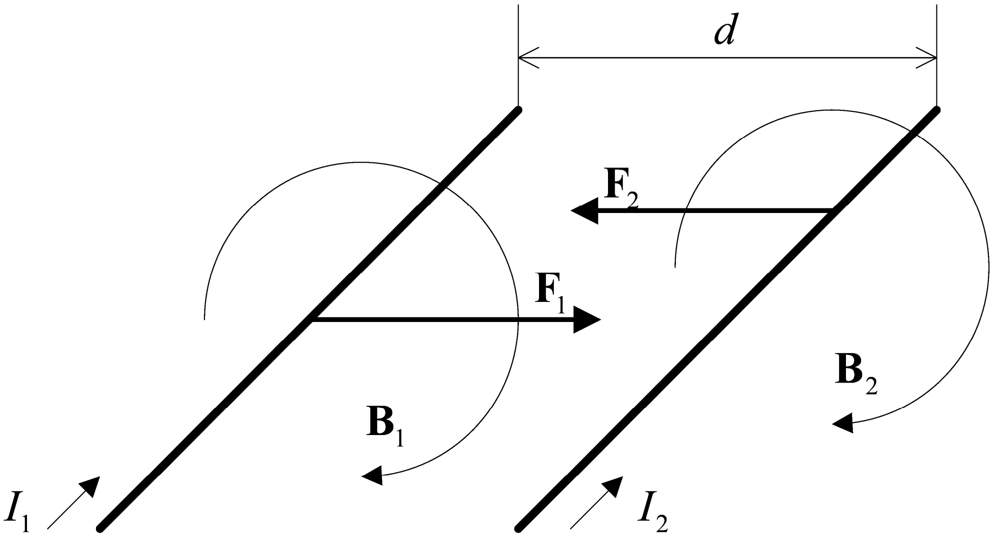

Figure 7-47. Two long parallel wires

Using the Ampere's law, the magnetic field at the 2nd wire caused by the current I_1 can be obtained as $B_1 = \dfrac{\mu_0 I_1}{2\pi d}$. According to the Lorentz force equation, the magnetic force per unit length at the 2nd wire is stated as

$$\frac{F_2}{l} = \frac{\mu_0 I_1 I_2}{2\pi d} \tag{7-7}$$

where, l is the wire length. The same amount of the magnetic force is obtained at the 1st wire. When $d = 1\ \mathrm{m}$ and $I_1 = I_2 = 1\ \mathrm{A}$, the magnetic force per unit length becomes $2\times10^{-7}\ \mathrm{N/m}$.

The radius of the wire is $0.05\ \mathrm{m}$, and the surrounding air area of $1.9\times1.9\ \mathrm{m}^2$ is modeled. Open boundary condition is applied on the outer boundary using the truncation method, the asymptotic boundary conditions, or infinite element method. Quadratic B-spline elements were used. The total number of nodes was 10520. The contour plots of the computed magnetic vector potential are shown in Figure 7-48. The magnetic force per unit length is computed as follows; $2.53\times10^{-7}\ \mathrm{N/m}$ using the truncation approach, 1.63×10^{-7} N/m using the asymptotic boundary condition, and 2.42×10^{-7} N/m using the decay function infinite element method with *L*=0.10. Using the asymptotic boundary condition, the computed force is closer to the analytical solution when $d = 1$ m. The other methods show similar results in terms of the contour plot and the magnetic force. It is because the decay length is so short that the decay function infinite element method is as same as the truncation approach.

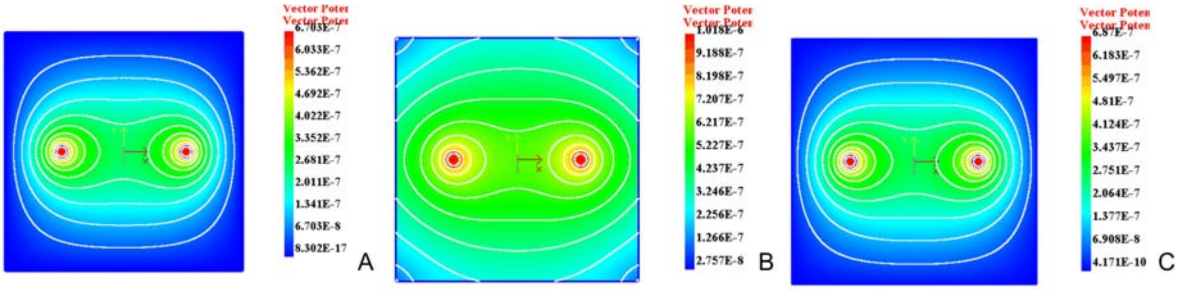

Figure 7-48. Contour plots for magnetic vector potential. A) Homogenous essential boundary conditions, B) asymptotic boundary conditions and C) Decay function infinite element with *L*=0.1.

Figure 7-49 shows the magnetic force per unit length versus the distance between the two wires. The distance *d* was varied from 0.2 m to 1.6m. Within a range from 0.2 m to 0.8 m, the decay factor *L*=0.15 was used for the decay function infinite element method and using this value the computed force using this method were close to the analytical solution. The computed forces using all open boundary techniques are similar when the distance is equal to 0.2 m, 0.4m, or 0.6m; however, the force computation using the asymptotic boundary condition is much closer to the analytic solution as the distance increases, that is when the source approaches the boundary. As the magnetic source (currant carrying wire) is closer to the out boundary, the error in the magnetic force increases when the truncation approach or the infinite element method is used.

Therefore, the force computation using ABC is clearly better than the other two open boundary techniques.

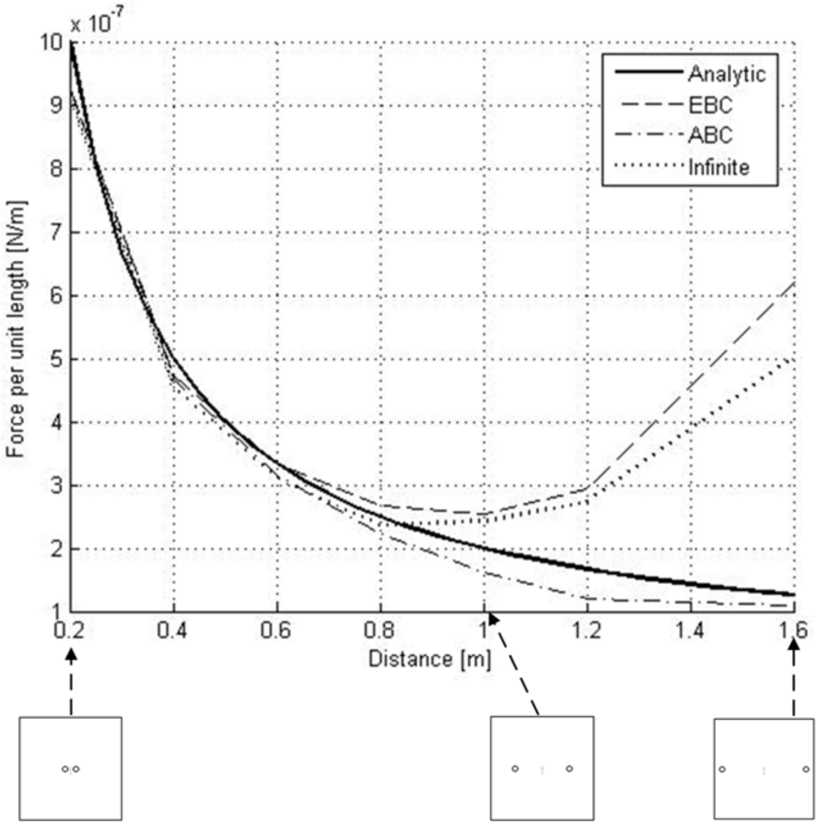

Figure 7-49. The magnetic force versus the distance between two wires

Coupled Magneto-Elastostatic Problems

Two coupled magneto-elastostatic problems are examined to validate the implicit boundary method. The first example is a 2D example containing a clapper solenoid actuator and a cantilever beam. The cantilever beam is attached on the top surface of the clapper armature. The magnetic force from the actuator deforms the cantilever beam. The second example is a 3D plunger solenoid actuator working with one of three circular shaped plates. Even though the geometries of the plates are different and complicated, the density of the structured mesh is the same for all three plates.

Example 7-5-1: 2D Clapper Solenoid Actuator with Cantilever Beam

A cantilever beam is attached on the top surface of the armature. The cantilever beam is a beam fixed at one end. At the other end, this cantilever beam is attached to the armature. The attachment location varies as shown in Figure 7-50. The distances from the center axis to the attached location are 10mm, 20mm, and 28mm. The thickness of the beam is 5mm and the length of the beam is 80mm. The beam is made of aluminum of which material properties are $E = 69\ \mathrm{Gpa}$, $\nu = 0.29$ and $\mu_r = 1$.

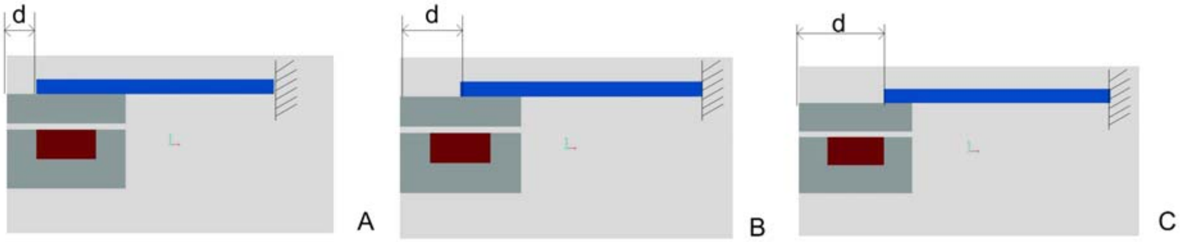

Figure 7-50. Planar clapper solenoid actuator with a cantilever beam. A) d=10mm B) d=20mm and C) d=28mm

This coupled analysis can involve nonlinear properties, nonlinearity that can occur from the large deformation of the beam, changing force according to the gap length, and the contact between the armature and the stator. In this research, the nonlinearity is ignored during the analysis. The computed magnetic force is used as loads for the cantilever beam. Four node bilinear elements are used for the analysis. The total number of elements is 1550. Figure 7-51 shows tip displacement versus ampere-turns. As *NI* increases, the displacement on the tip increases. When d=20mm or 28mm, the displacements on the tip is much larger than when d=10mm; however, there is very small difference in tip deflection between the two cases: d=20mm and d=28mm.

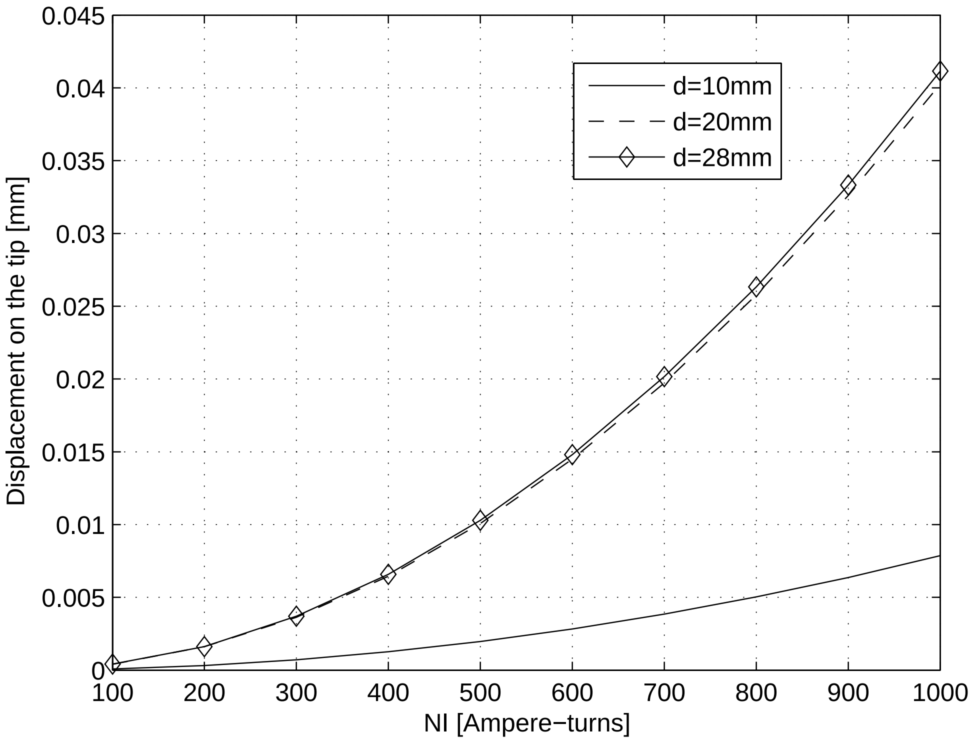

Figure 7-51. Displacement at the tip versus *NI* with varying attachment location

Next, the distance between the symmetric axis and the tip of the cantilever beam is fixed at d=20mm, and the thickness of the bar is varied as shown in Figure 7-52. The thickness value, equal to 3mm, 5mm or 7mm, was used.

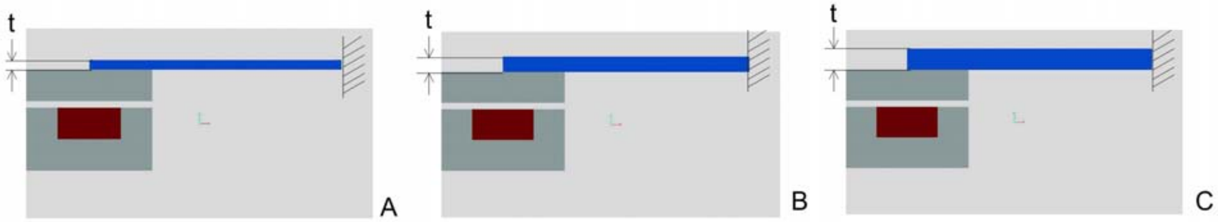

Figure 7-52. Planar clapper solenoid actuator with a cantilever beam. A) t=3mm, B) t=5mm and C) t=7mm

Figure 7-53 shows the tip displacement versus *NI*. When t=3mm, the larger displacement can be observed. When *NI* increases, the difference by the thickness also increases. The tip deflection is very sensitive to the thickness of the cantilever beam.

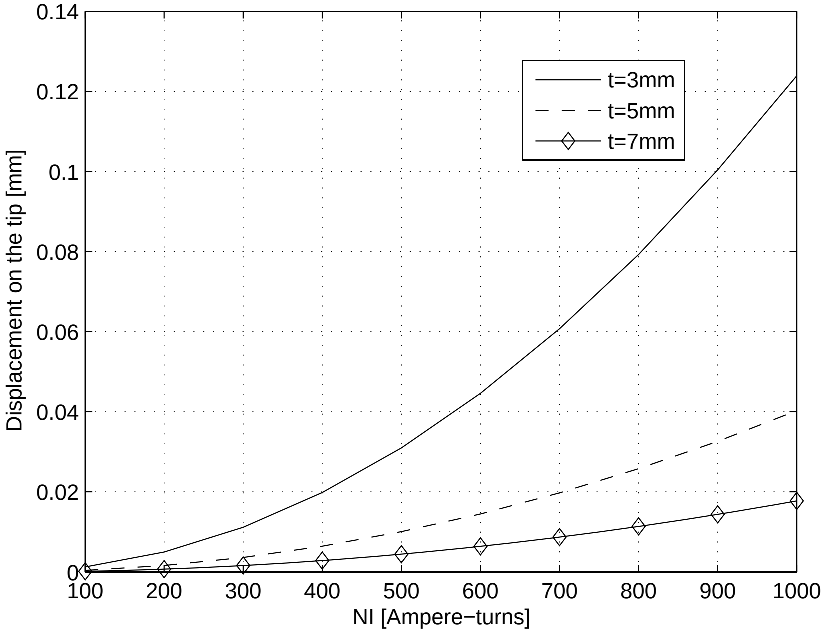

Figure 7-53. Displacement on the tip versus *NI* with varying beam thickness

Example 7-5-2: 3D Plunger Solenoid Actuator with Structures

The 3D model of a plunger solenoid actuator shown in Figure 7-28 A works with one of three plates, one that is attached to the top surface of the plunger armature. The top views of each structure and dimensions are included in the Figure 7-54. The first model is a solid plate, the second is a plate with one hole, and the third one is a plate with two holes. The thicknesses of all the plates equal to 2mm. All of the three structures are attached to the top surface of the plunger armature as shown in Figure 7-55. The structures are made of aluminum.

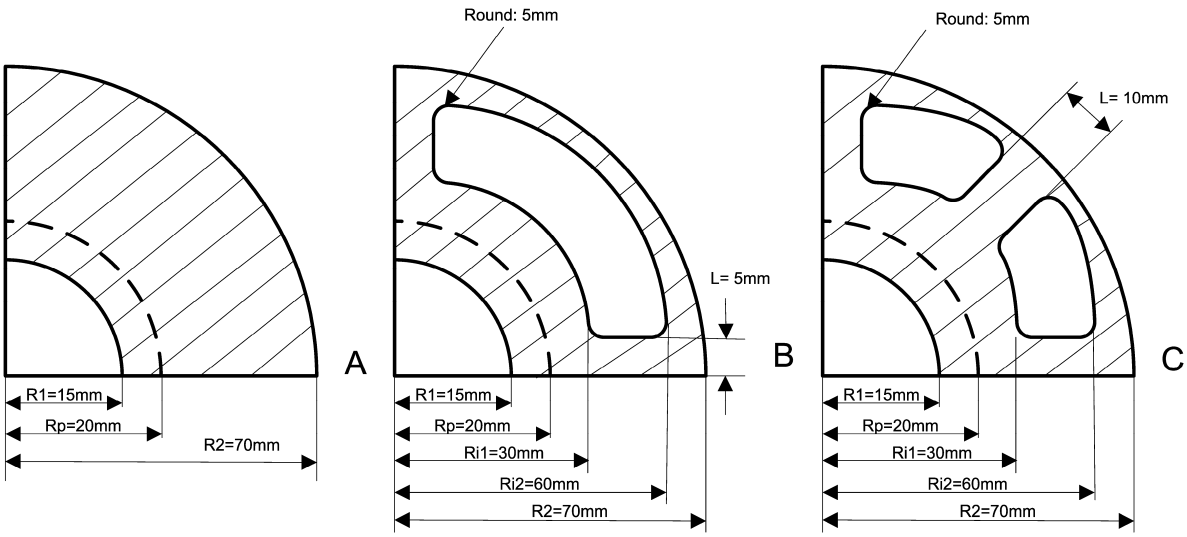

Figure 7-54. Top views of structures attached to the plunger armature. A) Solid plate, B) plate with one hole, and C) plate with two holes

When *NI*=800 and the fixed boundary conditions are applied on the surfaces of the structure at R=70mm, the magnetic force from the actuator results in downward deflection of the plunger armature. The structures are deformed by the movement of the armature as shown in Figure 7-56.

The maximum displacements for the structures are $7.24\times10^{-7}\,mm$ in the solid plate, $1.086\times10^{-6}\,mm$ in the plate with one hole, and $8.539\times10^{-7}\,mm$ in the plate including two holes. Figure 7-57 shows the maximum displacement versus *NI* (ampere-turns) for each plate. Among the structures, the plate with one hole has the largest deformation. On the other hand, the solid plate has the highest stiffness among them.

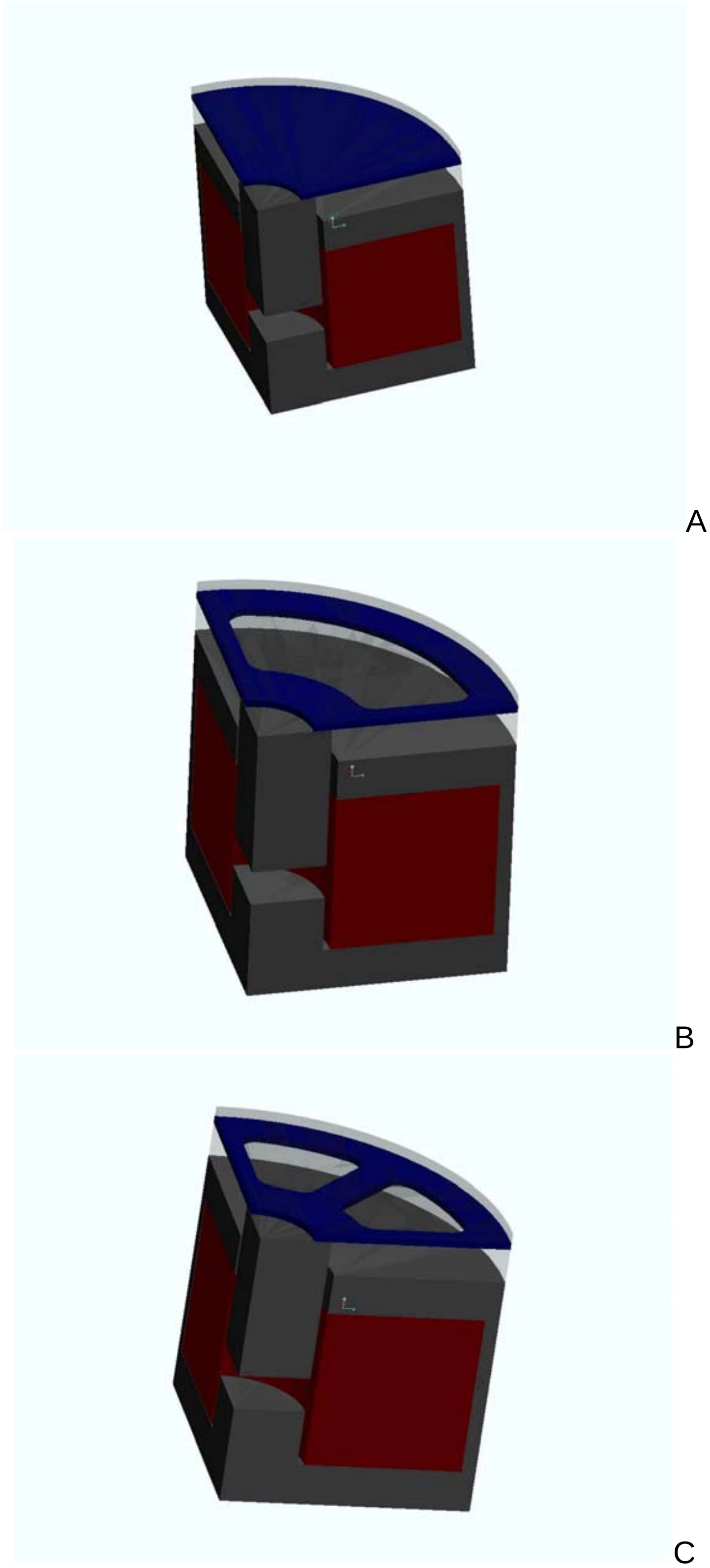

Figure 7-55. 3D plunger solenoid actuators with A) Solid plate, B) plate with one hole, and C) plate with two holes

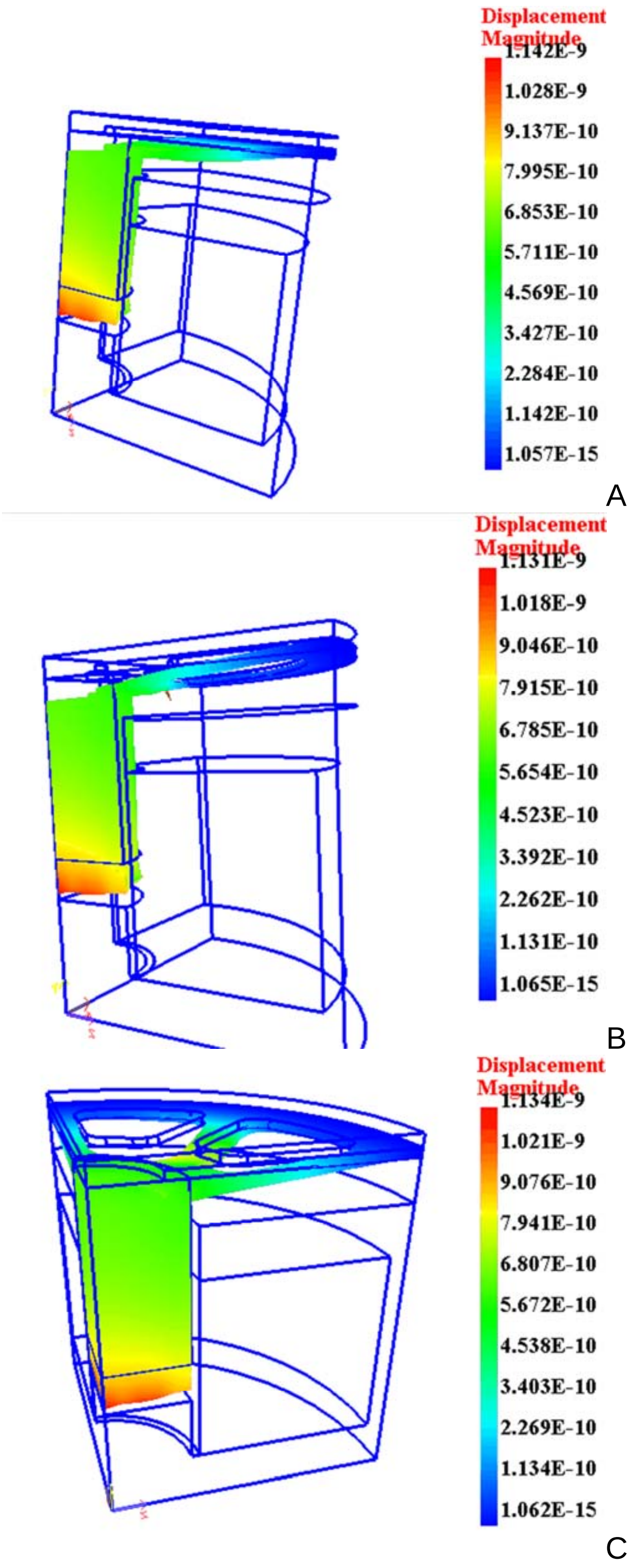

Figure 7-56. Deformation due to magnetic force. A) Solid plate, B) plate with one hole, and C) plate with two holes

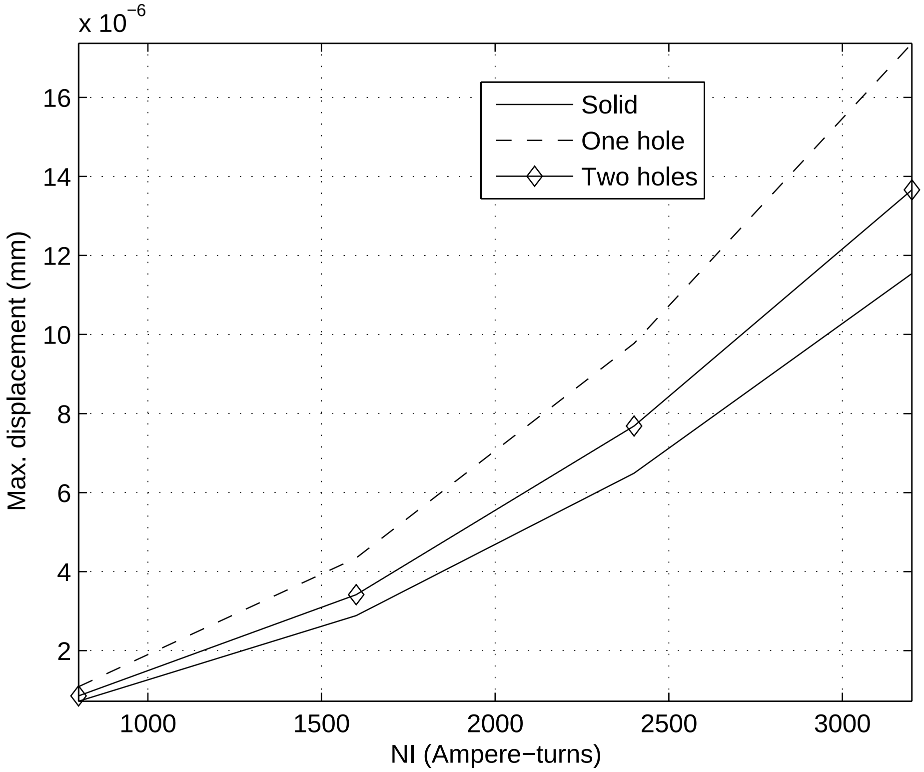

Figure 7-57. Maximum displacement versus *NI*

CHAPTER 8
DESIGN AND ANALYSIS OF MAGNETIC ACTUATORS USING IBFEM

Design Criteria

In this chapter, IBFEM is used as an actuator design tool. Solenoid actuators with clapper armature or plunger armature and coil actuators are designed under given design criteria. Among them, a lighter and more efficient design are needed for flapping wing micro air vehicle. The micro air vehicles are significantly small size aerial vehicle with the maximum dimension of about 15 cm. For a micro air vehicle actuator, there are three given design criteria: coil winding area, iron weight and size.

The given coil winding area S_w is assumed to be $12mm^2$. The entire coil winding area cannot be assumed to be only the copper because the coil includes copper and other materials such as insulator. Thus, the relation between the coil winding area and the copper conductor is defined as the packing factor F_p [18]. When the coil is wound tightly, the packing factor can be up to 75%. Thus, the packing factor is assumed to be 70%. The area of the coil wire is $S_c = 5.01\times10^{-3} mm^2$ when the number of the American Wire Gauge (AWG) is 40. Therefore, the number of coil turns *N* is given as following equation

$$N = \frac{F_p S_w}{S_c} = 1680 \tag{8-1}$$

When the coil is wound to a cylindrical bobbin with the diameter of 4 mm, the total length of the coil becomes about 21.1 m. As the resistance per meter for the given AWG is $3.44\ \Omega/m$, the total resistance of the coil is approximately $72\ \Omega$. In this research, it is assumed that the coil wire can allow current of 100mA to flow. The allowable current of the wire is based on plastic insulation. In case of the current source, LT3092, manufactured by Linear technology, the maximum output current is 200mA. The input voltage range is from 1.2 V to 40 V so that LT3092 can be operated by using a small size battery. Thus, the current of 100mA can be obtained using LT3092. If *N*=1680 and the amount of current *I* can be controlled by a digital processor, *NI* (ampere-turns) can vary from 0 to 168. *NI* is also called magnetomotive force. In order to compare several designed actuators in the later section, the magnetomotive force, *NI*=30, is used. When the maximum current (100mA) flows in the coils, the coils can have maximum energy dissipation as $W = I^2 R = 0.72\ [\mathbf{W}]$.

Another design criterion is the iron weight of the actuator. The iron occupy large portion of the weight of the actuator; however, iron has high relative permeability so that usage of the iron material can intensify a magnetic force of the actuator. Therefore, there is a trade-off between the iron weight of the actuator and the usage of the iron. As the second design criterion, we assume that the total iron weight of the iron portion can be up to 10g. In order to compute the iron weight of an actuator design, the mass density of iron is used as $7874 kg/m^3 = 7.874 \times 10^{-3} g/mm^3$. The third design criterion is the size of the actuator. In order to install an actuator inside the micro air vehicle, the actuator should fit inside of a cube with edge length of 2cm.

In the beginning of a solenoid design, the reluctance method is used so that a simple design is created under the design criteria. Based on the initial design, geometry of the design is changed in order to determine a better design.

Solenoid Actuators with Clapper Armature

A solenoid actuator with a clapper armature is shown in Figure 8-1. The clapper armature can move in the y-direction when the coils carry current. The armature and the stator are made of thin steel laminations with relative permeability of 2000, a thin steel lamination that can reduce heating caused by eddy current. When the current flows through a coil, magnetic flux is created as shown in Figure 8-1. The magnetic flux follows a closed path. If magnitude of the magnetic flux is known, a magnetic force can be estimated using the Maxwell stress tensor method.

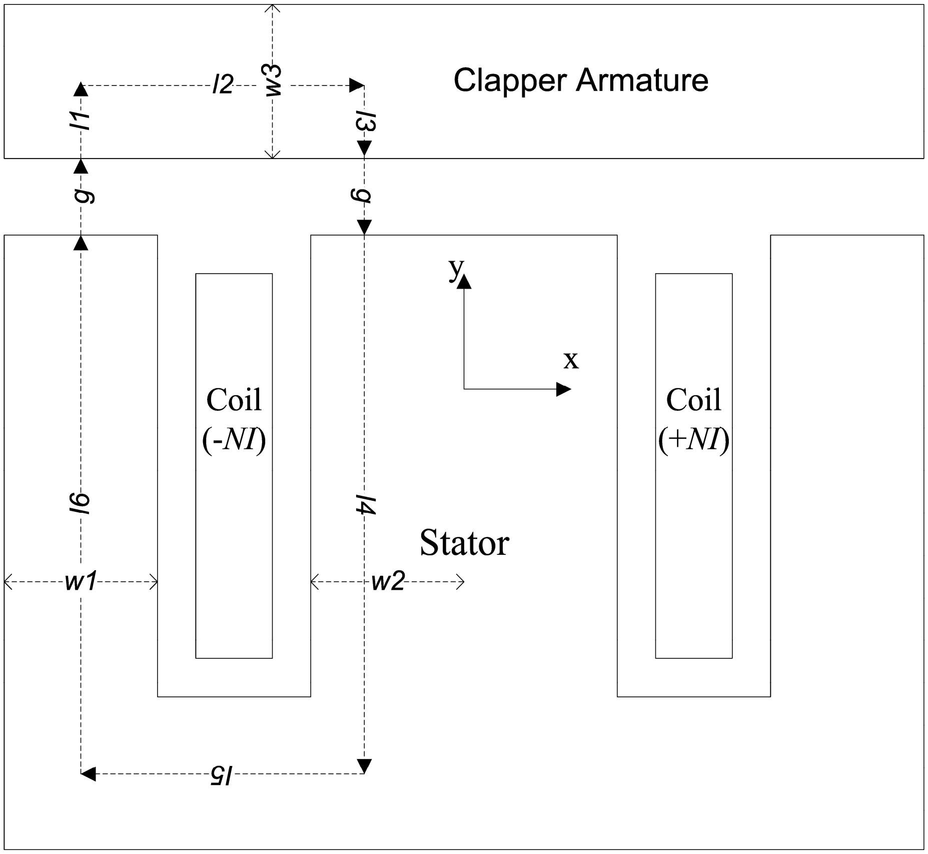

Figure 8-1. Solenoid actuator with clapper armature

Supposing that the dimensions are $l1 = l3 = 0.5mm$, $l2 = l5 = 3mm$, $l4 = l6 = 6.5mm$, $g = 1mm$, and $w1 = w2 = w3 = 1mm$, then reluctances in the armature, the stator, and the gap can be obtained as follows

$$R_{armature} = \frac{l1 + l2 + l3}{w1 \times \mu_r \mu_0} = 1.592 \times 10^3 \left[\mathrm{A/Wb}\right] \tag{8-2}$$

$$R_{stator} = \frac{l4 + l5 + l6}{w1 \times \mu_r \mu_0} = 6.364 \times 10^3 \left[\text{A/Wb}\right] \tag{8-3}$$

$$R_{gap} = \frac{2g}{w1 \times \mu_0} = 1.591 \times 10^6 \left[\text{A/Wb}\right] \tag{8-4}$$

Using the reluctance method, the magnetic flux can be stated as

$$\phi = \frac{NI}{\sum_i R_i} = \frac{NI}{R_{armature} + R_{stator} + R_{gap}} = 6.285 \times 10^{-7} \times NI \left[\text{Wb}\right] \tag{8-5}$$

As the magnetic flux is constant on the given path, the magnetic flux density and the magnetic field density can be obtained in each airgap as follows

$$B_{gap} = \frac{\phi}{w1} = 6.285 \times 10^{-4} \times NI \left[\text{T}\right] \tag{8-6}$$

$$H_{gap} = \frac{1}{\mu_0} B_{gap} = 500 \times NI \left[\text{A/m}\right] \tag{8-7}$$

Using Maxwell's stress tensor method, the normal magnetic pressure can be obtained as

$$F = \frac{\mu_0}{2} \left(H_{gap}\right)^2 \left(4 \times w1\right) = 6.283 \times 10^{-4} \times \left(NI\right)^2 \left[\text{N}\right] \tag{8-8}$$

When $NI = 30$, the magnetic force per unit length becomes 0.565 N/m. The magnetic flux and the magnetic field density are $1.886 \times 10^{-2} \left[\text{T}\right]$ and $1.5 \times 10^4 \left[\text{A/m}\right]$. Using the same geometry of the actuator, Figure 8-2 A shows contour plot of magnetic vector potential computed using IBFEM. Figure 8-2 B shows magnetic field density in the y-direction. The computed magnetic field density in the gap is approximately equal to the analytical value of $1.5 \times 10^4 \left[\text{A/m}\right]$. For this analysis, the asymptotic boundary conditions are applied on the outer boundaries. The computed force is 0.633 N/m. The computed force and the analytical solution are quite close. The difference between them results from a fringing flux, which the reluctance method ignores. As the iron domain is $40mm^2$, the iron weight per unit depth is $0.315 g/mm$.

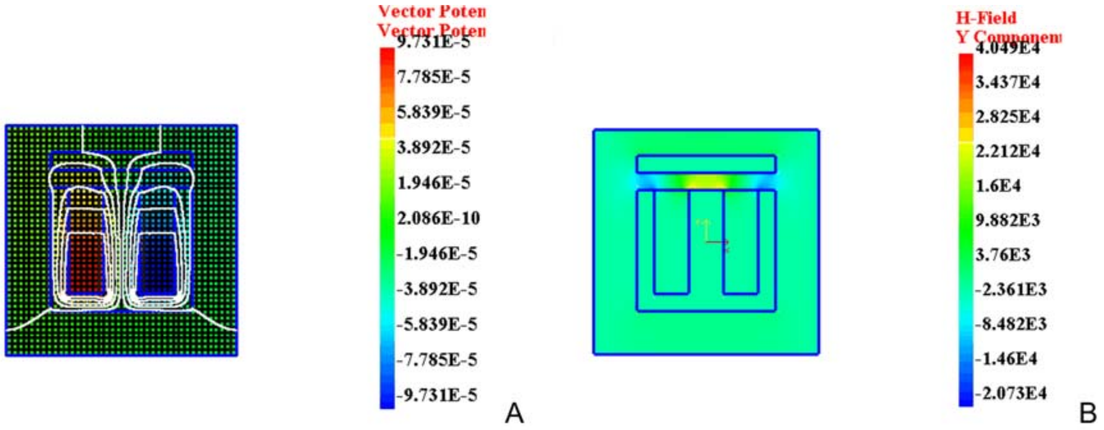

Figure 8-2. IBFEM results. A) Contour plot of magnetic vector potential, and B) Magnetic field density

Based on the initial design in shown in Figure 8-1, three different designs are created by changing the geometry of the armature and the stator. For all the designs, the rectangular area of the 2D model, including the air domain, is $13\times 13mm^2$. Figure 8-3 shows three designs with dimensions. The dimensions shown are all in *mm*. Even though the geometry is changed for each actuator, the mesh densities of the structured mesh are same for all designs. Nine node B-spline elements were used for the analysis. The total number of nodes was 2586. The asymptotic boundary conditions were applied on the outer boundaries. The magnetomotive force, $NI = 30$, was applied.

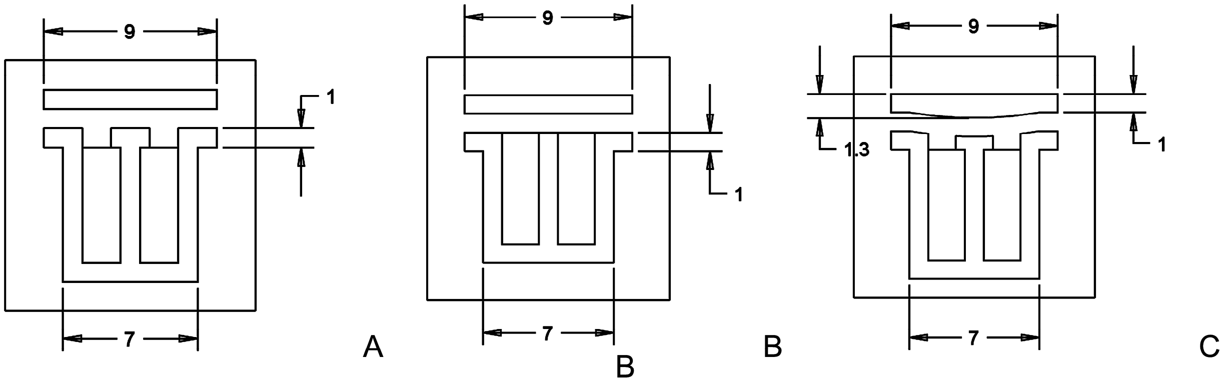

Figure 8-3. Clapper solenoid actuators. A) Design 1, B) Design 2, and C) Design 3

Figure 8-4 shows contour plots of magnetic vector potentials for all designs. Based on those computations, Table 8-1 shows comparison for three designs in terms of the magnetic force and the iron weight.

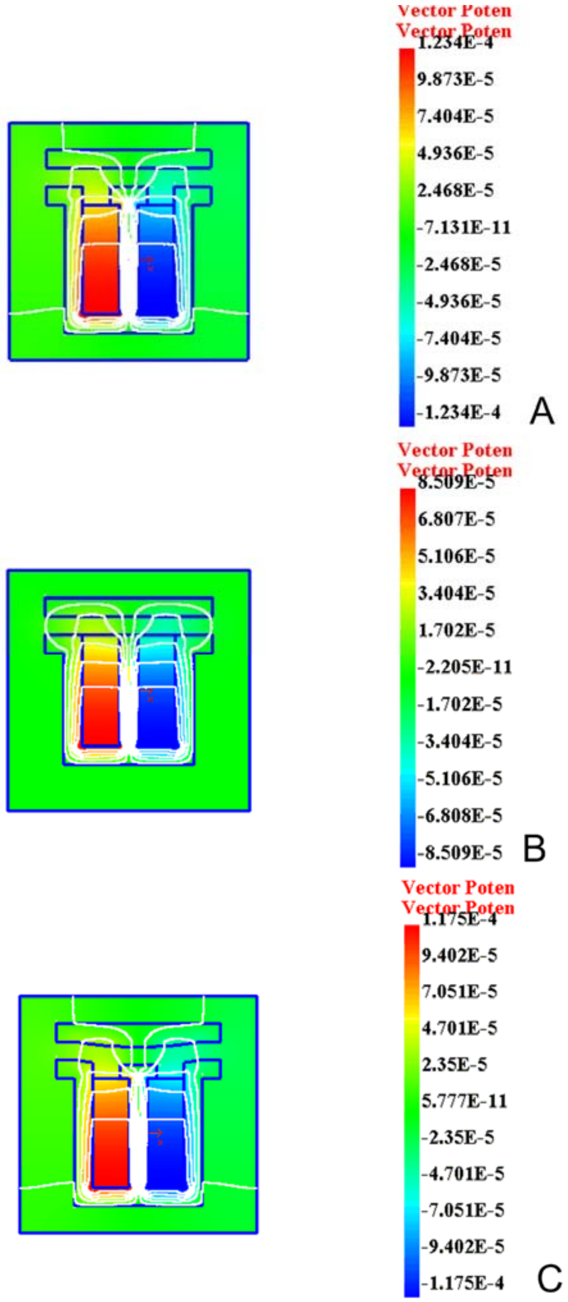

Figure 8-4. Contour plots of magnetic vector potential for clapper solenoid actuators. A) Design 1, B) Design 2, and C) Design 3

Table 8-1. Comparison for three clapper solenoid actuators (*NI*=30)

	Design 1	Design 2	Design 3
Force per *m*	0.691 *N/m*	0.509 *N/m*	0.681 *N/mm*
Iron weight per *mm*	$0.315g/mm$	$0.283g/mm$	$0.320g/mm$

According to Table 8-1, the first actuator design produces the largest force among them. The second actuator is the lightest one.

Solenoid Actuators with Plunger Armature

A solenoid actuator with a plunger armature is shown in Figure 8-5. The shape of the plunger armature can be a brick, cylinder, or conics. There are two gaps of *g* and *gs* that the flux can enter and leave the plunger armature. Useful magnetic force is produced only at *g*.

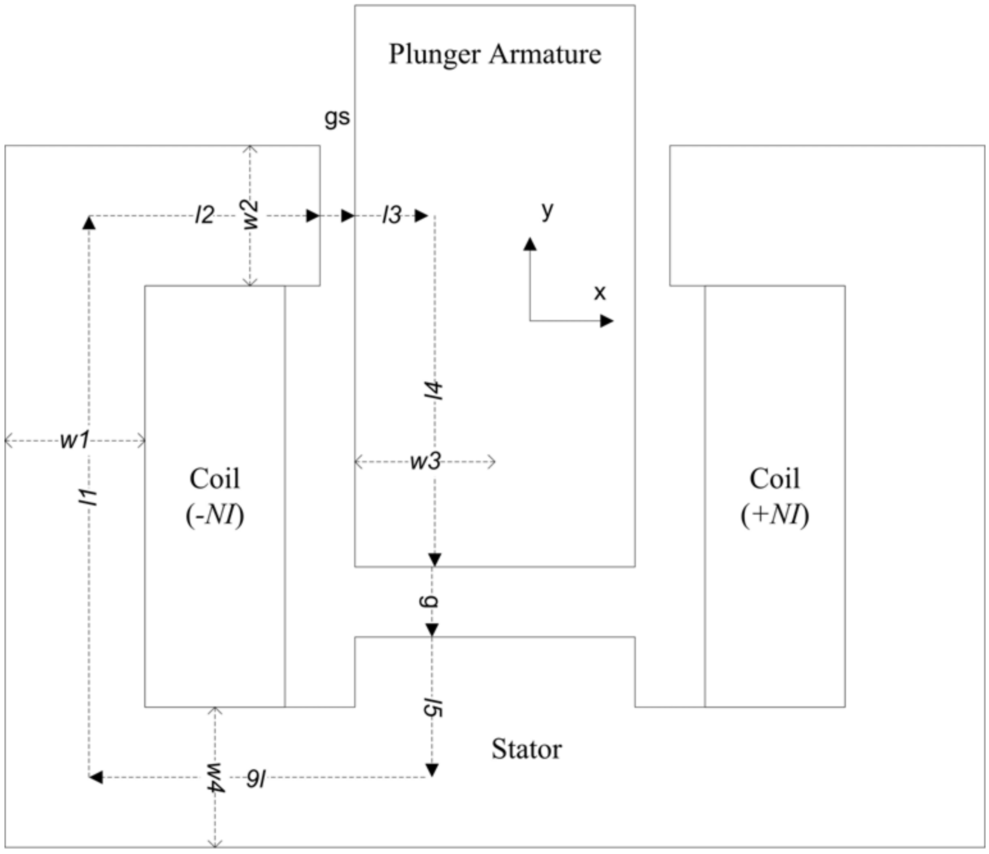

Figure 8-5. Solenoid actuator with plunger armature

The armature and the stator are made of steel with the relative permeability of 2000. When the dimensions are $l1 = 7mm$, $l2 = 2.5mm$, $l3 = 0.9mm$, $l4 = 4.5mm$, $l5 = 1.5mm$, $l6 = 3.5mm$, $gs = 0.1mm$, $g = 1mm$ and $w1 = w2 = w3 = w4 = 1mm$, all reluctances can be calculated as follows

$$R_{armature} = \frac{l3 + l4}{w1 \times \mu_r \mu_0} = 2.148 \times 10^3 \left[\mathrm{A/Wb}\right] \tag{8-9}$$

$$R_{stator} = \frac{l1 + l2 + l5 + l6}{w1 \times \mu_r \mu_0} = 5.769 \times 10^3 \left[\mathrm{A/Wb}\right] \tag{8-10}$$

$$R_{gs} = \frac{gs}{w1 \times \mu_0} = 7.958 \times 10^4 \left[\mathrm{A/Wb}\right] \tag{8-11}$$

$$R_g = \frac{g}{w1 \times \mu_0} = 7.958 \times 10^5 \left[\mathrm{A/Wb}\right] \tag{8-12}$$

Using the reluctance method, the magnetic flux is

$$\phi = \frac{NI}{\sum_i R_i} = \frac{NI}{R_{armature} + R_{stator} + R_g + R_{gs}} = 1.132 \times 10^{-6} \times NI \left[\mathrm{Wb}\right] \tag{8-13}$$

Based on the magnetic flux, the magnetic flux density and the magnetic field density in each airgap can be computed as follow

$$B_{gap} = \frac{\phi}{w1} = 1.132 \times 10^{-3} \times NI \left[\mathrm{T}\right] \tag{8-14}$$

$$H_{gap} = \frac{1}{\mu_0} B_{gap} = 900.8 \times NI \left[\mathrm{A/m}\right] \tag{8-15}$$

Using the magnetic field in the gap, the useful magnetic force can be calculated as follow

$$F = \frac{\mu_0}{2} \left(H_{gap}\right)^2 \left(2 \times w1\right) = 1.02 \times 10^{-3} \times \left(NI\right)^2 \left[\mathrm{N}\right] \tag{8-16}$$

when $NI = 30$, the force becomes 0.918 N. The magnetic flux and the magnetic field density are $3.4 \times 10^{-2} \left[\mathrm{T}\right]$ and $2.702 \times 10^4 \left[\mathrm{A/m}\right]$. Figure 8-6 shows the computed results: contour plot of magnetic vector potential and magnetic field density in the y-direction.

For the analysis, the same mesh density was used in the clapper solenoid actuator model. Nine node B-spline elements were used. Asymptotic boundary conditions were applied on the outer boundaries. The computed total force on the plunger armature is 0.9130 N/m. As the total area of the iron is $38.8mm^2$, the iron weight per unit depth is $0.306g/mm$.

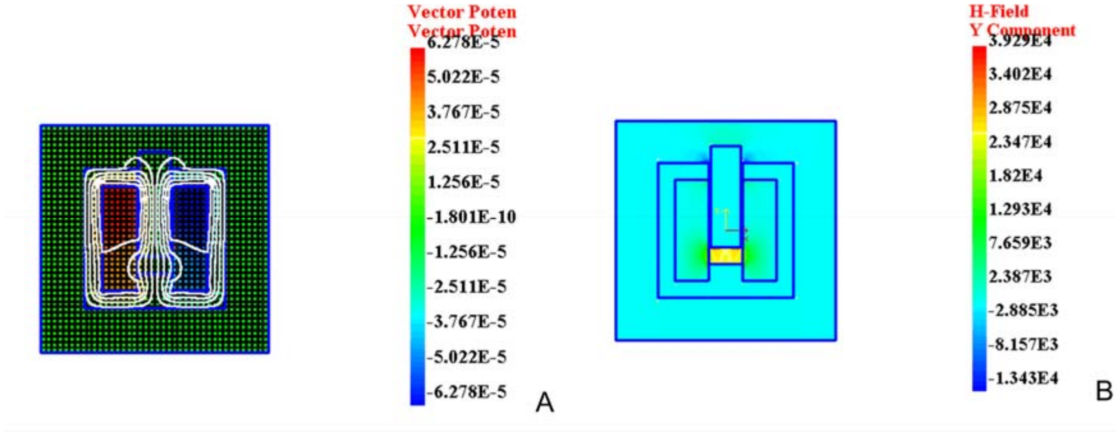

Figure 8-6. IBFEM results. A) Contour plot of magnetic vector potential, and B) Magnetic field in the y-direction

Modifying the initial design in shown in Figure 8-5, three different designs are created as shown in Figure 8-7. The dimensions shown are all in *mm*. For all designs, the area of the 2D model is as same as one of the clapper solenoid actuator. The same mesh density is applied for all the designs. Nine node B-spline elements were used for the analysis. The total number of nodes was 2548. The asymptotic boundary conditions were applied on the outer boundaries. The magnetomotive force, $NI = 30$, was used.

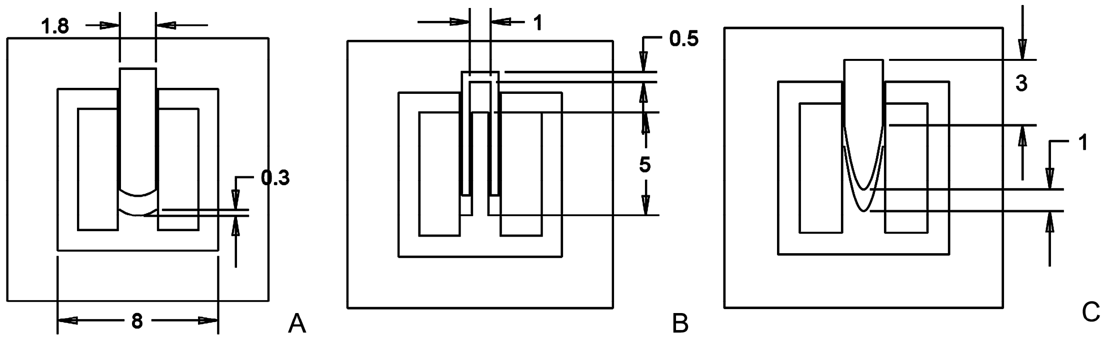

Figure 8-7. Plunger solenoid actuators. A) Design 1, B) Design 2, and C) Design 3

Figure 8-8 shows contour plots of magnetic vector potentials for all designs. Based on those results, Table 8-2 shows comparison for three designs in terms of the magnetic force and the iron weight. According to Table 8-2, the third plunger solenoid actuator model can produce the largest force among them. The second actuator model is the lightest one.

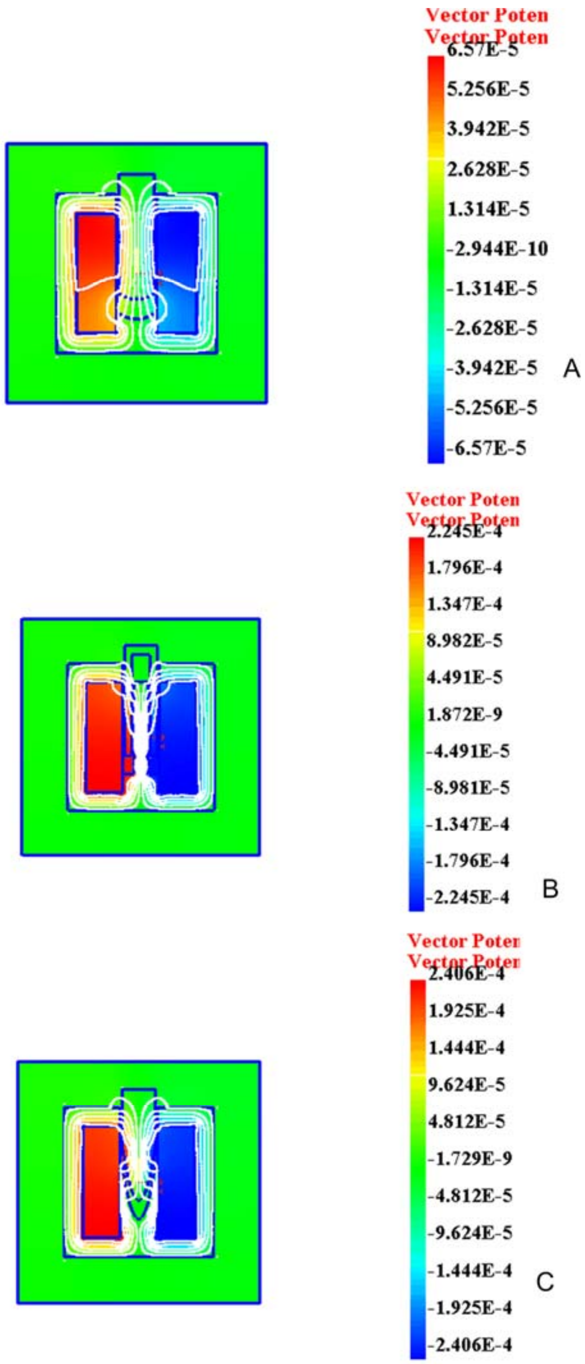

Figure 8-8. Contour plots of magnetic vector potential for plunger solenoid actuators. A) Design 1, B) Design 2, and C) Design 3.

Table 8-2. Comparison for three plunger solenoid actuators (*NI*=30)

	Design 1	Design 2	Design 3
Force per *m*	1.154 *N/m*	0.262 *N/m*	2.801 *N/mm*
Iron weight per *mm*	$0.306g/mm$	$0.294g/mm$	$0.310g/mm$

Solenoid Actuators with a Combined Plunger & Clapper Armature

A combined plunger & clapper armature is an armature that includes a clapper & plunger to increase the force. Three designs were studied. The sizes of those actuators are similar to one of the clapper solenoid actuator in the previous section. Magnetic force and iron weight for each actuator are characterized.

Figure 8-9 shows three solenoid actuators with a mixture armature. The dimensions shown are all in *mm*. For all designs, the area of the 2D model is as same as one of the clapper solenoid actuator. For the analysis, the same mesh density is applied for all the designs. Nine node B-spline elements were used for the analysis. The total number of nodes was 2674. The asymptotic boundary conditions were applied on the outer boundaries. The magnetomotive force *NI* is equal to 30.

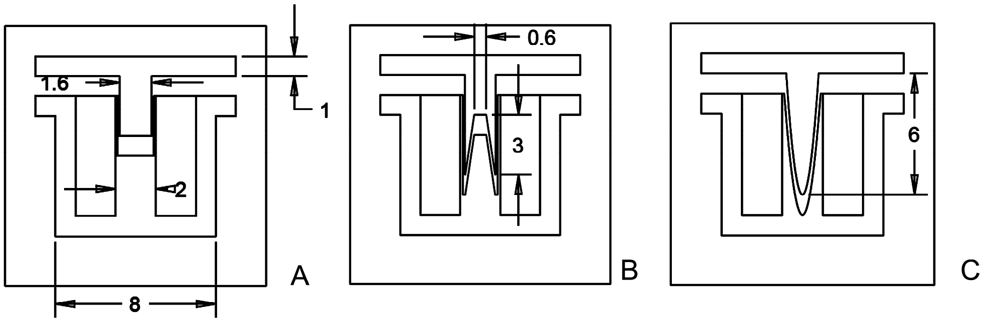

Figure 8-9. Three combined plunger & clapper solenoid actuators. A) Design 1, B) Design 2, and C) Design 3

After the analysis using these models, contour plots of magnetic vector potentials are show in Figure 8-10. Based on those results, Table 8-3 shows comparison for three designs in terms of the magnetic force and the iron weight. According to Table 8-3, the third one can produce the largest force among them. The second actuator is the lightest one.

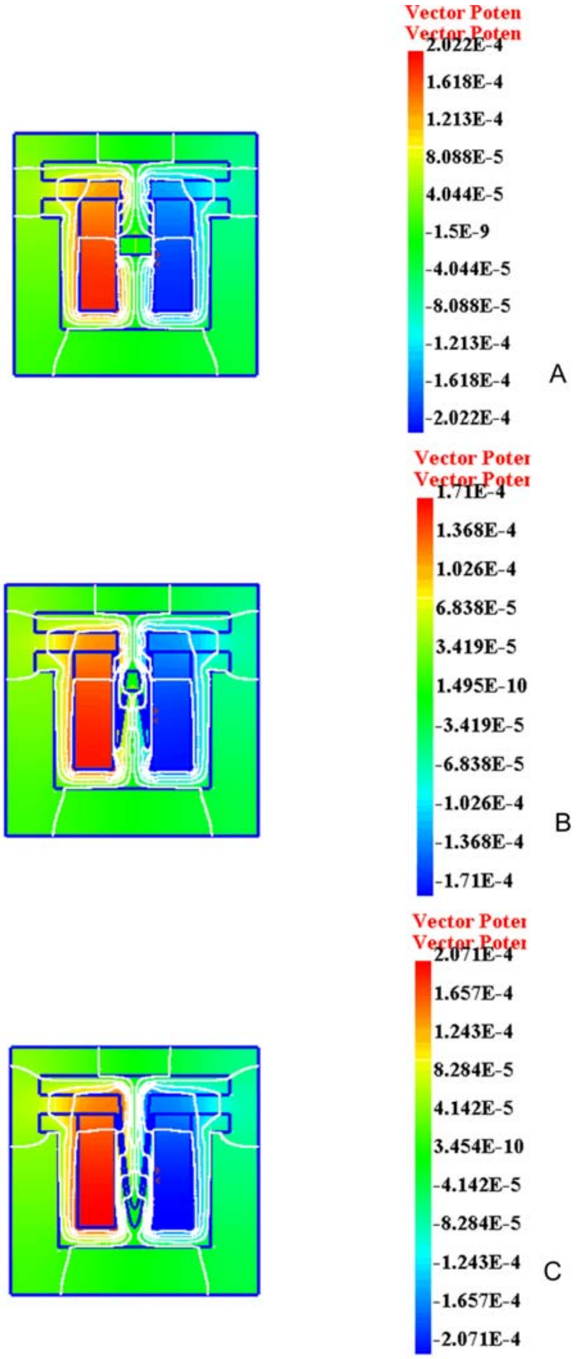

Figure 8-10. Contour plots of magnetic vector potential for combined plunger & clapper solenoid actuators. A) Design 1, B) Design 2, and C) Design 3.

Table 8-3. Comparison for three combined plunger & clapper solenoid actuators (*NI*=30)

	Design 1	Design 2	Design 3
Magnetic force per *m*	0.961 *N/m*	0.413 *N/m*	1.30 *N/m*
Iron weight per *mm*	$0.342 g/mm$	$0.339 g/mm$	$0.340 g/mm$

Coil Actuators

In this section, three coil actuators are studied under the given design criteria. The coil actuators include permanent magnets so that higher magnetic flux can be produced without the increase of *NI.* Moreover, the usage of the permanent magnets can reduce heating on the actuator. The coil actuator has magnetic force in the conductive coil instead of one on the armature of the solenoid actuator, a magnetic force that is computed using the Lorentz force equation.

Figure 8-11 shows three coil actuators. The dimensions shown are all in *mm*. For all the designs, the rectangular area of the 2D model including the air domain is $18 \times 18 mm^2$. The coil winding area is the same as in previous solenoid actuators. Two permanent magnets have different direction with the same remanent flux of 0.8 T. The first design is based on a typical voice coil actuator in a loudspeaker. The second is a design to remove the iron laminates from the first design. The third design has a gap at the bottom portion of the iron laminate, which allows the coil to move freely in the downward direction. For the analysis, the same mesh density is applied for all designs. Four node bilinear elements were used. The total number of nodes was 12036. The asymptotic boundary conditions were applied on the outer boundaries. *NI* is equal to 30.

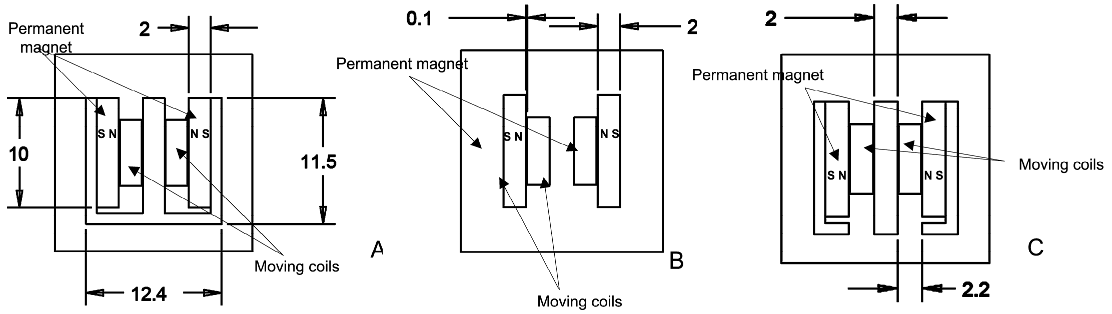

Figure 8-11. Three coil actuators. A) Design 1, B) Design 2, and C) Design 3

After the analysis using these models, the magnitudes of the magnetic flux densities are show in Figure 8-12. As the Lorentz force is proportional to the magnetic flux density, a stronger magnetic flux density near the moving coils can create a larger force. The first design has the strongest magnetic flux near the moving coils. Based on those results, Table 8-3 shows comparison for three designs in terms of the Lorentz force on the moving coil and the iron weight of the actuator. According to Table 8-4, the first coil actuator can produce the largest force among them. The second design is the best design if the actuator weight is the most critical criterion.

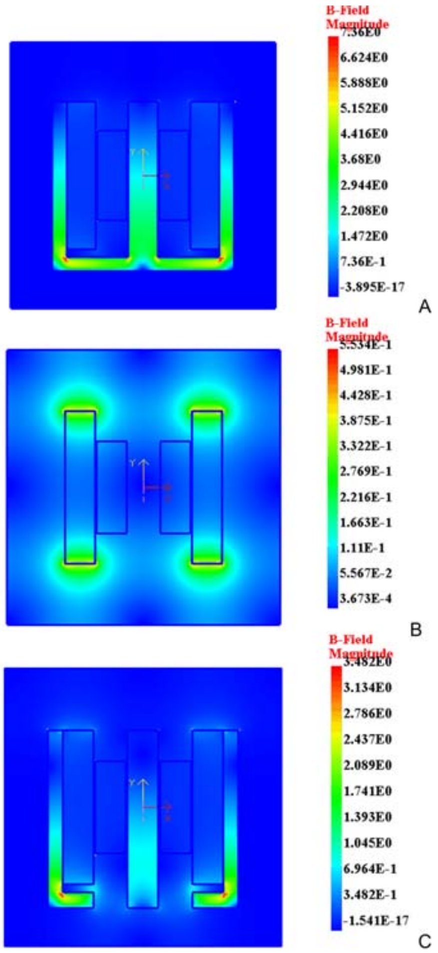

Figure 8-12. Magnitude of B fields for three coil actuators. A) Design 1, B) Design 2, and C) Design 3.

Table 8-4. Comparison for coil actuators (*NI*=30)

	Design 1	Design 2	Design 3
Force per *m*	21.0 *N/m*	2.64 *N/m*	9.12 *N/m*
Iron weight per *mm*	$0.428 g/mm$	$0\ g/mm$	$0.394 g/mm$

The Best Actuator among the Designed Actuators

Using IBFEM, four types of actuators were examined such as the clapper solenoid actuator, the plunger solenoid actuator, the combined plunger & clapper solenoid actuator, and the coil actuator. Among them, the coil actuator is the best actuator considering the given design criteria. Among several designs for the coil actuators, the first design is used for flapping wings of the micro air vehicle as shown in Figure 8-13. The first design could generate the largest force under the given magnetomotive force so that the magnetic force can make the largest deformation of flapping wings among them.

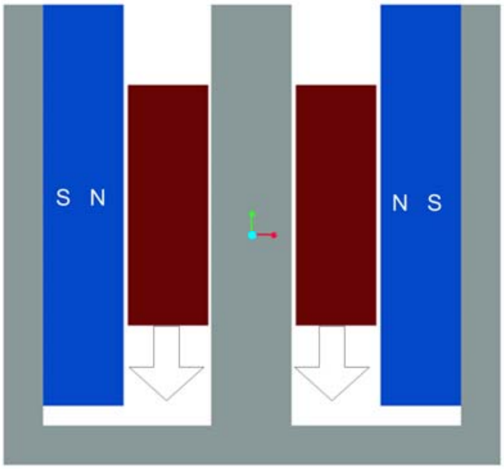

Figure 8-13. The best magnetic actuator among several designed actuators

Considering the 2D model, the best coil actuator is designed as 3D solid model as shown in Figure 8-14. Considering the symmetry, one fourth of the model is created using commercial software, Pro/engineering. Figure 8-15 shows the dimension of the

3D coil actuator and the directions of the permanent magnets. The dimensions shown are all in *mm*.

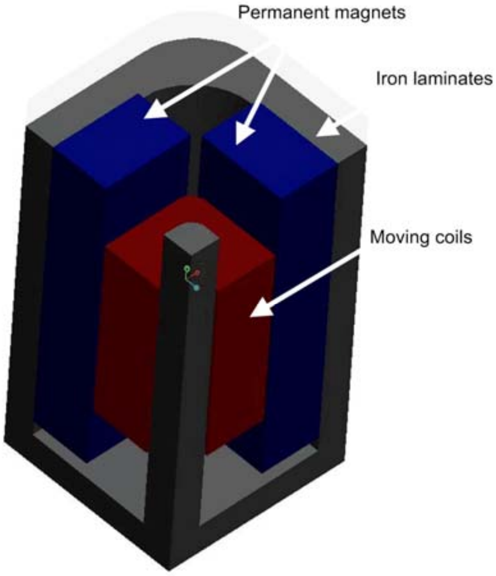

Figure 8-14. Sold model of the 3D coil actuator

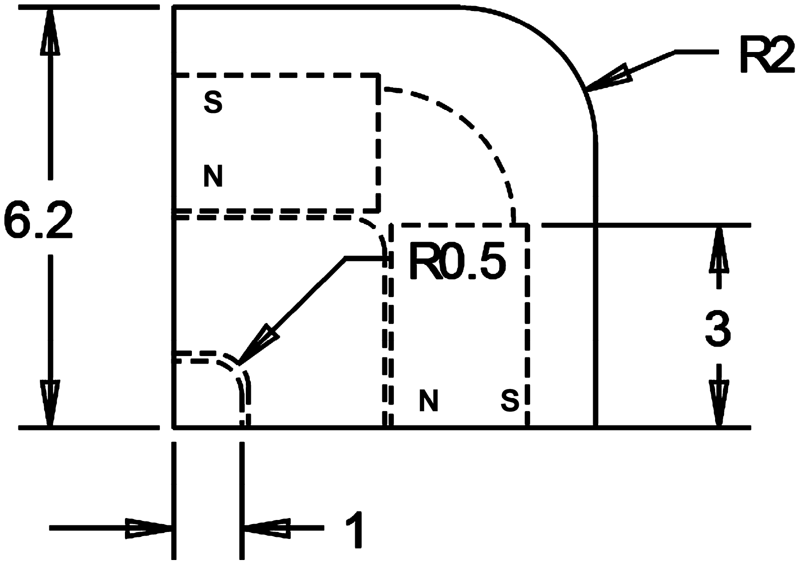

Figure 8-15. The top view of the 3D coil actuator

The moving coils carry current. The coil has a conductivity value of $10^6\ \mathrm{S/m}$. In order to perform the analysis, eight node brick elements were used. The total number of the nodes was 9651. According to the design criterion, the magnetomotive force, *NI*, can vary from 0 to 168. When *NI* is equal to 30, the magnetic flux density of the coil actuator is shown in Figure 8-16.

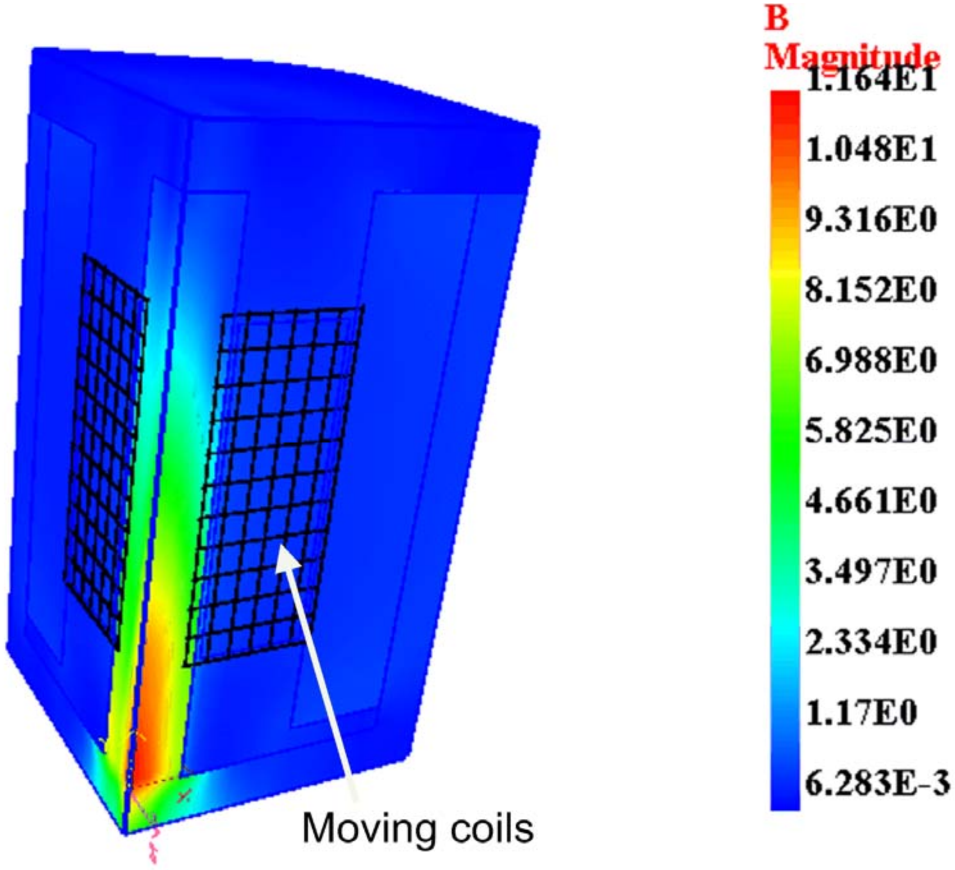

Figure 8-16. The magnitude of the magnetic flux density of the coil actuator

The magnetic flux density, B, vary from 1.17 to 2.33 *T* nearby the moving coils, so the computed force is -0.114 *N.* When *NI* is equal to 10, 30, 60, 90, 120 or 168, the computed Lorentz force is shown in Figure 8-17. Figure 8-17 shows the linear relation between the magnetomotive force and the Lorentz force. The maximum force is 0.683 *N.*

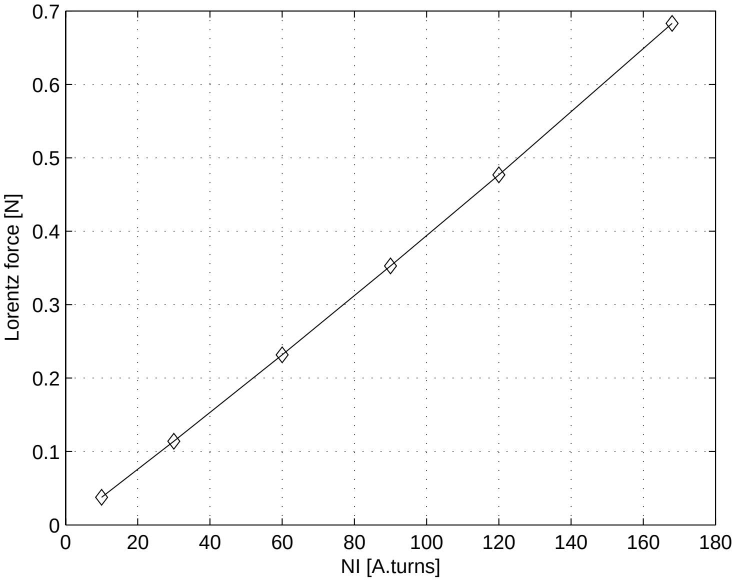

Figure 8-17. Lorentz force of the coil actuator versus *NI*

Coupled Magneto-Elastostatic Problems with a Flapping Wing Model

The best coil actuator is embedded in a micro air vehicle with flapping wings as shown in Figure 8-18. The coil actuator can fit inside of the fuselage. The moving coil of the coil actuator is attached to the structure.

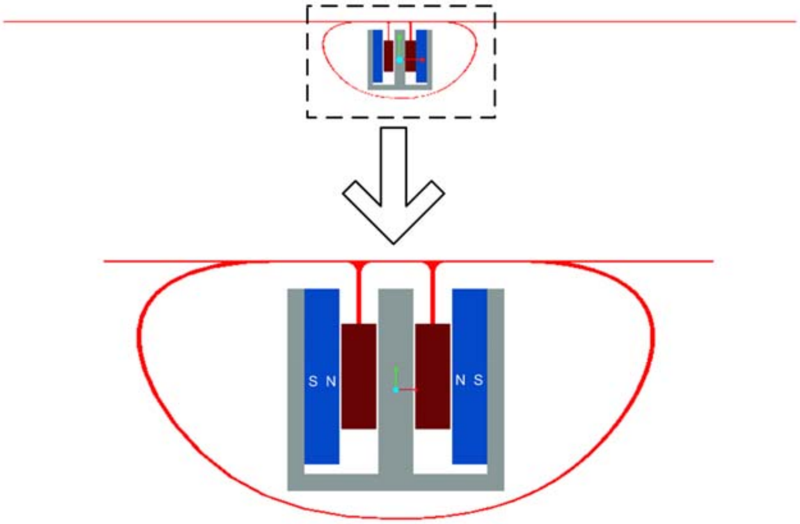

Figure 8-18. The coil actuator with flapping wings

Four structures are designed as shown in Figure 8-19 structures that are created as surface models. The thickness of the structure assumed to be equal to 0.45mm. Additionally, it is assumed that the structure is made of aluminum. All the structures have a similar top view; however, they have different front and side views. The dimensions shown are all in mm. As the length in chordwise direction is 26 mm, two coil actuators can be placed along the chordwise direction because the length of the coil actuator is 12.2mm according to Figure 8-15. Figure 8-20 also shows the four surface models.

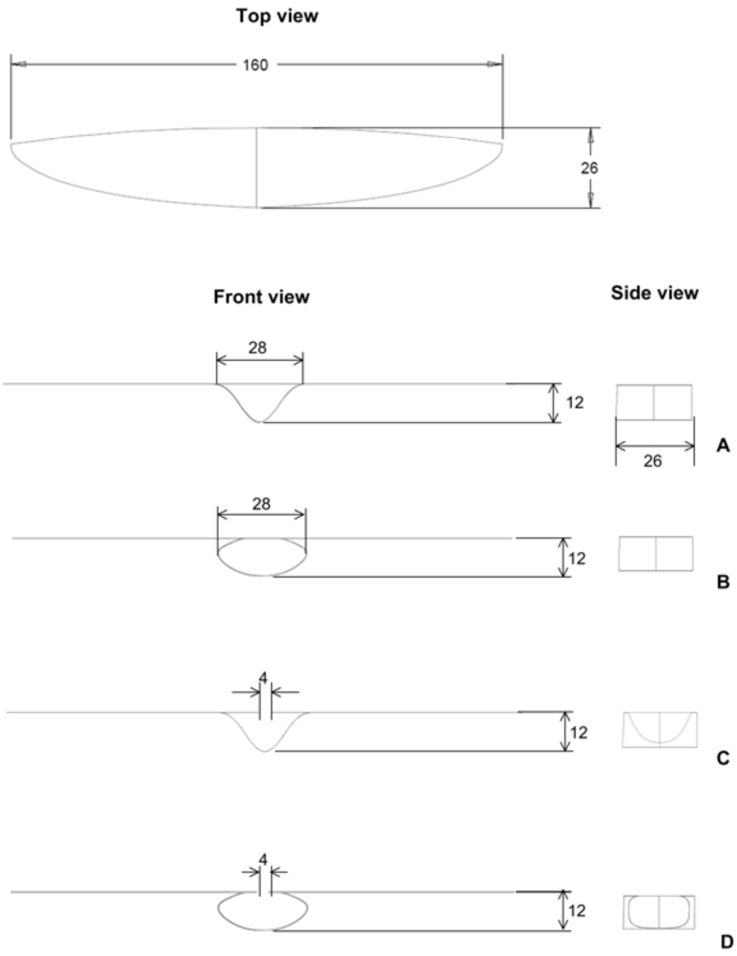

Figure 8-19. Four structures with flapping wings. A) Design 1, B) Design 2, C) Design 3, and D) Design 4.

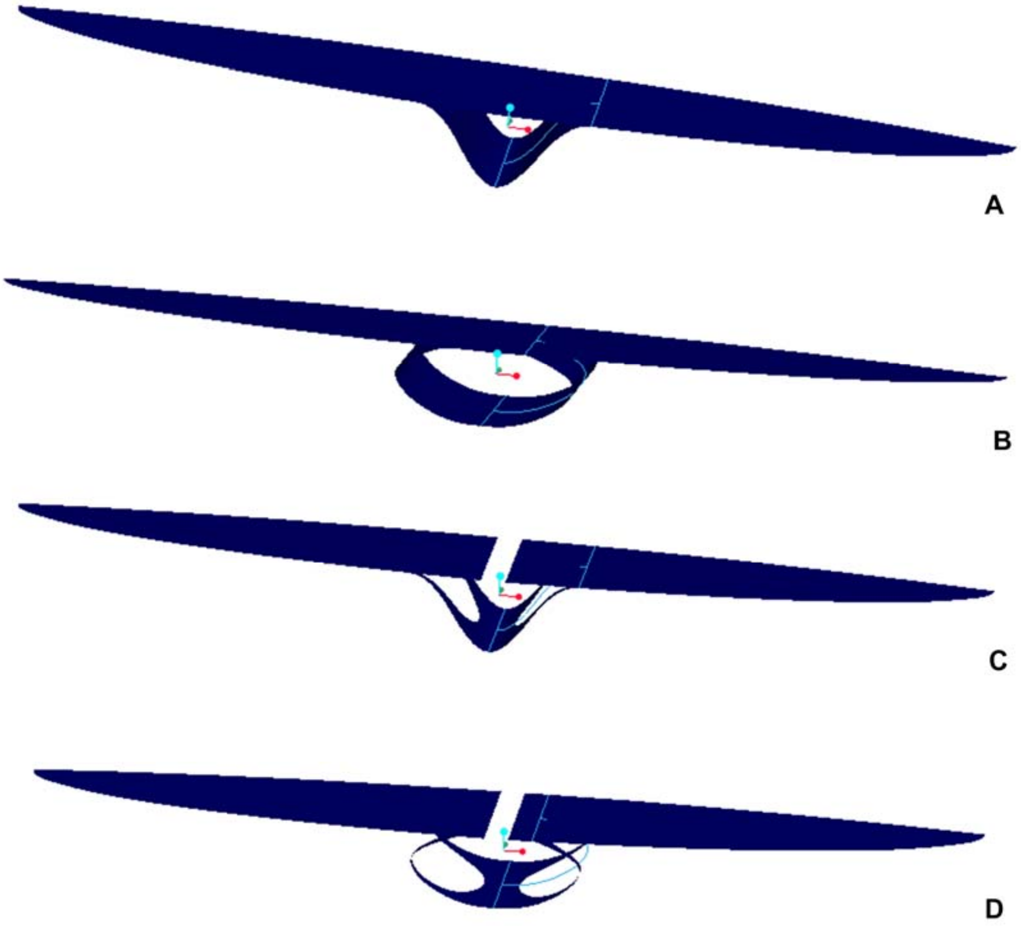

Figure 8-20. Four surface structures with flapping wings. A) Design 1, B) Design 2, C) Design 3, and D) Design 4.

In order to perform analysis of thin shell-like structures, the surface model analysis, IBFEM [65] have been extended to use 3D shell elements that are 3D elements with three degrees of freedom per node. These shell elements were used for the analysis. The total number of nodes in model is 666. Considering the symmetry of the geometry, half of the structure was modeled for the analysis. The structured mesh and the boundary conditions are shown in Figure 8-21. The magnetic force acts downward so that the wing produces upstroke. When one coil actuator is used, the applied force varies from 0 to 0.342 N at the edge. Using two coil actuators, the magnetic force can be double.

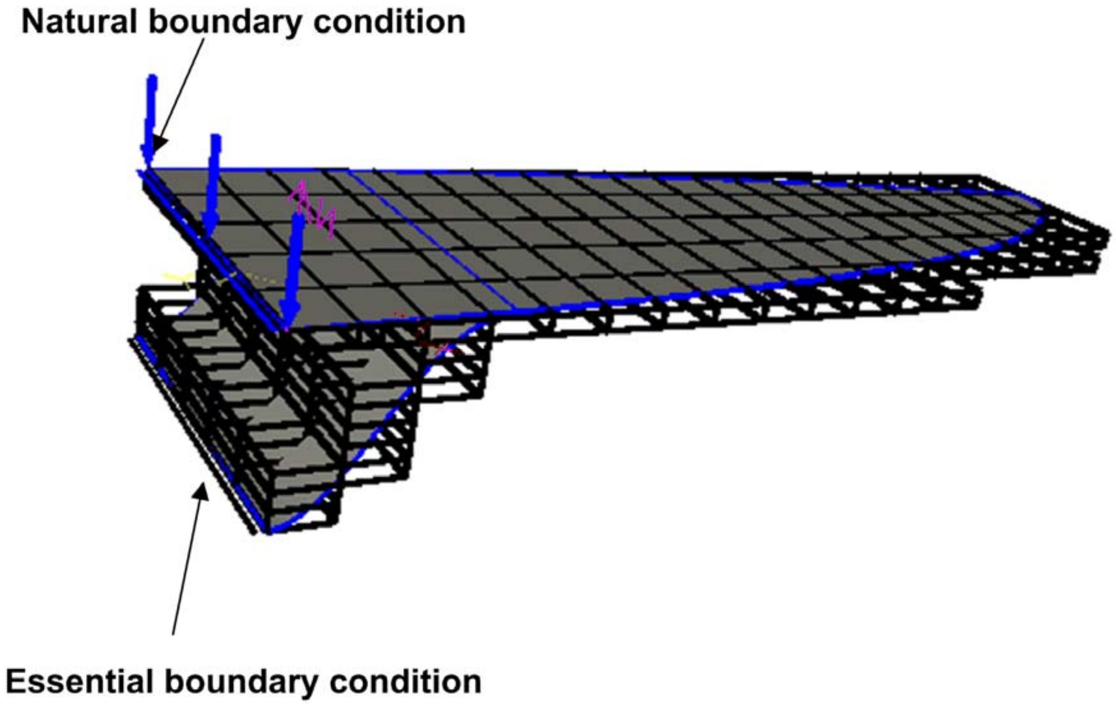

Figure 8-21. Structured mesh and boundary conditions of the first design

As the wing produces upstroke, the wing can also create down-stroke. Using the coil actuator, the same amount of Lorentz force can be produced in the opposite direction by changing the direction of the current. When *NI* is equal to 30, the wing up-strokes and down-strokes of the four designs are shown in Figure 8-22. For the up-stroke, the maximum displacement on the tip is $2.633\times10^{-3}mm$ in the first design, $4.238\times10^{-3}mm$ in the second design, $3.765\times10^{-2}mm$ in the third design, and $1.968\times10^{-1}mm$ in the fourth design. Magnitudes of the tip deflections during the wing up-stroke are the same as ones during the wing down-stroke because the magnetic force is proportional to the displacement. Thus, the tip deflection can be double including both strokes. Among the four designs studied here, the last design produces the largest tip deflection.

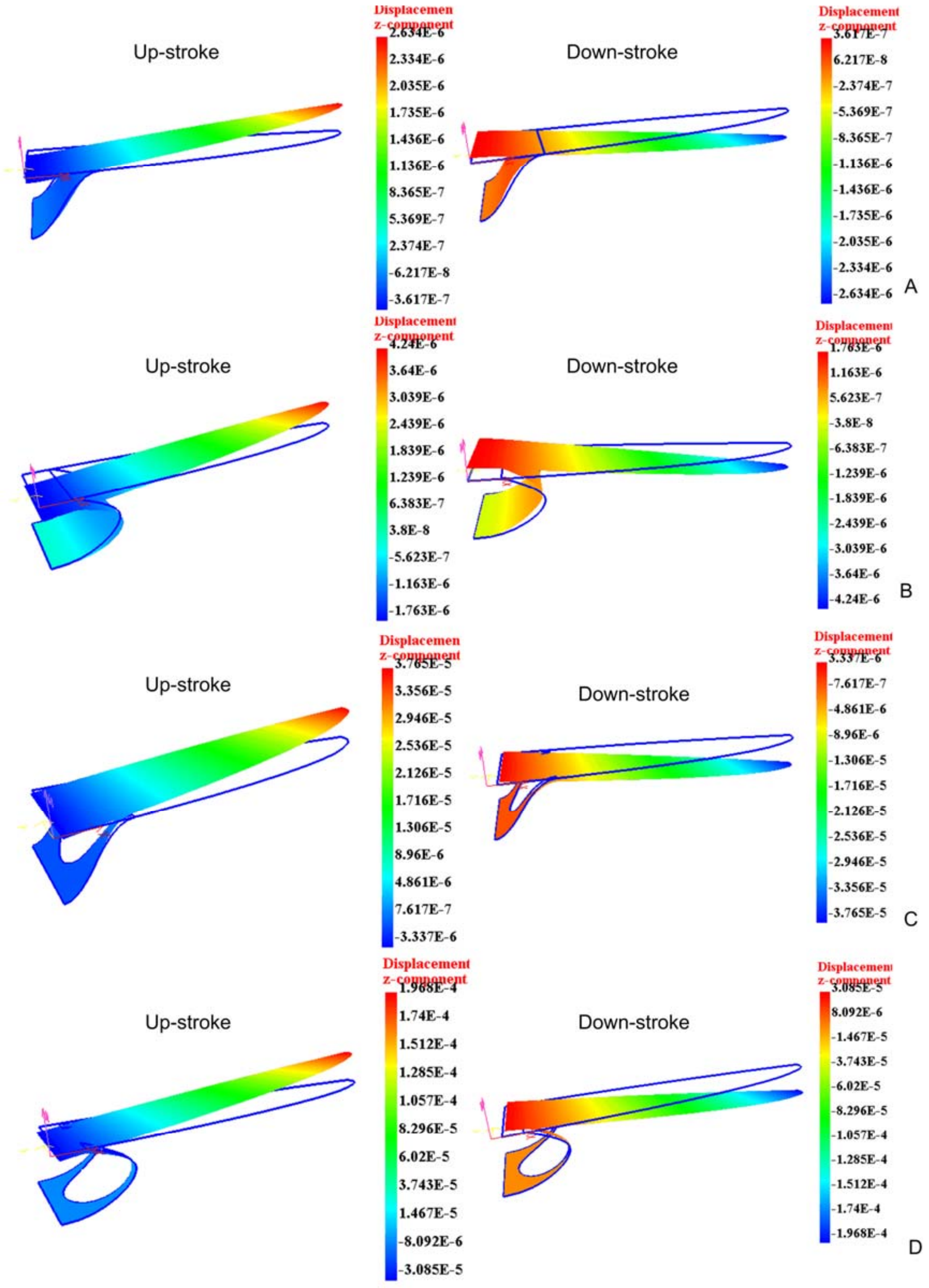

Figure 8-22. Displacement in the z-direction during the wing stroke. A) Design 1, B) Design 2, C) Design 3, and D) Design 4.

When *NI* varies from 1 to 168, the tip deflection as a function of the magnetomotive force is shown in Figure 8-23. The first three designs are too stiff for our application.

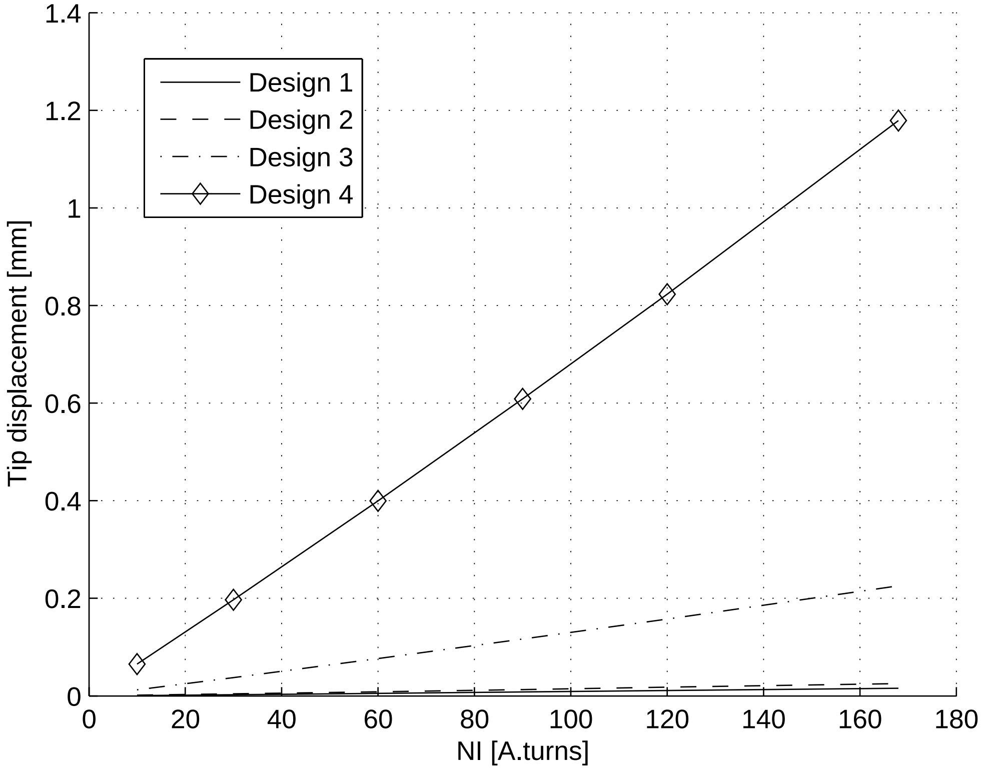

Figure 8-23. Tip displacement versus *NI* for wing upstroke

CHAPTER 9
CONCLUSIONS AND FUTURE WORK

Conclusions

The main research contributions made in this thesis are to extend Implicit Boundary Finite Element Method to

- Perform magnetostatic analysis
- Perform coupled magneto-elastostatic analysis
- Model multi-material system

Implicit Boundary Finite Element Method (IBFEM) for analysis using structured mesh has been demonstrated for 2D-and 3D-magnetostatic models and coupled magneto-elastostatic models. This approach directly uses the geometry imported from CAD systems without generating a conforming mesh. Structured meshes are easy to generate and the elements are regular and not distorted as in traditional finite element mesh. Furthermore, the internal elements are identical to each other and have the same stiffness matrix thus reducing the computation required.

In order to perform magnetostatic analysis, IBFEM requires the capability for the multi-material analysis. Each material has its own structured mesh, and a modified solution structure is applied at the interface elements. The multi-material analysis in magnetostatic problems allows magnetic force to be computed, a magnetic force that includes the magnetic surface force density and the Lorentz force. The magnetic surface force density is a force on ferro-material, and the Lorentz force is a force on a current carrying coil due to the magnetic flux. After computing these forces, the forces can then be used in a subsequent structural analysis to perform coupled magnetostatic-elastostatic analysis.

IBFEM has been evaluated using several 2D and 3D magnetostatic examples. Although those examples were complicated in terms of geometry, IBFEM could solve the problems without any distorted element. The results of those examples were compared to one using the reluctance method or to analytic solution when available. Based on the results of the magnetic flux density and the magnetic field density, the magnetic force was computed accurately. Through 2D problems, IBFEM presented faster convergence using quadratic B-spline elements, the method that created very accurate solutions with relatively fewer nodes. Moreover, IBFEM could solve large electromagnetic problems. In case of a 3D model with complex geometry, the structured mesh could allow relatively fewer elements to be used for the analysis. Consequently, the number of equations is smaller than the traditional finite element method.

Three open boundary techniques were implemented in the IBFEM software and evaluated using several examples. The open boundary techniques studied here include the truncation method, the asymptotic boundary conditions, and the decay function infinite element method. Several examples were used for comparing these three methods including permanent magnet, solenoid actuator, and two wire examples. Among the three methods studied, the asymptotic boundary conditions produced the most robust results no matter where magnetic sources were located.

The computed magnetic force could be subsequently used in the structural analysis. So, IBFEM could reveal relationship that exists between the magnetomotive force *NI* and the displacement of the structure. This relation is an important factor in designing a magnetically actuated structure. Several examples in 2D or 3D were created using a variety of structure geometry. Through the coupled magneto-elastostatic analysis, the relationships between magnetomotive force and displacement were studied for these examples.

IBFEM was used as a magnetic actuator design tool. In order to design an efficient magnetic actuator for a flapping-wing micro air vehicle, IBFEM was used to analyze several magnetic actuators created under the given specifications. These specifications include the range of *NI*, the size of a magnetic actuator and the weight of a magnetic actuator. Several magnetic actuators were examined such as clapper solenoid actuator, plunger solenoid actuator, combined clapper & plunger solenoid actuator and coil actuator. Among them, the coil actuator created the largest magnetic force for the given specifications. This magnetic force was used in structural analysis of flapping-wings modeled using 3D shell elements. Through the coupled magneto-elastostatic analysis, the relationship between the magnetomotive force of the coil actuator and the tip displacement of the flapping-wing structure was determined.

Future Work

This research focused on the steady static analysis so that the coupled problem is modeled as the weakly coupled magneto-elastostatic analysis. This assumption allows us to perform the magnetostatic and elastostatic analysis sequentially. If the magnetic field changes due to the elastic deformation, the problem becomes nonlinear and a strongly coupled nonlinear analysis is needed. The magnetic field may change because the structural deformation may cause permanent magnets or circuits attached to the structure to also move relative to each other. If the structure undergoes large deformation then geometric nonlinearities must be included. In addition, if the coupled problem is a dynamic problem, then the electrical circuits, the magnetic circuits and the structural analysis must be solved as a coupled problem. Another source of nonlinearity is due to contact between the armature and the stator.

The open boundary techniques should be further studied and extended for 3D magnetostatic problems. The open boundary techniques were studied in this thesis only for two dimensional problems. Asymptotic Boundary Condition (ABC) was found to be the most effective; however, this approach requires the user to specify the origin of the magnetic source. The accuracy of the results depends on careful choice of this origin. Further, research is needed to explore more effective ways of applying open boundary condition.

The magnetic force computation should be extended to nonlinear materials and permanent magnets. In this thesis, the magnetic force computation was implemented and studied only for linear ferrro-material and current carrying coils. In order to analyze magnetic actuators that involve moving permanent magnets, we need to implement force computation for permanent magnets.

In order to do dynamic analysis for flapping wings operated by magnetic actuators, nonlinear characteristics in geometry, force and kinematics must be considered. The wing motion creates large deformation so that a moment can be a function of deformation. When an armature of magnetic actuator moves toward stator, the magnetic force can vary according to the location of the armature. In addition, the contact problem occurs between the armature and the stator.

LIST OF REFERENCES

[1] T. Belytschko, Y. Krongauz, D. Organ, M. Fleming, and P. Krysl, "Meshless methods: An overview and recent developments," *Computer Methods in Applied Mechanics and Engineering*, vol. 139, pp. 3-47, 1996.

[2] K. M. Lee, Q. Li, and H. Sun, "Effects of numerical formulation on magnetic field computation using meshless methods," *IEEE Transactions on Magnetics*, vol. 42, pp. 2164-2171, 2006.

[3] Q. Li and K. M. Lee, "An adaptive meshless method for magnetic field computation," *IEEE Transactions on Magnetics*, vol. 42, pp. 1996-2003, 2006.

[4] A. Bruyere, L. Illoul, F. Chinesta, and S. Clenet, "Comparison between NEM and FEM in 2-D magnetostatics using an error estimator," *IEEE Transactions on Magnetics*, vol. 44, pp. 1342-1345, 2008.

[5] X. Liu, Y. M. Deng, Z. W. Zeng, L. Udpa, and S. S. Udpa, "Model-Based Inversion Technique Using Element-Free Galerkin Method and State Space Search," *IEEE Transactions on Magnetics*, vol. 45, pp. 1486-1489, 2009.

[6] O. Bottauscio, M. Chiampi, and A. Manzin, "Computation of higher order spatial derivatives in the multiscale expansion of electromagnetic-field problems," *IEEE Transactions on Magnetics*, vol. 44, pp. 1194-1197, 2008.

[7] K. Muramatsu, Y. Yokoyama, and N. Takahashi, "3-D magnetic field analysis using nonconforming mesh with edge elements," *IEEE Transactions on Magnetics*, vol. 38, pp. 433-436, 2002.

[8] T. Belytschko, C. Parimi, N. Moes, N. Sukumar, and S. Usui, "Structured extended finite element methods for solids defined by implicit surfaces," *International Journal for Numerical Methods in Engineering*, vol. 56, pp. 609-635, 2003.

[9] N. Moes, E. Bechet, and M. Tourbier, "Imposing Dirichlet boundary conditions in the extended finite element method," *International Journal for Numerical Methods in Engineering*, vol. 67, pp. 1641-1669, 2006.

[10] Y. Abdelaziz and A. Hamouine, "A survey of the extended finite element," *Computers & Structures*, vol. 86, pp. 1141-1151, 2008.

[11] P. M. A. Areias and T. Belytschko, "Analysis of three-dimensional crack initiation and propagation using the extended finite element method," *International Journal for Numerical Methods in Engineering*, vol. 63, pp. 760-788, 2005.

[12] T. Belytschko and T. Black, "Elastic crack growth in finite elements with minimal remeshing," *International Journal for Numerical Methods in Engineering*, vol. 45, pp. 601-620, 1999.

[13] A. V. Kumar, R. Burla, S. Padmanabhan, and L. X. Gu, "Finite element analysis using nonconforming mesh," *Journal of Computing and Information Science in Engineering*, vol. 8, 2008.

[14] A. V. Kumar, S. Padmanabhan, and R. Burla, "Implicit boundary method for finite element analysis using non-conforming mesh or grid," *International Journal for Numerical Methods in Engineering*, vol. 74, pp. 1421-1447, 2008.

[15] R. K. Burla and A. V. Kumar, "Implicit boundary method for analysis using uniform B-spline basis and structured grid," *International Journal for Numerical Methods in Engineering*, vol. 76, pp. 1993-2028, 2008.

[16] R. K. Burla, A. V. Kumar, and B. V. Sankar, "Implicit boundary method for determination of effective properties of composite microstructures," *International Journal of Solids and Structures*, vol. 46, pp. 2514-2526, 2009.

[17] S. R. H. Hoole, *Computer-aided analysis and design of electromagnetic devices*. New York: Elsevier, 1989.

[18] J. R. Brauer, *Magnetic Actuators and Sensors*: John Wiley & Sons, 2006.

[19] K. Vijayakumar, R. Karthikeyan, S. Paramasivam, R. Arumugam, and K. N. Srinivas, "Switched Reluctance Motor Modeling, Design, Simulation, and Analysis: A Comprehensive Review," *IEEE Transactions on Magnetics*, vol. 44, pp. 4605-4617, 2008.

[20] V. L. Rvachev and T. I. Sheiko, "R-Functions in Boundary Value Problems in Mechanics," *Applied Mechanics Reviews*, vol. 48, pp. 151-188, 1995.

[21] V. Shapiro and I. Tsukanov, "Meshfree simulation of deforming domains," *Computer-Aided Design*, vol. 31, pp. 459-471, 1999.

[22] K. Hollig, C. Apprich, and A. Streit, "Introduction to the Web-method and its applications," *Advances in Computational Mathematics*, vol. 23, pp. 215-237, 2005.

[23] G. Apaydin, S. Seker, and N. Ari, "Weighted extended b-splines for one-dimensional electromagnetic problems," *Applied Mathematics and Computation*, vol. 190, pp. 1125-1135, 2007.

[24] G. Apaydin, S. Seker, and N. Ari, "Application of web-spline method in electromagnetics," *Aeu-International Journal of Electronics and Communications*, vol. 62, pp. 163-173, 2008.

[25] J. L. Coulomb and G. Meunier, "Finite-Element Implementation of Virtual Work Principle for Magnetic or Electric Force and Torque Computation," *IEEE Transactions on Magnetics*, vol. 20, pp. 1894-1896, 1984.

[26] Z. Ren and A. Bossavit, "A new approach to eddy current problems in deformable conductors and some numerical evidence about its validity," *International Journal for Applied Electromagnetics in Materials*, vol. 3, pp. 39-46, 1992.

[27] Z. Ren and A. Razek, "Local Force Computation in Deformable-Bodies Using Edge Elements," *IEEE Transactions on Magnetics*, vol. 28, pp. 1212-1215, 1992.

[28] Z. Ren, "Comparison of Different Force Calculation Methods in 3d Finite-Element Modeling," *IEEE Transactions on Magnetics*, vol. 30, pp. 3471-3474, 1994.

[29] J. Bastos and N. Sadowski, *Electromagnetic modeling by finite element methods*: CRC Press, 2003.

[30] R. S. Grandia, V. A. Galindo, A. U. Galve, and R. V. Fos, "General formulation for magnetic forces in linear materials and permanent magnets," *IEEE Transactions on Magnetics*, vol. 44, pp. 2134-2140, 2008.

[31] J. Simkin and C. W. Trowbridge, "Use of the Total Scalar Potential in the Numerical-Solution of Field Problems in Electromagnetics," *International Journal for Numerical Methods in Engineering*, vol. 14, pp. 423-440, 1979.

[32] J. L. Coulomb, "Finite-Element 3 Dimensional Magnetic-Field Computation," *IEEE Transactions on Magnetics*, vol. 17, pp. 3241-3246, 1981.

[33] O. Biro and K. Preis, "On the Use of the Magnetic Vector Potential in the Finite-Element Analysis of 3-Dimensional Eddy Currents," *IEEE Transactions on Magnetics*, vol. 25, pp. 3145-3159, 1989.
[34] K. Preis, I. Bardi, O. Biro, C. Magele, W. Renhart, K. R. Richter, and G. Vrisk, "Numerical-Analysis of 3d Magnetostatic Fields," *IEEE Transactions on Magnetics*, vol. 27, pp. 3798-3803, 1991.
[35] R. Albanese and G. Rubinacci, "Magnetostatic Field Computations in Terms of 2-Component Vector Potentials," *International Journal for Numerical Methods in Engineering*, vol. 29, pp. 515-532, 1990.
[36] R. C. Mesquita and J. P. A. Bastos, "An Incomplete Gauge Formulation for 3d Nodal Finite-Element Magnetostatics," *IEEE Transactions on Magnetics*, vol. 28, pp. 1044-1047, 1992.
[37] N. A. Demerdash and R. Wang, "Theoretical and Numerical Difficulties in 3-D Vector Potential Methods in Finite-Element Magnetostatic Computations," *IEEE Transactions on Magnetics*, vol. 26, pp. 1656-1658, 1990.
[38] A. S. Semenov, H. Kessler, A. Liskowsky, and H. Balke, "On a vector potential formulation for 3D electromechanical finite element analysis," *Communications in Numerical Methods in Engineering*, vol. 22, pp. 357-375, 2006.
[39] J. Jin, *The Finite Element Method in Electromagnetics*, 2 ed: Wiley-IEEE Press, 2002.
[40] Q. Chen and A. Konrad, "A review of finite element open boundary techniques for static and quasi-static electromagnetic field problems," *IEEE Transactions on Magnetics*, vol. 33, pp. 663-676, 1997.
[41] G. Ventura, "On the elimination of quadrature subcells for discontinuous functions in the eXtended Finite-Element Method," *International Journal for Numerical Methods in Engineering*, vol. 66, pp. 761-795, 2006.
[42] S. Natarajan, S. Bordas, and D. R. Mahapatra, "Numerical integration over arbitrary polygonal domains based on Schwarz-Christoffel conformal mapping," *International Journal for Numerical Methods in Engineering*, vol. 80, pp. 103-134, 2009.
[43] D. A. Lowther, C. B. Rajanathan, and P. P. Silvester, "Finite-Element Technique for Solving 2-D Open Boundary Problems," *IEEE Transactions on Magnetics*, vol. 14, pp. 467-469, 1978.
[44] J. R. Brauer, "Open Boundary Finite-Elements for Axisymmetric Magnetic and Skin Effect Problems," *Journal of Applied Physics*, vol. 53, pp. 8366-8368, 1982.
[45] C. Antunes, "Approximate Ballooning Techniques," *IEEE Transactions on Magnetics*, vol. 19, pp. 2555-2557, 1983.
[46] C. Antunes, E. M. Freeman, D. Lowther, and P. Silvester, "A Static Ballooning Technique for 2-D Open Boundary-Problems," *Journal of Applied Physics*, vol. 53, pp. 8360-8362, 1982.
[47] Y. S. Sun, G. S. Zhang, and W. Chen, "A Data-Base Method for 3d-Open Boundary Field Computation," *IEEE Transactions on Magnetics*, vol. 26, pp. 807-810, 1990.
[48] W. Chen, G. S. Zhang, Y. S. Sun, M. J. Chen, and Y. Zhao, "The Application of the Data-Base Method for 3-D Open Boundary Field Computation," *IEEE Transactions on Magnetics*, vol. 28, pp. 1686-1689, 1992.

[49] J. R. Brauer, S. M. Schaefer, J. F. Lee, and R. Mittra, "Asymptotic Boundary-Condition for 3-Dimensional Magnetostatic Finite-Elements," *IEEE Transactions on Magnetics*, vol. 27, pp. 5013-5015, 1991.

[50] Q. S. Chen, A. Konrad, and S. Baronijan, "Asymptotic Boundary-Conditions for Axisymmetrical Finite-Element Electrostatic Analysis," *IEEE Transactions on Magnetics*, vol. 30, pp. 4335-4337, 1994.

[51] Q. Chen, A. Konrad, and P. P. Biringer, "Computation of 3-Dimensional Unbounded Eddy-Current Problems Using Asymptotic Boundary-Conditions," *IEEE Transactions on Magnetics*, vol. 31, pp. 1348-1351, 1995.

[52] S. Gratkowski, L. Pichon, and H. Gajan, "Asymptotic boundary conditions for open boundaries of axisymmetric magnetostatic finite-element models," *IEEE Transactions on Magnetics*, vol. 38, pp. 469-472, 2002.

[53] R. L. Ungless, "An infinite finite element," vol. Master of Science. Canada: The University of British Columbia, 1973.

[54] P. Bettess, "Infinite Elements," *International Journal for Numerical Methods in Engineering*, vol. 11, pp. 53-64, 1977.

[55] P. Bettess, "More on Infinite Elements," *International Journal for Numerical Methods in Engineering*, vol. 15, pp. 1613-1626, 1980.

[56] P. Bettess, *Infinite elements*. Sunderland, UK: Penshaw Press, 1993.

[57] B. M. A. Rahman and J. B. Davies, "Finite-Element Analysis of Optical and Microwave Waveguide Problems," *IEEE Transactions on Microwave Theory and Techniques*, vol. 32, pp. 20-28, 1984.

[58] M. J. McDougall and J. P. Webb, "Infinite Elements for the Analysis of Open Dielectric Wave-Guides," *IEEE Transactions on Microwave Theory and Techniques*, vol. 37, pp. 1724-1731, 1989.

[59] M. S. Towers, A. McCowen, and J. A. R. Macnab, "Electromagnetic Scattering from an Arbitrary, Inhomogeneous 2-D Object - a Finite and Infinite Element Solution," *IEEE Transactions on Antennas and Propagation*, vol. 41, pp. 770-777, 1993.

[60] G. Beer and J. L. Meek, "Infinite Domain Elements," *International Journal for Numerical Methods in Engineering*, vol. 17, pp. 43-52, 1981.

[61] O. C. Zienkiewicz, C. Emson, and P. Bettess, "A Novel Boundary Infinite Element," *International Journal for Numerical Methods in Engineering*, vol. 19, pp. 393-404, 1983.

[62] T. T. Abdel-Fattah, H. A. Hodhod, and A. Y. Akl, "A novel formulation of infinite elements for static analysis," *Computers & Structures*, vol. 77, pp. 371-379, 2000.

[63] M. V. K. Chari and S. J. Salon, *Numerical methods in electromagnetism*. San Diego: Academic press, 2000.

[64] R. Arumugam, D. A. Lowther, R. Krishnan, and J. F. Lindsay, "Magnetic-Field Analysis of a Switched Reluctance Motor Using a Two-Dimensional Finite-Element Model," *IEEE Transactions on Magnetics*, vol. 21, pp. 1883-1885, 1985.

[65] P. D. S. Periyasamy, "Finite element analysis of shell like structures using implicit boundary method," in *Mechanical and Aerospace engineering*, vol. Master of Science. Gainesville: University of Florida, 2009, pp. 86.

[66] S. Zhang and A. V. Kumar, "Magnetic Field Computation using Implicit boundary Finite Element Method," *IEEE Transactions on Magnetics*, in press, 2010.

[67] S. Zhang and A. V. Kumar, "3D Magnetostatic Analysis using Implicit Boundary Finite Element Method," *Computers & Structures*, submitted 2010.

BIOGRAPHICAL SKETCH

Sung-Uk Zhang was born in Seoul, South Korea. He graduated with a bachelor's degree in electrical engineering from the Sogang University, South Korea in February 2003. In December 2006, he achieved a master's degree in biomedical engineering from the University of Florida. Then, he enrolled in the doctoral problem in mechanical and aerospace engineering at the University of Florida in January 2007. His areas of interest include digital signal processing, electrical impedance tomography, inverse problem, finite element method, and computer-aided geometric design.